

**Anatomical Structure Analysis of the  
Thoracic Area Based on Volumetric Images:  
From Blobs to Fibers**

**Hirohisa Oda**



# Abstract

Anatomy is the field of study that reveals the structures of bodies. Computational anatomy is a subfield of anatomy that introduces computational techniques to analyze structures. Image processing with computer vision techniques is undeniably fundamental for revealing anatomies. For instance, segmenting organs allows us to investigate the target organs' shapes and sizes. In this thesis, I focus on anatomies in the thorax.

There are various imaging techniques, such as endoscopes, X-ray computed tomography (CT), magnetic resonance imaging (MRI), and microscopes, some of which are available for use in living bodies, including clinically available CT and MRI scanners. Although optical or electron microscopes have much higher resolution than clinically available CT or MRI scanners, they cannot be used for living bodies and usually produce only 2-dimensional images of a tiny region.

For revealing anatomical structures using computational techniques, analyzing from 3-dimensional images is preferred, such as from CT or MRI images. However, since the spatial resolutions of these imaging techniques are not very high, some anatomies are vague and unclear. Non-clinical high-resolution imaging techniques, such as micro-focus X-ray CT ( $\mu$ CT), are also available to acquire images of small tissues that cannot be observed on the CT or MRI images of living bodies. However, there are still small structures that appear vague and unclear in  $\mu$ CT volumes.

This work aims to make it possible to reveal anatomical structures in the thorax with

3-dimensional images. As mentioned, a common difficulty is vague and unclear images of small tissues. We approach this problem by 1) a novel filtering technique and 2) image evaluation for analysis.

The first topic is a mediastinal lymph node detection method based on intensity targeted radial structure tensor (ITRST) analysis. We propose a new image processing filter for lymph nodes on CT volumes. Mediastinal lymph nodes are around only 10 mm in diameter, have low contrast on CT volumes, and unclear boundaries. Typical filters are often negatively affected by surrounding regions having higher contrast. The proposed detection method based on ITRST analysis correctly detected lymph nodes even if with various surrounding tissues or regions, e.g., contrast-enhanced blood vessels, air, etc. In the experiments, the proposed method's detection rate was 84.2 %, with 9.1 false positives per volume for lymph nodes whose short axis was at least 10 mm, which outperformed the conventional filtering methods.

The second topic is cardiac fiber tracking.  $\mu$ CT volumes acquired by a desktop-type scanner are vague for cardiac fibers compared to a more expensive high-resolution imaging technique (refraction-contrast X-ray CT). Evaluating the efficacy of  $\mu$ CT volumes for fiber tracking is vital for further investigation using  $\mu$ CT. Although fiber tracking is possible using structure tensor analysis, it is unclear that  $\mu$ CT is useful. Comparing results from  $\mu$ CT and refraction-contrast X-ray CT allows us to discuss the efficacies and limitations of these imaging techniques. In the experiments, fiber orientations estimated by two imaging techniques were closely resembled under the correlation coefficient of 0.63. Two imaging techniques' fiber tracking results were also similar and followed the anatomical knowledge. The  $\mu$ CT volume's limitations were found for the artifacts and stitching scanning.

This thesis consists of five chapters. Chapter 1 provides the motivations of the author's research as the introduction. Chapter 2 describes background information, including anatomical study fields, imaging techniques for anatomical studies, and tho-

racic anatomies. Chapter 3 describes the mediastinal lymph node detection method. Chapter 4 describes cardiac fiber tracking from  $\mu$ CT volumes and Chapter 5 provides a summary and description of our future work.



# Contents

<b>Abstract</b>	<b>i</b>
<b>Contents</b>	<b>ix</b>
<b>1 Introduction</b>	<b>1</b>
1.1 Preface . . . . .	1
1.2 Goal . . . . .	2
1.3 Computational analysis of thoracic anatomies . . . . .	4
1.3.1 Lungs . . . . .	4
1.3.2 Bronchus . . . . .	6
1.3.3 Lymph nodes . . . . .	7
1.3.4 Hearts . . . . .	7
1.4 Approaches for unclearly shown anatomies . . . . .	8
1.4.1 Prior shape information: Cardiac chambers and blood vessels on MRI . . . . .	10
1.4.2 Bloblike filters or texture features: Mediastinal lymph nodes on CT	10
1.4.3 Tubelike filters: deep branches on CT . . . . .	11
1.4.4 Structure tensor: cardiac fibers on $\mu$ CT . . . . .	12
1.5 Topics . . . . .	12
1.5.1 Motivation . . . . .	12

1.5.2	Topic 1: Mediastinal lymph node detection . . . . .	13
1.5.3	Topic 2: Cardiac fiber tracking . . . . .	14
1.6	Thesis structure . . . . .	14
<b>2</b>	<b>Anatomical studies and computational analysis</b>	<b>17</b>
2.1	Anatomy . . . . .	17
2.1.1	Anatomical studies until modern age . . . . .	18
2.1.2	Gross anatomy . . . . .	20
2.1.3	Surface anatomy . . . . .	21
2.1.4	Microscopic anatomy . . . . .	21
2.1.5	Computational anatomy . . . . .	22
2.2	Imaging for anatomical studies . . . . .	22
2.2.1	Optical camera . . . . .	26
2.2.2	Endoscope . . . . .	26
2.2.3	Optical microscope . . . . .	28
2.2.4	Electron microscope . . . . .	29
2.2.5	(2D) Radiograph . . . . .	31
2.2.6	Computed Tomography (CT) . . . . .	32
2.2.7	Magnetic resonance imaging (MRI) . . . . .	37
2.2.8	Scintigraphy . . . . .	38
2.2.9	Ultrasonography . . . . .	39
2.3	Thoracic anatomies . . . . .	40
2.3.1	Exploring thorax . . . . .	40
2.3.2	Lungs . . . . .	40
2.3.3	Bronchus . . . . .	41
2.3.4	Lymph nodes . . . . .	41
2.3.5	Heart and blood vessels . . . . .	42

2.4	Computational anatomy in thorax . . . . .	47
2.4.1	Motivations of focusing on thorax . . . . .	47
2.4.2	Assistance of clinical practices . . . . .	47
<b>3</b>	<b>Mediastinal lymph node detection</b>	<b>51</b>
3.1	Overview . . . . .	51
3.2	Background . . . . .	52
3.3	Conventional local intensity structure analyses . . . . .	55
3.3.1	Hessian analysis . . . . .	55
3.3.2	RST analysis . . . . .	56
3.4	ITRST-based lymph node detection method . . . . .	57
3.4.1	ITRST filter . . . . .	57
3.4.2	Mediastinal lymph node detection . . . . .	59
3.5	Experiments . . . . .	65
3.5.1	ITRST filter . . . . .	65
3.5.2	Mediastinal lymph node detection . . . . .	66
3.6	Results . . . . .	72
3.6.1	ITRST filter . . . . .	72
3.6.2	Mediastinal lymph node detection . . . . .	72
3.7	Discussion . . . . .	77
3.7.1	ITRST filter . . . . .	77
3.7.2	Mediastinal lymph node detection . . . . .	78
3.7.3	Lung area segmentation . . . . .	80
3.8	Conclusions . . . . .	80
<b>4</b>	<b>Cardiac fiber tracking</b>	<b>85</b>
4.1	Overview . . . . .	85
4.2	Background . . . . .	86

4.3	Fiber analysis method . . . . .	88
4.3.1	Overview . . . . .	88
4.3.2	Fiber orientation estimation . . . . .	88
4.3.3	Fiber tracking . . . . .	89
4.4	Materials . . . . .	89
4.4.1	Scanning . . . . .	89
4.4.2	Registration . . . . .	93
4.5	Experimental setup . . . . .	95
4.5.1	Overview . . . . .	95
4.5.2	Fiber orientation statistics . . . . .	96
4.5.3	3D visualization of fibers . . . . .	98
4.6	<b>Results</b> . . . . .	98
4.6.1	Fiber orientation statistics . . . . .	98
4.6.2	3D visualization of fibers . . . . .	99
4.7	Discussions . . . . .	100
4.7.1	Fiber orientation statistics . . . . .	100
4.7.2	3D visualization of fibers . . . . .	104
4.8	Conclusions and limitations . . . . .	104
<b>5</b>	<b>Summary and future work</b>	<b>107</b>
5.1	Summary . . . . .	107
5.1.1	Overall conclusion . . . . .	107
5.1.2	Mediastinal lymph node detection . . . . .	108
5.1.3	Cardiac fiber tracking . . . . .	109
5.1.4	Further challenges . . . . .	110
5.2	Blueprints . . . . .	112
5.2.1	Incorporating advantages of various imaging techniques . . . . .	112

<i>CONTENTS</i>	ix
5.2.2 Assisting elementary or secondary education . . . . .	113
5.2.3 3D imaging and analysis for microscopic anatomy . . . . .	113
5.2.4 Deep learning techniques for various imaging techniques . . . . .	114
5.2.5 Finding unknown anatomies . . . . .	115
<b>Acknowledgments</b>	<b>117</b>
<b>References</b>	<b>119</b>
<b>Publications</b>	<b>155</b>



# List of Tables

1.1	Analysis methods for anatomies or lesions in the thorax that are unclear on 3D images. . . . .	9
2.1	Typical characteristics of imaging techniques. All resolutions are approximate values for each imaging technique’s main target. Exceptions also exist for other characteristics. . . . .	25
3.1	Features for FP reduction step. . . . .	64
3.2	Specification of CT volumes used in experiments of mediastinal lymph node detection. . . . .	66
3.3	Number of lymph nodes categorized by short axes. . . . .	66
3.4	Constant parameter values. (a) ITRST filter. (b) Mediastinal lymph node detection: Initial detection evaluation. (c) Mediastinal lymph node detection: Overall detection performance evaluation. Note that $r_{\text{target}}$ , $t_{\text{blob}}$ , and $w_{\text{F}}$ are not shown here since they are varied for evaluating the performances of different conditions. . . . .	69
3.5	Comparison of lymph node detection performances. Note that symbol * represents performance shown in publications. Their experiments were performed using different datasets or criteria from ours. . . . .	76
3.6	Fisher’s exact test among detection rate at 10.0 FPs/volume. . . . .	77

4.1 Specification of RCT scanning. . . . . 92

4.2 Specifications of  $\mu$ CT scanning . . . . . 93

# List of Figures

- 1.1 Anatomies in thorax respecting to physical size. . . . . 4
- 1.2 Anatomies around the lungs on a CT volume. Spatial resolution is  $0.723 \times 0.723 \times 0.801 \text{ mm}^3$ . (a) Mediastinal window. Window width (WW) is 400 H.U. and window level (WL) is 0 H.U. (b) Lung window. Annotations of the bronchus cover limited parts on image. WW is 500 H.U. and WL is -800 H.U. . . . . 5
- 1.3 CT and MRI volumes of the heart. (a) MRI (T1-weighted) volume. Figure 1 in [216] with annotation by this thesis’s author. Spatial resolution is  $1.37 \times 1.37 \times 8.0 \text{ mm}^3$ . (b) CT (arterial phase) volume. Spatial resolution is  $0.644 \times 0.644 \times 0.801 \text{ mm}^3$ . . . . . 15
- 2.1 Illustrations of anatomy until modern age. (a) Leonardo da Vinci’s illustration of cardiac valves (Fig. 3 on [137]). (b) Gempaku Sugita’s illustration of heart (Fig. 1.2 on [139], pp. 32) . . . . . 18
- 2.2 Medical image processing for observation of anatomies. (a) Organ segmentation from CT volumes. Figure obtained from [32] with additional notes. (b) Lung nodule detection from CT volumes. Figure obtained from movie frame in [26] with additional notes. . . . . 23

- 2.3 Imaging techniques. (a) Digital camera, DSC-WX500 (Sony, Japan). (b) Bronchoscope, BF-XT190 (OLYMPUS, Japan). Figure from [23] (c) Virtual slide scanner, VS120 (OLYMPUS, Japan). (d) Electron microscope, SU7000 (Hitachi High-Tech, Japan). Figure from [25] (e) 2D X-ray scanner, DigitalDiagnost (Philips, Netherlands). Figure from [20] (f) Clinical CT scanner, Aquilion ONE / GENESIS Edition (Canon Medical Systems, Japan). Figure from [21] (g)  $\mu$ CT scanner, SMX-90CT Plus (Shimadzu, Japan). (h) MRI scanner, Ingenia Elition 3.0T X (Philips, Netherlands). Figure from [22] (i) Ultrasonic imaging system, Aplio i900 (Canon Medical Systems, Japan). Figure from [24]. . . . . 27
- 2.4 Compound optical microscope. (a) Components of compound optical microscope. Figure from [167] (b) Working principle. Real image ( $A'B'$ ) is generated by objective lens (C1) for object (A-B). From real image ( $A'B'$ ), eye piece (C2) generates virtual image ( $A''B''$ ) which can be observed by eye. Figure from [168] . . . . . 28
- 2.5 Electron microscopes: transmission electron microscopy (TEM) and scanning electron microscopy (SEM). (c) SEM and TEM images of escherichia coli O-157. Figure from [169] with annotations by thesis' author (a) TEM. Part of Fig. 2.1 in [66] (b) SEM. Part of Fig. 2.2 in [66] . . . . . 30
- 2.6 Principle of CT reconstruction with filtered-back-propagation (FBP). Figs. 4 and 5 on pp. 191-192 in [127] with modifications by thesis' author. (a) Recording projection data. (b) Recording projection data from various angles. (c) Filtering. (d) Reconstruction with FBP. . . . . 34

2.7	Efficacy of filtering. Parts of Fig 2.3, 2.4, 2.5, and 2.6 on [190] with modifications by thesis' author. (a) Schematic illustrations. Simple back-propagation generates blurred images, while filtered back-propagation generates much more clear images. (b) Reconstruction results of abdominal CT volume. . . . .	35
2.8	Basics of MR imaging. Figures 1, 2, 4 and 5 on [185] with modifications by thesis' author. (a) Protons and nuclear magnification. When static magnetic field $H_0$ is offered, magnetic field $M_0$ generated by protons directs along $z$ -axis. (b) Excitation. When 90-degree pulse is given, magnetic vectors lie on $x - y$ plane. (c) T1- and T2-relaxations. (d) Example of time sequence for spin-echo method. . . . .	43
2.9	Body surface and major anatomies around thorax. Image courtesy of Visible Body [50] (annotations by author of thesis). . . . .	44
2.10	Organs (lungs and heart), bronchus and their surroundings. Image courtesy of Visible Body [50] (annotations by author of thesis). . . . .	44
2.11	Detailed illustrations of bronchus. (a) Entire bronchus. (b) Around termination of branches. . . . .	45
2.12	Detailed illustrations of lungs, bronchus and surrounding lymph nodes and vessels (pp. 197 in [27]). . . . .	46
2.13	Detailed illustrations of the left ventricle of the heart (pp. 209 in [27]). . . . .	46
3.1	Intensity profile of lymph node. (a) Example of axial slice and its magnification of lymph node. Yellow represents lymph nodes. (b) Intensity profile on the line segment A-B shown in (a). . . . .	54

3.2	Schematic illustration showing differences between (a) RST and (b) ITRST filters. Point $\boldsymbol{x}$ is in sphere, and sphere is touching region with very low intensities. Top row represents intensity gradients that are summed into RST and ITRST, respectively. Bottom row represents magnitudes of eigenvalues $\lambda_0, \lambda_1, \lambda_2$ ( $ \lambda_0  \geq  \lambda_1  \geq  \lambda_2 $ ) with corresponding eigenvectors of RST and ITRST, respectively. . . . .	58
3.3	Synthetic examples of solid objects. (a) Blueprint of artificially-generated volume. Slice contains centers of all spheres. (b) Slice containing one isolated sphere and six spheres touching bright (300 H.U.) or dark (-1000 H.U.) square poles. . . . .	68
3.4	Responses for synthetic volume. (a) ITRST filter. (b) RST filter. (c) Hessian filter. Color scheme is same as (a). Blue represents low response (around 1), yellow represents medium response (around 125), and red represents high response (around 250). . . . .	73
3.5	Eigenvalue profiles on lines A–B and C–D shown in Fig. 3.3 (b). (a) ITRST filter. (b) RST filter. (c) Hessian filter. . . . .	74
3.6	FROC curves obtained after initial detection ( $t_{\text{blob}}$ for 20.0, 40.0, 80.0, and 160.0 for ITRST and RST filters, and $t_{\text{blob}}$ for 2000, 4000, 8000, and 16000 for Hessian filter). (a) $r_{\text{target}} = 5$ mm. (b) $r_{\text{target}} = 7.5$ mm. (c) $r_{\text{target}} = 10$ mm. . . . .	75
3.7	FROC curves obtained after FP reduction ( $w_F$ for 0.025, 0.05, 0.075, 0.10, 0.125, 0.15, 0.20, 0.25, 0.30, 0.40, and 0.50) with $t_{\text{blob}} = 20$ for ITRST and RST filters, and $t_{\text{blob}} = 2000$ for Hessian filter. (a) $r_{\text{target}} = 5$ mm. (b) $r_{\text{target}} = 7.5$ mm. (c) $r_{\text{target}} = 10$ mm. . . . .	82

3.8	Examples of detection results (a)–(e) with parameters $t_{\text{blob}} = 20$ and $r_{\text{target}} = 10$ mm. Yellow denotes ground truth. Cyan denotes TP detection. Red denotes FP detection. Green represents detection of small or hilar lymph nodes. First two rows represent candidate regions and after FP reduction using ITRST filter. Third and fourth rows represent results of RST filter. Fifth and sixth rows are of Hessian filter. . . . .	83
3.9	Target region extraction on volume having lung cancer region. (a) Input volume. (b) Lung cancer region. (c) Lung region. (d) Target region. . .	84
4.1	Rabbit heart: longest axis is about 20 mm. . . . .	90
4.2	Machines that scanned rabbit heart shown in Fig. 4.1: (a) RCT and (b) $\mu\text{CT}$ . . . . .	90
4.3	Axial and coronal slices of (a) RCT and (b) $\mu\text{CT}$ volumes. Fibers on RCT volume look clearer than those of $\mu\text{CT}$ volume. Registration is required for comparison due to different heart positions. . . . .	91
4.4	Coordinate system and position of ventricles: Axial planes (x-y plane) cut axis along base and apex into rounds. On axial planes, RV is shown on left of LV. Outside ratio is illustrated in magnified part. Outside ratio becomes 0 % at endocardium side and 100 % at epicardium side. . . . .	94
4.5	Axial and coronal slices of registered volumes: Registration results of (a) RCT and (b) $\mu\text{CT}$ with LV mask (red line); (c) Checker-board-like scheme visualization of these volumes. . . . .	95
4.6	Definitions of angles: (a) Angle difference of $\mu\text{CT}$ from RCT $\theta_1$ and (b) Inclination angle $\theta_2$ . . . . .	98

- 4.7 Mean and standard deviation of angle differences of  $\mu$ CT from RCT at sample points on each axial slice: Target axial slices were selected at 100-slice intervals along Z-axis (longest axis from apex to base) of RCT and  $\mu$ CT volumes. Each point on graph shows mean angle differences of  $\mu$ CT from RCT of a sample point on slice, and error bars represent standard deviation. Sample points on each slice were defined by a radial search scheme, explained in Section 4.5.2. Results do not greatly vary throughout the entire LV. Slice located at depth 8.85 mm is used for further evaluation in Figs. 4.8, 4.9 and 4.10 is pointed by arrow. . . . . 100
- 4.8 Angle differences of  $\mu$ CT from RCT on manually selected slice (depth = 8.85 mm. see Fig. 4.7): Colored cylinders show fiber orientations estimated from  $\mu$ CT volume and are colored according to angle difference of  $\mu$ CT from RCT . Fiber orientations estimated from RCT volume are also shown as white cylinders. . . . . 101
- 4.9 Fiber orientations on manually selected slice (depth = 8.85 mm. see Fig. 4.7) with coloring based on inclination angle: (a) RCT and (b)  $\mu$ CT. Cylinders show estimated fiber orientations, and colors represent inclination angles. . . . . 102
- 4.10 Relationship of inclination angles measured in RCT and  $\mu$ CT volumes. We manually selected slice (depth = 8.85 mm. see Fig. 4.7) and plot inclination angles measured on selected slice in this figure. Each circle is gray-scale coded based on outside ratio. From the figure, we can find positive correlation is clearly observed between inclination angles estimated from RCT and  $\mu$ CT volumes. Also, we can observe positive inclination angles in the outside area (epicardium). . . . . 103

4.11 Fiber tracking results with sagittal slice. Colors represent inclination angles. Two viewpoints were defined: one is useful for observing endocardium, and another is for epicardium. (a) RCT: Tracking was performed properly in entire LV. (b)  $\mu$ CT: Although closely resembling RCT results in (a), flat tracking results, densely gathered in joints, were produced due to scanning procedure, explained in Section 4.4.1. . . . . 106



# Chapter 1

## Introduction

### 1.1 Preface

Anatomy is the field of study that reveals the structures of bodies. Various imaging techniques have been developed and utilized for investigating anatomies, including endoscopes, X-ray computed tomography (CT), magnetic resonance imaging (MRI), and microscopes. Some imaging techniques are available for living bodies, including clinically available CT and MRI scanners.

In this thesis, we focus on the computational analysis of thorax anatomies. The thorax contains many anatomies, such as the bronchus, lungs, and heart, and each of these anatomies consists of various small structures. The heart consists of muscle fibers (cardiac fibers) and the structures of these cardiac fibers can be revealed by fiber tracking.

Although optical and electron microscopes have very high spatial resolution, they cannot be used for living bodies and usually produce 2-dimensional images of only a tiny region. It is challenging to understand 3D structures from microscopic images. However, 3D imaging techniques, including CT and MRI, do not have spatial resolution

comparable to that of microscopes. Thus, anatomies are vague and unclear on these images, especially for small tissues.

CT is widely used for 3D imaging of the thorax. Since CT imaging is based on X-ray absorption, contrast between air and non-air regions is high. However, some important tissues for clinical practices or anatomical investigations do not generate high contrast or clear edges.

This thesis's first topic is mediastinal lymph node detection from CT volumetric images (volumes). Lymph nodes are unclear and have low contrast on CT volumes. The proposed filter detects lymph nodes with a variety of appearances. Our second topic is cardiac fiber tracking from micro-focus X-ray CT ( $\mu$ CT) imaging. Since cardiac fibers do not clearly appear on  $\mu$ CT volumes, we evaluate the efficacy of  $\mu$ CT volumes for fiber tracking by a comparative study with a high-end imaging technique.

## 1.2 Goal

Investigating anatomical structures from 3D images (e.g., CT, MRI) is fundamental to understanding human and animal bodies. Our goal is to investigate the structures of various thoracic anatomies via computational anatomy in 3D.

Nevertheless, there are still challenging targets, especially for small anatomies that are vague and unclear on 3D images. One common characteristic between these anatomies is their unclear and vague appearance on images. These anatomies are physically smaller than large organs such as the lungs or heart. CT and MRI are feasible candidates for 3D imaging of anatomies in the human thorax. However, as shown in Table 2.1, their spatial resolutions are not as small as optical or electron microscopes. Smaller objects do not tend to be represented very clearly in these images and representing structures less than 0.1 mm (100  $\mu$ m) is not feasible.

Although microscopes may allow us to acquire very high spatial resolutions, there

are problems for volumes of interests. Microscopes are useful not for scanning the entire bronchus, but for observing the details of bronchial tissues [184]. Although microscopes can magnify a part of one lymph node [182, 183], these microscope images are not useful for detecting (finding and locating) scattered lymph nodes. There are many studies [189, 221, 222] in the histology of cardiac fibers using microscopes. However, microscopic images are not very useful for analyzing structures in 3D because they are usually 2D images.

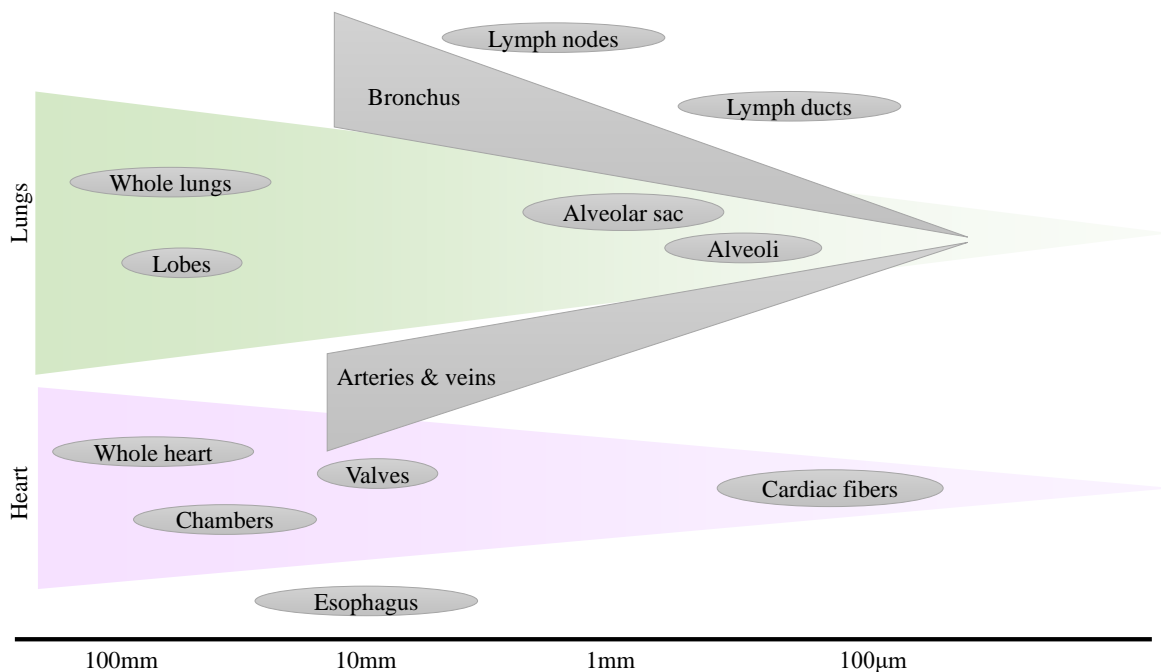


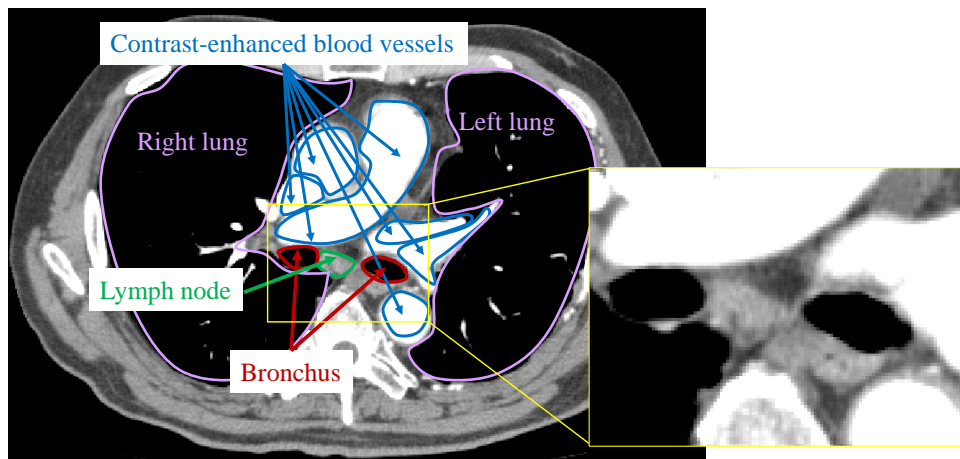
Figure 1.1: Anatomies in thorax respecting to physical size.

### 1.3 Computational analysis of thoracic anatomies

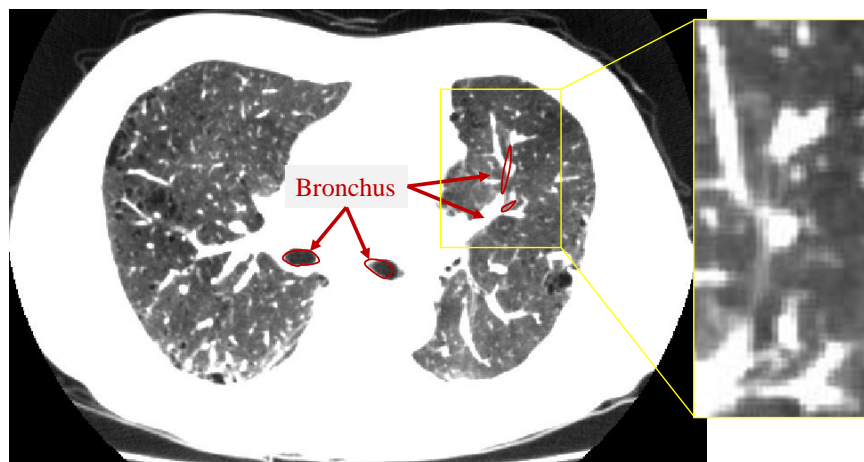
Computational anatomy (Section 2.1.5) helps us understand anatomies quantitatively. There are various anatomies in the thorax, as explained in Section 2.3. Approaches for imaging and computational anatomy vary for each anatomy. As summarized in Fig. 1.1, the sizes of these anatomies also vary. Generally, smaller anatomies tend to be more vague or unclear than larger ones on images acquired with the same imaging technique.

#### 1.3.1 Lungs

The lungs are filled with air. The absorption of X-rays in air is less than in bones or soft tissues. Thus, radiography and CT are widely used for lung imaging. Radiographs are utilized clinically, such as in thoracic X-ray examination. CT is also utilized when 3D



(a) Mediastinal window



(b) Lung window

Figure 1.2: Anatomies around the lungs on a CT volume. Spatial resolution is  $0.723 \times 0.723 \times 0.801 \text{ mm}^3$ . (a) Mediastinal window. Window width (WW) is 400 H.U. and window level (WL) is 0 H.U. (b) Lung window. Annotations of the bronchus cover limited parts on image. WW is 500 H.U. and WL is -800 H.U.

imaging is desired.

One straightforward anatomical understanding of the lungs by image processing is segmentation of the lung regions on radiographs or CT volumes (Figs. 1.2 (a)). Since these show high contrast between the inside and outside of the lungs, high-performance segmentation methods have existed since the early 1990s for radiographs [146] and CT

volumes [147]. Nowadays, deep learning methods, especially for fully convolutional networks [33] such as U-Net [249] are widely used for segmentation [54].

The lungs are divided into the two lobes (See Section 2.3.2). A segmentation method of the lobes based on 3D watershed transform was proposed in 2003 [145] and an atlas-based method was proposed in 2005 [140]. A segmentation method based on analyzing neighboring anatomies (the airway and vascular trees) was proposed in 2008 [141].

### 1.3.2 Bronchus

Radiographs and CT volumes of the lungs also show the bronchus. Segmentation of the bronchus has been widely studied. Segmentation methods based on region growing were proposed from the 1990s to the early 2000s. The region-growing method segments connected regions whose intensities are within a specific range. Adaptively setting the range for region growing [143] or introducing a cylindrical volume of interest [144] was proposed to improve robustness of the segmentation processes. Although many methods were proposed through the 2000s (summarized in EXACT'09 [119]), it was still difficult to segment the bronchus accurately to the deep branches. Deep branches tend to be thinner than the root; thus, they are often vague and have low contrast on CT volumes (Fig. 1.2 (b)). Accurate segmentation to deep branches is still challenging today [51–53].

Another imaging technique for the bronchus is an endoscope (2.2.2) called the *bronchoscope*. Inserting the bronchoscope into the bronchus allows us to acquire color images inside the bronchus. Since the camera only produces images observed from its current position, it does not obtain the shape or size of the entire airway tree. It is also difficult to locate the current position or pose of the bronchoscope. Shapes and sizes of entire airway trees are obtained by bronchus segmentation, as explained above. Therefore, the *virtual bronchoscopy* was introduced [157], which simulates bronchoscopic

images using the segmented bronchus from CT volumes. However, CT volumes may not contain detailed information that can be observed by bronchoscopes. Bronchoscopes are still useful for detailed diagnosis of the bronchus interior; therefore, bronchoscope tracking methods were proposed for locating the bronchoscope in the airway tree using electromagnetic sensors [154, 155], an image-based method [148, 149], and a hybrid of the two [156].

### 1.3.3 Lymph nodes

As mentioned above, the size of lymph nodes is crucial in lung cancer diagnosis. In the late 2000s, segmentation methods of each lymph node were proposed. Since the shape of each lymph node is ellipsoid- or spherelike, most segmentation methods use prior knowledge of these shapes, e.g., fast marching [104], [103] and graph-based [105]. However, there was a need to locate lymph nodes manually before starting segmentation using those methods.

Another difficult problem for both humans and computers is finding and counting lymph nodes from CT volumes. Not limited to the mediastinum, lymph node detection from CT volumes is widely studied with notable difficulties of size and small contrast (Fig. 1.2 (a)). Especially for mediastinal lymph nodes on CT volumes, there are many neighboring anatomies with very high or low intensities. From the late 2000s, filtering-based methods [101, 102] were proposed by assuming that lymph nodes have bloblike shapes and are slightly brighter than their surroundings.

### 1.3.4 Hearts

Both CT and MRI are widely utilized for 3D imaging of the heart. There are computational methods for both MRI and CT volumes.

For the whole heart or its chambers (Fig. 2.10), especially for the left ventricle, segmentation methods from MRI volumes have been actively studied. Thresholding-based segmentation [114] was proposed in 1995. In the late 1990s, segmentation methods using the active contour model [107, 113] were proposed. Use of the active counter model continued after 2000 [115]. Recently, deep learning has been widely introduced [117, 118] for MRI volumes. For CT volumes, approaches based on deformable models were further applied in the 2000s [109, 112]. Atlas-based segmentation methods [110, 111] were also proposed around 2010. Deep learning [108, 116] is currently being studied for CT volumes.

One important structure of the heart is the cardiac fibers, which are not described in any well-known gross anatomy book (Fig. 2.13) because of their small size. Neither MRI (Fig. 1.3 (a)) nor CT (Fig. 1.3 (b)) scanners for clinical purposes can acquire images of the cardiac fibers that can be observed due to their spatial resolution. One way to analyze fiber structures is to use diffusion-tensor magnetic resonance imaging (DT-MRI) [180, 234], which analyzes water molecules using an extended MRI technique. This work assumes that diffusions of water molecules are parallel to the fibers, which is difficult to confirm. Analyzing fibers from high-resolution 3D images is promising for a more straightforward analysis. It has been reported that ( $\mu$ CT) volumes of animal hearts for estimating fiber orientations can be utilized with the structure tensor [232].

## 1.4 Approaches for unclearly shown anatomies

Many thoracic anatomies are not clearly shown on 3D images, as listed in Table 1.1. Available 3D imaging techniques for bodies are usually limited to CT (Section 2.2.6) or MRI (Section 2.2.7). Especially for living human bodies, it is difficult to choose the best imaging technique for clearly showing only the analysis target anatomies. Even in animal experiments, the choice of imaging techniques may be restricted for various

Table 1.1: Analysis methods for anatomies or lesions in the thorax that are unclear on 3D images.

<b>Anatomy or lesion</b>	<b>Imaging technique</b>	<b>Analysis technique and application</b>
Mammary gland	CT	Segmentation by atlases [12], Segmentation by spectral clustering[8]
Breast lesions	MRI	Detection by convolutional neural network [11]
Breast cancers	MRI	Detection by Hessian-based filter [9]
Nonmass breast abnormalities	MRI	Characterization by graphs [10]
Bronchus	CT	Segmentation by region growing [142], Segmentation by Hessian-based filter [52]
Esophagus	CT	Segmentation by probabilistic model [133], Segmentation by atlas-based deep learning [134]
Mediastinal lymph nodes	CT	Detection by Hessian-based filter [101], Detection by 3D Haar-like features [132]
Lung nodules	CT	Detection by filter for cylinders [225], Detection by Hessian-based filter [231], Estimating malignancy by deep learning [230]
Heart chambers	MRI	Segmentation by atlases [229], Segmentation by deformable model [228]
Cardiac blood vessels	MRI	Segmentation by deformable models [226]
Cardiac fibers	$\mu$ CT	Fiber tracking by structure tensor [232]

reasons, such as cost, ethics, and technical difficulties. Our focus is on anatomical analyses, even if the target anatomies are not clearly shown on images.

Unclear images of target anatomies are mainly due to the imaging techniques' characteristics and anatomies' physical size. We selected several anatomies from Table 1.1 to discuss the causes of these unclear images and their current solutions.

### **1.4.1 Prior shape information: Cardiac chambers and blood vessels on MRI**

An MRI volume is generated by observing magnetic resonance many times. However, since the heart is in a living body and is continuously beating, the MRI scanner needs to observe the magnetic resonance only at a fixed beating phase over a long period (usually 30 minutes or more). Cardiac MRI volumes tend to be blurred due to the scanning time. Thus, on cardiac MRI images, most anatomies are blurred, particularly the boundaries between the blood vessels (e.g., aorta and pulmonary artery).

Since the shape of the heart and the cardiac blood vessels are almost fixed between patients, we can apply prior anatomical knowledge. Deformable models [226] or probabilistic atlases [227] are methods for introducing previous shape information.

### **1.4.2 Bloblike filters or texture features: Mediastinal lymph nodes on CT**

Mediastinal lymph nodes are bloblike regions around the major branches of the bronchus. Unlike the cardiac chambers or blood vessels, lymph node positions and numbers vary between patients; thus, introducing the probabilistic atlas [101] does not detect lymph nodes accurately.

One approach is to introduce filters for bloblike regions[100, 101]. However, there are many surrounding regions, such as air, soft-tissues, and blood vessels. It is not easy to clearly define the characteristics of mediastinal lymph nodes on CT volumes.

Mediastinal lymph nodes are very hard to detect only from their appearances. They have a similar attenuation coefficient to muscles and vessels. Both muscles and vessels cover a much larger volume of the body.

... Furthermore, the size of a lymph node can vary a lot.

Johannes Feulner, et al. [132]

Another approach is to utilize machine learning techniques to observe texture features, e.g., marginal space learning [123], Haar-like features with spatial priors [132], or convolutional neural networks [31].

### 1.4.3 Tubelike filters: deep branches on CT

The bronchus is an airway tree. Segmentation of the bronchus has been widely studied [48, 142]. Although only one airway tree exists in the body, its deep branches are challenging to find on CT volumes. Since the branches are spread all over the lungs, probabilistic atlases are not very useful.

Filters for tubelike structures have been widely studied. The Hessian-based filter [35, 120, 121, 126] is the most popular choice. Hessian analysis allows us to develop filters for a structure type (blob, line, or sheet) with specific sizes. Filtering methods based on Hessian analysis are still under improvement, e.g., Sukanya et al. [242] for vessels. Since some parts of the bronchus are not simple linelike, but are more cavity-like, Meng et al. [52] utilized the cavity enhancement filter [241].

The spatial resolution of clinical CT volumes is around 0.5 mm per voxel at best. Deep branches (the bronchioles) are often difficult to observe on CT volumes even with the human eye. This is because the bronchioles might be thinner than the resolution. Lee et al. [119] introduced a support vector machine (SVM) classifier, which offers additional segmentation results for separate parts on responses by a tubular-like filter, including Hessian analysis. It is desirable to segment until the disappearing points on CT volumes. Bian et al. [106] introduced an airway tracking scheme to continue to segment until the terminal branches.

#### 1.4.4 Structure tensor: cardiac fibers on $\mu$ CT

Micro-focus X-ray CT ( $\mu$ CT) volumes of animal hearts are promising for fiber tracking with the structure tensor [232]. Fiber orientation can be seen on  $\mu$ CT volumes due to the contrast between the fibers and their extracellular matrices. However,  $\mu$ CT images acquired by desktop-type low-end scanners are not clear for cardiac fibers and thus cardiac fibers may not be accurately analyzed due to the low contrast and unclear images. The contrast is generated between cardiac fibers and their extracellular matrices. These extracellular matrices consist of collagen, not air.

### 1.5 Topics

#### 1.5.1 Motivation

This thesis shows that computational anatomical structure analysis is possible, even if represented as unclearly on 3D images. The ability of 3-dimensional anatomical structure analysis is presented, even for anatomies that are unclearly shown on volumetric images.

The CT is widely utilized for 3D imaging of the thorax due to the amount of air in the thorax. High contrast between the air and non-air regions can be seen on CT volumes. However, some anatomies of the thorax do not contain or are not surrounded by air. While a variety of anatomies exist (Section 1.4), two anatomies satisfying

- observed on clinical or  $\mu$ CT volumes,
- unclearly shown because the contrast between the anatomy and the air is undependable for the analysis, and
- bloblike or fiberlike regions in the thorax.

are focused.

Topic 1 is mediastinal lymph node detection from CT volumes. Mediastinal lymph nodes are bloblike structures surrounded by various structures. A robust filtering technique is proposed for the accurate detection of those bloblike structures.

The clinical CT has a limitation of spatial resolution. Topic 2 is cardiac fiber tracking on  $\mu$ CT volumes. On  $\mu$ CT volumes, cardiac fibers can be observed, but they are unclearly shown. In addition to  $\mu$ CT's high spatial resolution, the contrast is generated by their extracellular matrices consisting of the collagen. Nevertheless,  $\mu$ CT is promising for anatomical studies of physically small structures. Evaluation of  $\mu$ CT's efficacy is conducted for anatomical analysis of fiberlike structures.

### 1.5.2 Topic 1: Mediastinal lymph node detection

This thesis proposes an automated lymph node detection method from chest CT volumes with experimental results. Although this is a computer-aided detection system method, the proposed filter focuses on anatomical structures with little effect from surrounding anatomies. Lung cancer is a leading cause of cancer death. Selecting proper treatment methods is crucial for the metastasis of lung cancer to the lymph nodes. Radiologists need to find lymph nodes manually, but this is very difficult because lymph nodes are small and vary in appearance and shape. Therefore, a novel filter for such small objects with vague appearances is essential for the accurate detection of lymph nodes.

Mediastinal lymph nodes are bloblike tissues. Not only are these regions filled with air (e.g., the bronchus and lungs), but there are a variety of neighboring areas, including soft-tissues and blood vessels. As mentioned in Section 1.4, filters for bloblike structures have had difficulty defining the target characteristics. We attack this problem using a filtering scheme that is robust for various surrounding regions.

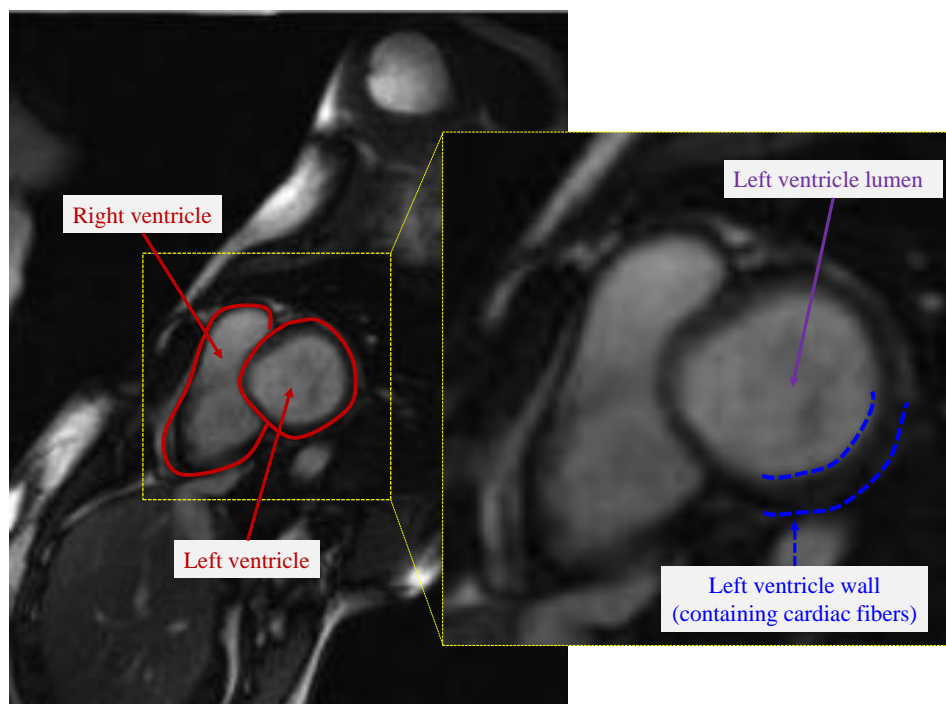
### 1.5.3 Topic 2: Cardiac fiber tracking

The heart consists of muscle fibers that are typically called cardiac fibers. Fiber tracking from  $\mu$ CT volumes of rabbit hearts is possible using structure tensor analysis for modeling. Fiber tracking results from  $\mu$ CT volumes are compared with those of refraction-contrast X-ray CT volumes, which have higher contrast resolutions than  $\mu$ CT. However, as mentioned above, discovering new imaging techniques is vital for obtaining detailed and broad information about the body. Although micro-focus X-ray (CT) imaging is promising for acquiring high-resolution images, cardiac fibers are blurred in CT images due to their low contrast resolution for soft tissues. It is crucial to evaluate the usefulness of these new imaging techniques.

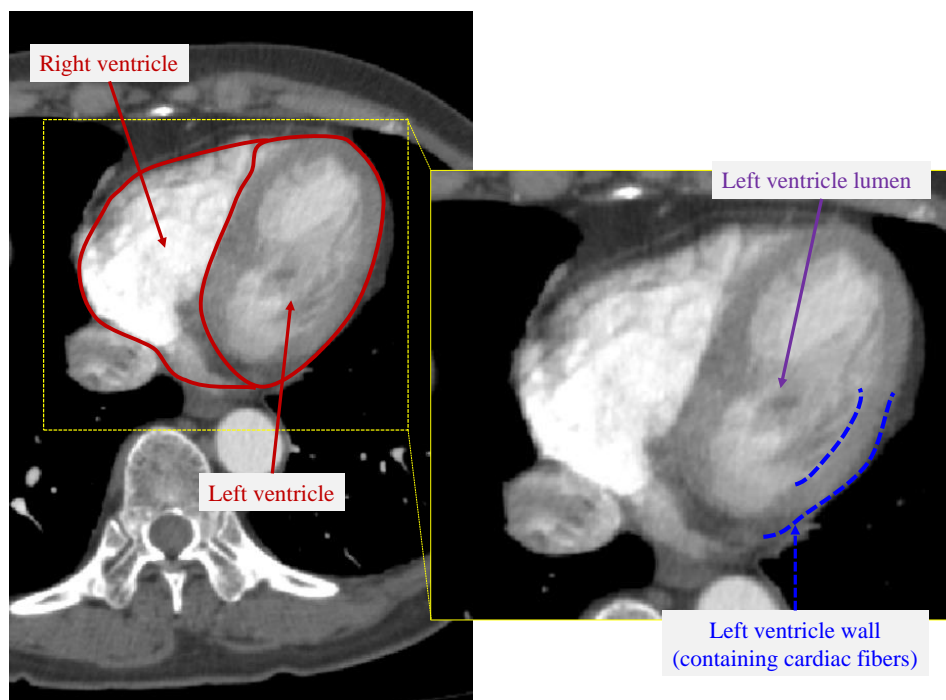
Cardiac fibers are shown on CT volumes and can be observed due to the contrast with the extracellular matrices. However, extracellular matrices mainly consist of collagen. Although the structure tensor can be used for fiber tracking, the reliability of the results has not yet been confirmed. We evaluate the reliability of the results from CT volumes of the heart by comparing them with other high-end imaging techniques.

## 1.6 Thesis structure

This thesis consists of five chapters. Chapter 1 provides the motivations of the research as an introduction. Chapter 2 describes background information, including anatomical study fields, imaging techniques for anatomical studies, and thoracic anatomies. Chapter 3 describes the mediastinal lymph node detection method. Chapter 4 describes cardiac fiber tracking from  $\mu$ CT volumes, and Chapter 5 provides a summary and discussion of future work of this thesis.



(a) MRI



(b) CT

Figure 1.3: CT and MRI volumes of the heart. (a) MRI (T1-weighted) volume. Figure 1 in [216] with annotation by this thesis's author. Spatial resolution is  $1.37 \times 1.37 \times 8.0 \text{ mm}^3$ . (b) CT (arterial phase) volume. Spatial resolution is  $0.644 \times 0.644 \times 0.801 \text{ mm}^3$ .



## Chapter 2

# Anatomical studies and computational analysis

### 2.1 Anatomy

Anatomy studies the parts of organisms, including organs, bones, and tissues. The word “anatomy” is sometimes used as a noun to represent an item inside a body. A famous anatomical book states that anatomy consists of a variety of fields and is vital for medicine.

Anatomy includes those structures that can be seen grossly (without the aid of magnification) and microscopically (with the aid of magnification). Typically, when used by itself, the term *anatomy* tends to mean gross or macroscopic anatomy – that is, the study of structures that can be seen without using a microscope.

... Anatomy forms the basis for the practice of medicine.

Susan Standring, et al. [85] pp. 2



(a) Cardiac valves by Leonardo da Vinci

(b) Heart by Gempaku Sugita

Figure 2.1: Illustrations of anatomy until modern age. (a) Leonardo da Vinci's illustration of cardiac valves (Fig. 3 on [137]). (b) Gempaku Sugita's illustration of heart (Fig. 1.2 on [139], pp. 32)

There are currently many famous books describing anatomy [27, 67–69, 83–85]. To date, both research and education in anatomy have improved through various approaches worldwide [138].

### 2.1.1 Anatomical studies until modern age

Anatomy originated in ancient Egypt around 3100 BC. [82]. Hippocrates (c.460 c.370 BC), the founder of scientific medicine in ancient Greece, dissected animals [55]. In Alexandria, Herophilus (c. 335 c. 280 BC) and Erasistratus (c. 304 c. 250 BC) dissected human bodies [60, 61] to investigate bodily structures. They described the nervous system, cerebrum, and cerebellum. Hippocrates and Herophilus are called “the Father of Medicine” and “the Father of Anatomy,” respectively [205].

Galenus (Galen, c. 129 c. 200) was a famous clinician in ancient Rome, where the

dissection of human bodies was prohibited. Galenus published many anatomy reports based on animal dissections. Over 20 volumes of those reports remain today [208]. Knowledge of the nervous system did not extensively progress until Herophilus and Erasistratus. For instance, Galenus discovered the seven cranial nerves and the spinal nerves, and found that paralysis occurs when the spinal cord at the point related to the paralyzing position is injured. Galenus' medical knowledge formed the basis of anatomy until the Renaissance.

Until the Renaissance, anatomy was not very actively investigated [207]. In Europe, the dissection of human bodies began in the 14th century. Mondino de' Liuzzi (c. 1270 c. 1326), an Italian anatomist, is known as "the Restorer of Anatomy." He argued the importance of "understanding through practice." de' Liuzzi conducted the first documented public dissection after an absence of more than 1700 years. In the 16th-century, Leonardo da Vinci dissected human bodies with accurate sketches of his work (Fig. (a)). Andreas Vesalius (1514-1564) was a Belgian anatomist who published many reports on the dissection of human bodies [204]. He is regarded as a founder of the science of anatomy based on observations gained using a scalpel on human cadavers. He published a series of seven books called the "De Humani Corporis Fabrica" that contains observant illustrations. Govard Bidloo (1649-1713) was a Dutch anatomist who published a book on human anatomy entitled "Anatomia Humani Corporis" in 1685, in which he described the lipomyelomeningocele in detail.

The study of a wide variety of regions and aspects of the body began in the ancient era. For instance, regarding the lymphatic system, lymph nodes and vessels containing milky fluid had already been observed in the pre-Renaissance era, including by Hippocrates [62]. Bartolomeo Eustachi was a famous scientist who described many anatomies, including one of two lymph ducts, the thoracic duct [63, 81], in the 14th century.

Not only was anatomical research actively investigated, but education was also been

widely provided all over the world. In the 18th century, German anatomist Johann Adam Kulmus published an anatomical book entitled *Anatomische Tabellen*. Its Dutch translation was further translated into Japanese and published as it *Kaitai Shinsho* by Gempaku Sugita and Ryotaku Maeno (Fig. 2.1 (b)). Another famous book of the 18th century, *Anatomy of the Human Body*, was published by British anatomist William Cheselden.

### 2.1.2 Gross anatomy

*Gross anatomy* is the study of bodies and their parts at the visible or macroscopic level [71]. *Anatomy* is often synonymous with gross anatomy (See Section 2.1).

Gross anatomy is also called *macroscopic anatomy* due to its macroscopic observation. There are many organs and tissues, such as bones, organs, and vessels. Observing these anatomies macroscopically allows us to understand their sizes, positions, shapes, and roles. Gross anatomy can be studied from various points of view, such as regional and systemic approaches [85].

#### Regional approach

Anatomical study from the regional approach is sometimes regarded as the subcategory *regional anatomy* [70]. The body can be divided into *regions*, e.g., the thorax, abdomen, and head. The thorax contains the lungs, heart, thoracic skeleton, walls, etc.

#### Systemic approach

Another point of view is as a *system*. The body consists of systems including the nervous, skeletal, muscular, lymphatic, reproductive, gastrointestinal, and respiratory systems. Although each system is not inside a *region*, it works integrally. The respiratory system

consists of the head, neck, and thorax. The nervous, skeletal, and lymphatic systems cover the entire body.

### 2.1.3 Surface anatomy

*Surface anatomy* [77] observes bodies externally. It is sometimes regarded as a subcategory of gross anatomy. Even without dissection or imaging, it is possible to observe many anatomies, such as the hair, eyes, skin, and nails. Bodies can posture in various styles.

It is not just about knowing what lies under the skin and which structures are perceptible to touch in a living body, it is also about enabling learners to improve their skills in clinical examinations, interventional procedures, and interpretation of diagnosing images.

Veronica Papa, et al. [78] pp. 167

### 2.1.4 Microscopic anatomy

Microscope magnification is efficient for investigating small anatomies (See Section 2.2.3). Microscopic anatomy (histology) is the study of small bodily structures, primarily with the use of microscopes, in contrast to the macroscopic approach of gross anatomy. Microscopes allow us to observe tiny tissues in bodies, such as cells. Marcello Malpighi (1628-1694) [64, 79] is a pioneer of *microscopic anatomy*.

The British scientist Robert Hooke first observed plant cells in the 17th century [72]. However, further microscopic exploration was not well conducted for almost 200 years. In the 19th century, Theodor Schwann and Matthias Jakob Schleiden used microscopes to observe animals and cells, respectively [73]. Together, they established the cell theory, arguing that all parts of animal and plant bodies are made up of cells. Marcello

Malpighi described many small anatomies, including the renal glomeruli [65], pulmonary capillaries, and alveoli [80].

### 2.1.5 Computational anatomy

Nowadays, computational techniques allow us to investigate anatomies. This field is called *computational anatomy*:

Computational anatomy is an emerging discipline deriving from medical anatomy and several other sciences and technologies, including medical imaging, computer vision, and applied mathematics. The main focus of the discipline covers the quantitative analysis and modeling of variability of biological shapes in human anatomy in health and disease.

...

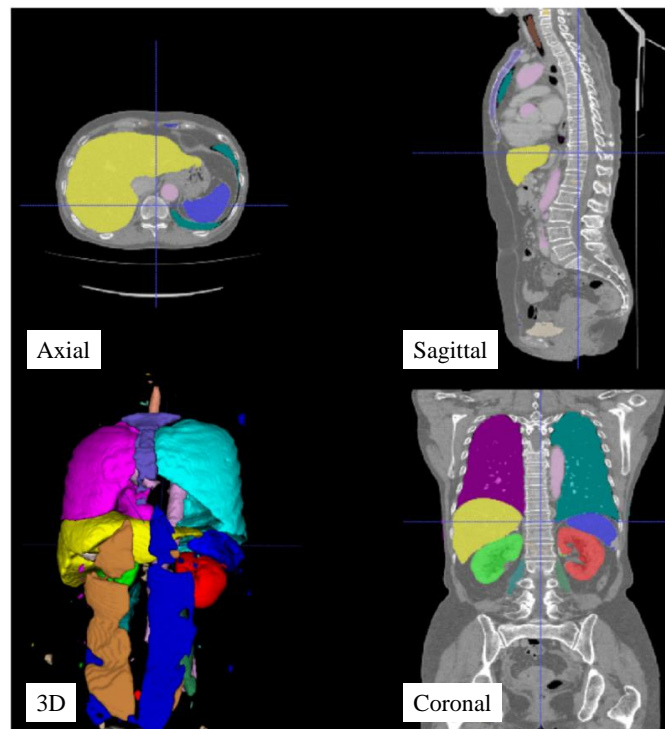
reliable and automated segmentation schemes for all organs in medical images are necessary for detecting abnormal structures and surgical planning.

Yoshitaka Masutani, [74] pp. 2

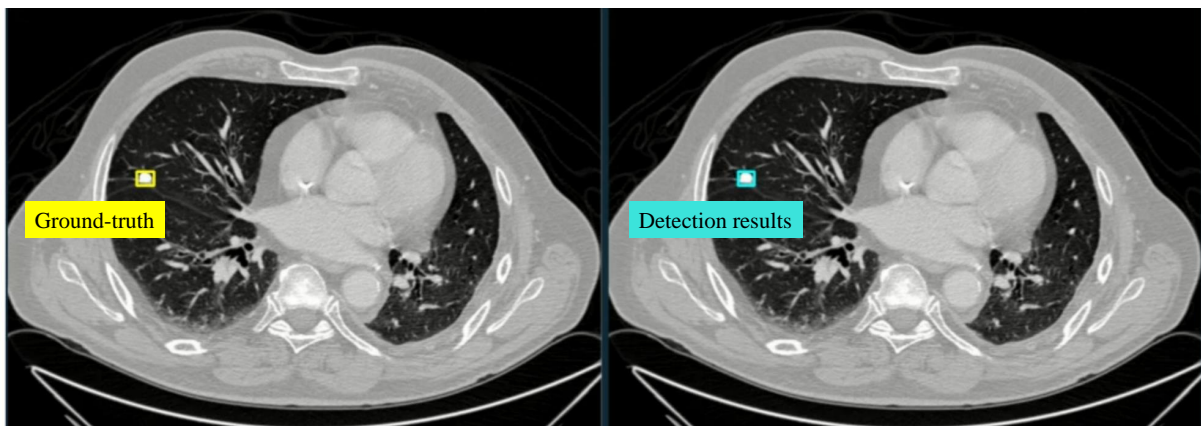
Nowadays, computational techniques allow us to investigate anatomies. This field is called *computational anatomy*:

## 2.2 Imaging for anatomical studies

One way of investigating (gross) anatomy is through dissection. Today, the dissection of human bodies is considered important education for medical students [59]. For ethical reasons, dissection has often been avoided or prohibited [55]. Since dissection is usually restricted to cadavers or experimental animals, the cost, techniques, and environment make it difficult to perform.



(a) Organ segmentation



(b) Lung nodule detection

Figure 2.2: Medical image processing for observation of anatomies. (a) Organ segmentation from CT volumes. Figure obtained from [32] with additional notes. (b) Lung nodule detection from CT volumes. Figure obtained from movie frame in [26] with additional notes.

Another method is to utilize imaging techniques (medical imaging). Acquiring images allows us to observe and record anatomies. There are currently many types of imaging techniques available for medical imaging. As listed in Table 1.1, many imaging techniques can be applied to anatomical studies (Table 2.1).

Table 2.1: Typical characteristics of imaging techniques. All resolutions are approximate values for each imaging technique's main target. Exceptions also exist for other characteristics.

Section	Technique	Observation target	Spatial resolution	Typical use on medicine
2.2.1	Optical camera	Visible light	Vary	Body surface
2.2.2	Endoscope	Visible light	1 $\mu\text{m}$ –1 mm	Diagnosis inside bodies (e.g., airways, intestines, etc.)
2.2.3	Optical microscope	Visible light	Depending on magnification ratio (100nm [75]–)	Cells or local structures on glass slides
2.2.4	Electron microscope	Electron	0.1 nm [76]–	Viruses or inside cells on glass slides
2.2.5	(2D) Radiograph	X-ray	0.1-1 mm	Diagnosis inside bodies
2.2.6	X-ray computed tomography (CT)	X-ray	250 $\mu\text{m}$ [28]–	Diagnosis inside bodies
2.2.7	Magnetic resonance imaging (MRI)	Magnetism	0.1 mm [29]–	Diagnosis inside bodies
2.2.8	Scintigraphy	$\gamma$ -ray		Diagnosis for specific purposes (e.g., bone metastasis [30])
2.2.9	Ultrasonography	Ultrasound	100 $\mu\text{m}$ [46]	Real-time diagnosis inside bodies (e.g., embryo, heart)

### 2.2.1 Optical camera

Cameras are used not only for medical, but also many other purposes, such as artistic photographs, television, and surveillance. Cameras observe the visible light coming in through the lens. Historically, films made from gelatin silver or similar techniques were used for recording this light. Videos can be generated by recording many images over a period of time, in a manner similar to flipbooks. The Kinetoscope and Cinematographe, invented in the 1890s, play videos by displaying a series of many images in a timeline. However, these techniques produce analog images, which are not easily handled by computers. Digital images can be generated by sampling and quantization. In digital images, each image is represented as an array. A component of the array is called a pixel (in 2D) or voxel (in 3D).

The digital camera was invented in 1975 by Steve Sasson [56]. Presently, digital cameras (Fig. 2.3 (a)) utilize a charge-coupled device (CCD) image sensor to observe lights and record images as a digital representation. Each image (picture) is divided into an array of pixels and the pixels are represented as intensity values. It is possible to generate color images by observing intensities at red, green, and blue (RGB) color wavelengths individually and recording them as different channels.

The optical camera is not very suitable for observing inside the bodies of humans, animals, or plants. This is because human skin and most other objects reflect visible light. There are, however, various ways to observe inside of bodies, as mentioned below.

### 2.2.2 Endoscope

The endoscope is a medical device for observing the internal organs of living bodies. Most endoscopes are tube shaped so that they are insertable into the body. A camera installed at the top of the endoscope allows clinicians to observe the interior of the body.

A type of endoscope for the thorax is a *bronchoscope* (Fig. 2.3 (b)). The broncho-

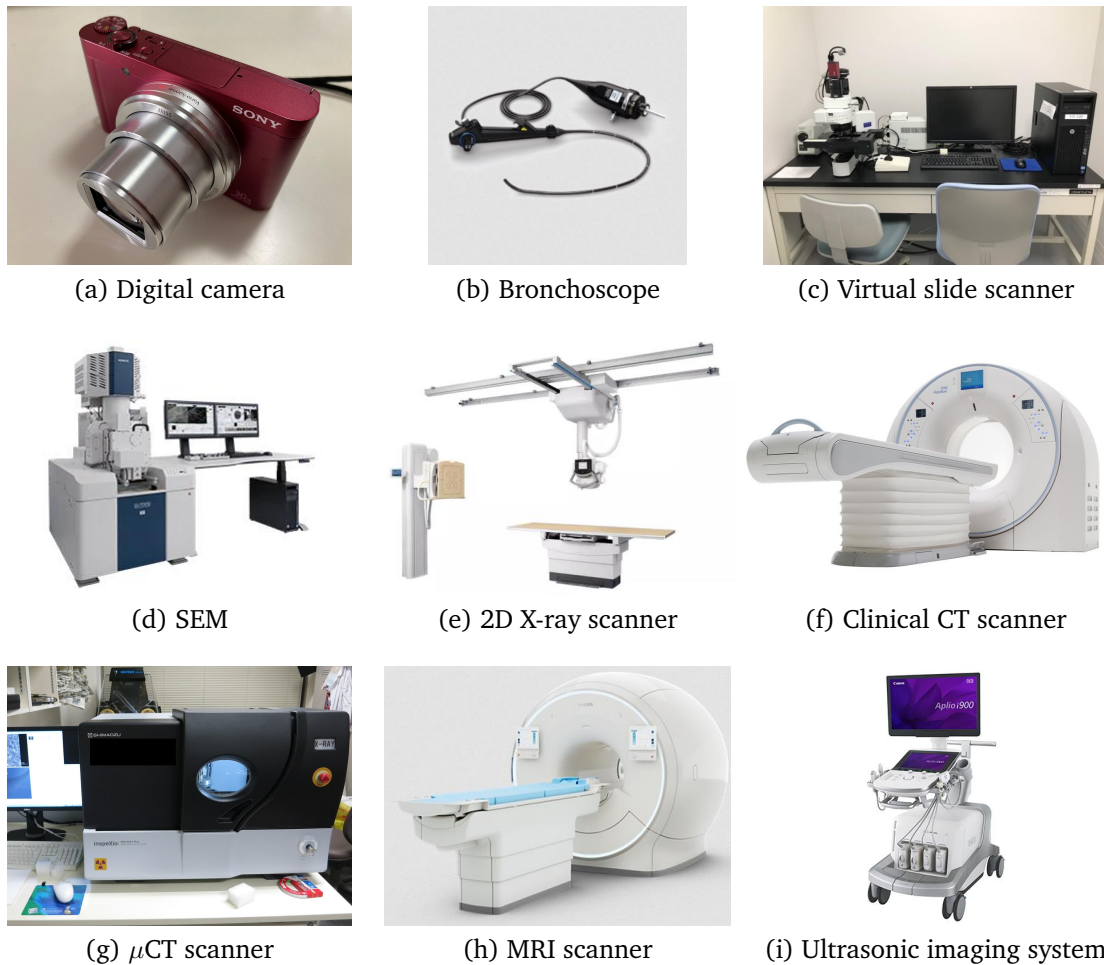


Figure 2.3: Imaging techniques. (a) Digital camera, DSC-WX500 (Sony, Japan). (b) Bronchoscope, BF-XT190 (OLYMPUS, Japan). Figure from [23] (c) Virtual slide scanner, VS120 (OLYMPUS, Japan). Figure from [23] (d) Electron microscope, SU7000 (Hitachi High-Tech, Japan). Figure from [25] (e) 2D X-ray scanner, DigitalDiagnost (Philips, Netherlands). Figure from [20] (f) Clinical CT scanner, Aquilion ONE / GENESIS Edition (Canon Medical Systems, Japan). Figure from [21] (g)  $\mu$ CT scanner, SMX-90CT Plus (Shimadzu, Japan). (h) MRI scanner, Ingenia Elition 3.0T X (Philips, Netherlands). Figure from [22] (i) Ultrasonic imaging system, Aplio i900 (Canon Medical Systems, Japan). Figure from [24].

scope is inserted through the nose or throat. The camera at the top of the bronchoscope allows us to observe the interior of the bronchus. The bronchoscope is widely utilized

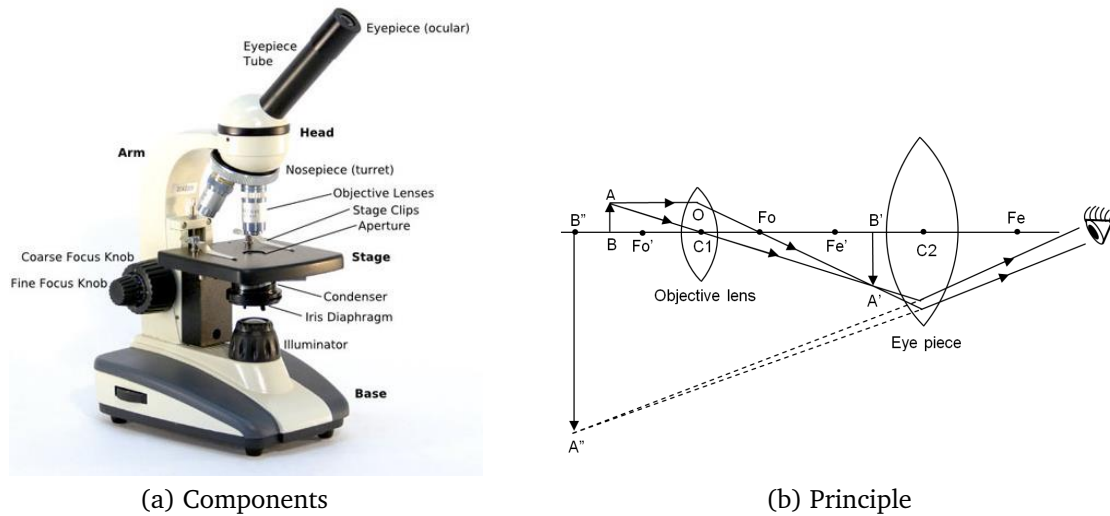


Figure 2.4: Compound optical microscope. (a) Components of compound optical microscope. Figure from [167] (b) Working principle. Real image ( $A'B'$ ) is generated by objective lens ( $C1$ ) for object ( $A-B$ ). From real image ( $A'B'$ ), eye piece ( $C2$ ) generates virtual image ( $A''-B''$ ) which can be observed by eye. Figure from [168]

for clinical purposes, including diagnosis [224] and surgery [223].

### 2.2.3 Optical microscope

Optical microscopes are used for observing tiny structures, e.g., cells. Acquiring microscopic images is useful for pathology, histology, and biology. These microscopes magnify objects, making these objects much easier to visualize than in their original size.

Optical microscopes that are consisting of multiple lenses are called compound optical microscopes. The sample is usually prepared on a microscope slide, a rectangular glass of  $75 \times 26 \text{ mm}^2$ . The compound optical microscope consists of many components (Fig. 2.4 (a)), including a light source, a stage, an objective lens, and an ocular lens. A light source kindles the microscope slide installed on the stage. A halogen lamp or an electronic light is often used as a light source. An objective lens facing the sample collects light from the sample ( $A-B$  on Fig. 2.4 (a)) and generates a real image ( $A'B'$ ) on

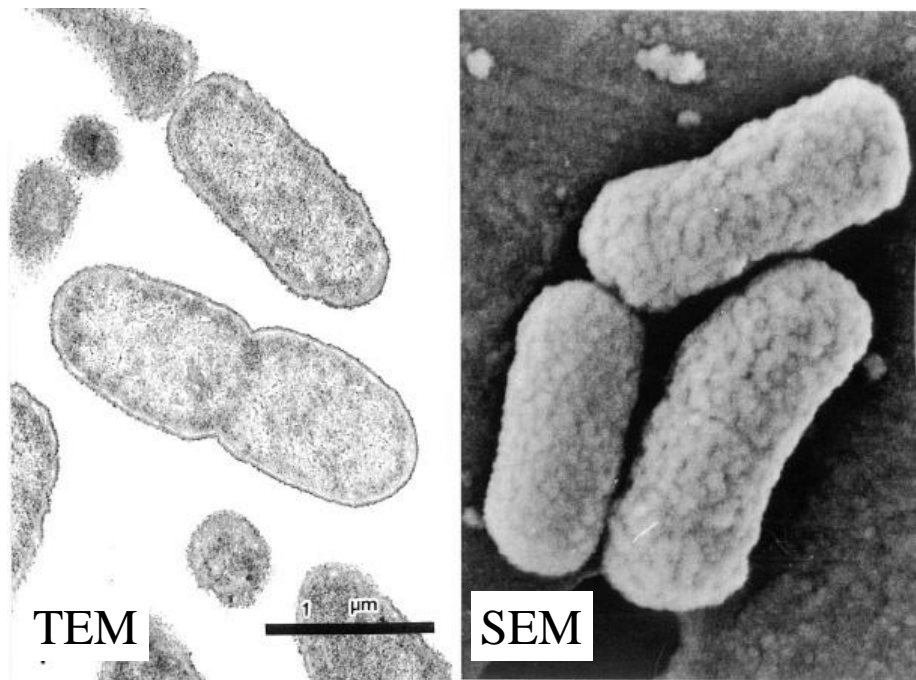
Fig. 2.4 (a)) inside the microscope. The eye piece (ocular lens) magnifies the real image (A-B on Fig. 2.4 (a)) as a virtual image (A''-B'' on Fig. 2.4 (a)) that can be observed by an eye. A digital optical microscope utilizes the CCD instead of the ocular lens to produce digital images.

Typical microscopes focus only on a limited part of a glass slide. Digital microscope images consist of many pixels for visualizing tiny regions. Typical microscopes focus only on a limited part of a slide. Virtual slide imaging (VSI) scanners (Fig. 2.3 (c)) are utilized for a vast space of glass slides. VSIs allow us to observe an entire glass slide as one digital image. 3D imaging techniques based on optical [244] or electron [243] techniques have been studied. However, there are still many limitations compared to CT (Section 2.2.6) or MRI (Section 2.2.7) for 3D imaging. One approach for 3D imaging is stacking and aligning many neighboring slice images [206]. However, it is very challenging to accurately align these images to view as a volume since there are many differences between neighboring slices. The banana effect [206] is a known alignment difficulty. Even if we accurately stack and align, it is infeasible to acquire a volume with isotropic resolution. The resolution along slices has to depend on slice thickness, which would be far lower than the axes on each slice.

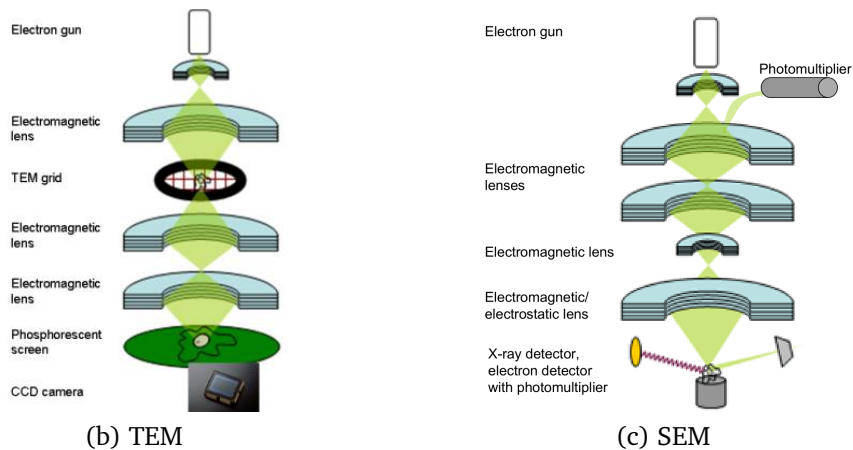
## 2.2.4 Electron microscope

Electron microscopes (Fig. 2.3 (d)) utilize the electrons. There are two common scanning techniques: transmission electron microscopy (TEM) and scanning electron microscopy (SEM). Electron microscopes can achieve much higher spatial resolution than optical microscopes. Electron microscopes are used to observe viruses or the inside of cells.

The TEM (Fig. 2.5 (b)) is utilized for observing inside a sample prepared as a very thin surface (100 nm or less). The sample is installed on the TEM grid. Tiny objects can



(a) TEM and SEM images



(b) TEM

(c) SEM

Figure 2.5: Electron microscopes: transmission electron microscopy (TEM) and scanning electron microscopy (SEM). (c) SEM and TEM images of escherichia coli O-157. Figure from [169] with annotations by thesis' author (a) TEM. Part of Fig. 2.1 in [66] (b) SEM. Part of Fig. 2.2 in [66]

be observed, e.g., viruses, DNA. The electron gun generates electron beams towards the sample. The electromagnetic lens (condenser) concentrates the electron beams

and exposes them to the sample. Subsequent electromagnetic lenses magnify the electron beams that have passed the sample. The CCD camera records the image generated on the phosphorescent screen.

The SEM (Fig. 2.5 (c)) is useful for SEM can observe a wider area than the TEM. Electron beams generated by the electron gun are focused on the sample installed on the stage. When the electron beams are projected, X-rays and secondary electrons spread from the projected point. Images are generated by observing those X-rays and electrons observed by their detectors with photomultipliers. The secondary electrons are often utilized for biological samples [66] because secondary electrons escape only from the samples' surface.

### 2.2.5 (2D) Radiograph

In 1895, Wilhelm Rontgen discovered X-rays [58]. X-ray is an electromagnetic wave that permeates through most non-metal objects well. Images acquired by X-ray are called *radiographs*. Wilhelm Rontgen used photographic plates for acquiring radiographs. The first radiograph was of Wilhelm Rontgen's wife's hand, which clearly showed the bones and a ring on a finger [57].

Radiographs are currently used for many medical purposes. X-ray scanners (Fig. 2.3 (e)) are commonly used in medical examinations. For instance, radiographs are essential for detecting abnormalities, e.g., a pulmonary nodule, on medical tests. X-rays uniformly explode from an X-ray generator to the target object to acquire radiographic images. Photographic plates, films, and detectors receive X-rays passed through the target objects at the opposite side of the X-ray generator.

The absorption of X-rays occurs severely in tissues that densely consist of large atomic numbers. The bones and teeth have significant X-ray absorption because they densely contain calcium ( ${}_{20}\text{Ca}$ ), whose atomic number is 20. Soft tissues mostly consist

of low atomic numbers, e.g., hydrogen ( ${}_1\text{H}$ ), carbon ( ${}_6\text{C}$ ), and oxygen ( ${}_8\text{O}$ ). Air has minimal X-ray absorption. Usually, regions with large X-ray absorption appear brighter than areas with small absorption. Bones and teeth are therefore bright, air and air-filled organs (e.g., the lungs) dark, and soft-tissues somewhere in the middle.

Because radiographs are 2D images, many objects overlap with radiation exposure. For instance, the heart, lungs, ribs, and blood vessels overlap each other on chest radiographs.

### 2.2.6 Computed Tomography (CT)

Computed tomography (CT) is an imaging technique that solves the issues of (2D) radiographs mentioned in Section 2.2.5. CT generates images on sections of objects without physical cutting and it is possible to generate a 3D CT image (volumetric image, volume).

Projections of X-ray absorption from many angles are required for generating CT images. Reconstruction algorithms [34, 36] construct a volume from the projections along with many angles. As with (2D) radiographs, large contrasts are observed between the bones, soft tissues, and air.

#### History

CT scanning was initially invented by the British engineer Godfrey Hounsfield while working for Electrical and Musical Industries Ltd. (EMI) [212]. He learned the basics of electronics and radar science while in the Royal Air Force. After World War II, he entered EMI and began working on weapons, radars, and computers. In the late 1960s, he focused on 3D imaging based on X-rays and developed a CT scanner. Two radiologists, James Ambrose and Louis Kreel, assisted Godfrey Hounsfield with radiological knowledge and testing samples.

In 1971, computed tomography angiography (CTA) scanning was performed on a preserved human brain, a fresh cow brain, and Godfrey Hounsfield's brain. The first patient was a woman suffering from a suspected frontal lobe tumor [203]. The scanner at this time took 4.5–20 minutes for each 180-degree scan. The CT volumes consisted of slices of  $80 \times 80$  pixels, with a spatial resolution of  $3 \times 3 \times 13 \text{ mm}^3$ . In 1979, Godfrey Hounsfield and an American Physicist, Allan MacLeod Cormack, won the Nobel Prize in Physiology or Medicine. Allan MacLeod Cormack proposed a reconstruction algorithm from X-ray images acquired from various angles [202].

Although another 3D imaging technique called magnetic resonance imaging (MRI) started to become common in the 1980s, improvement of the CT scanning technique has continued with several significant innovations up to today [211]. Spiral scanning introduced in 1989 replaced slice-by-slice scans for generating a stack with real 3D images. Today, an entire body can be scanned within 5–20 seconds at a spatial resolution of less than 1 mm.

### Principle

Highly-dense materials with high atomic numbers tend to cause strong attenuation of the X-ray. The CT estimates the attenuation coefficient at each point in the sample. Note that the following description is mainly based on pp. 191–192 in [127].

The Radon's theorem is the basis of generating images of materials' sections. According to Radon's theorem, projection data from all angles allows us to reconstruct the images of materials' sections.

The X-ray is projected from the X-ray tube to the sample. The X-ray detector existing at the opposite side of the X-ray tube records the radiation dose. The projection data is calculated by comparing the projected and recorded radiation doses. When a projected and recorded radiation doses were  $I_0$  and  $I_d$ , respectively, the projection data value

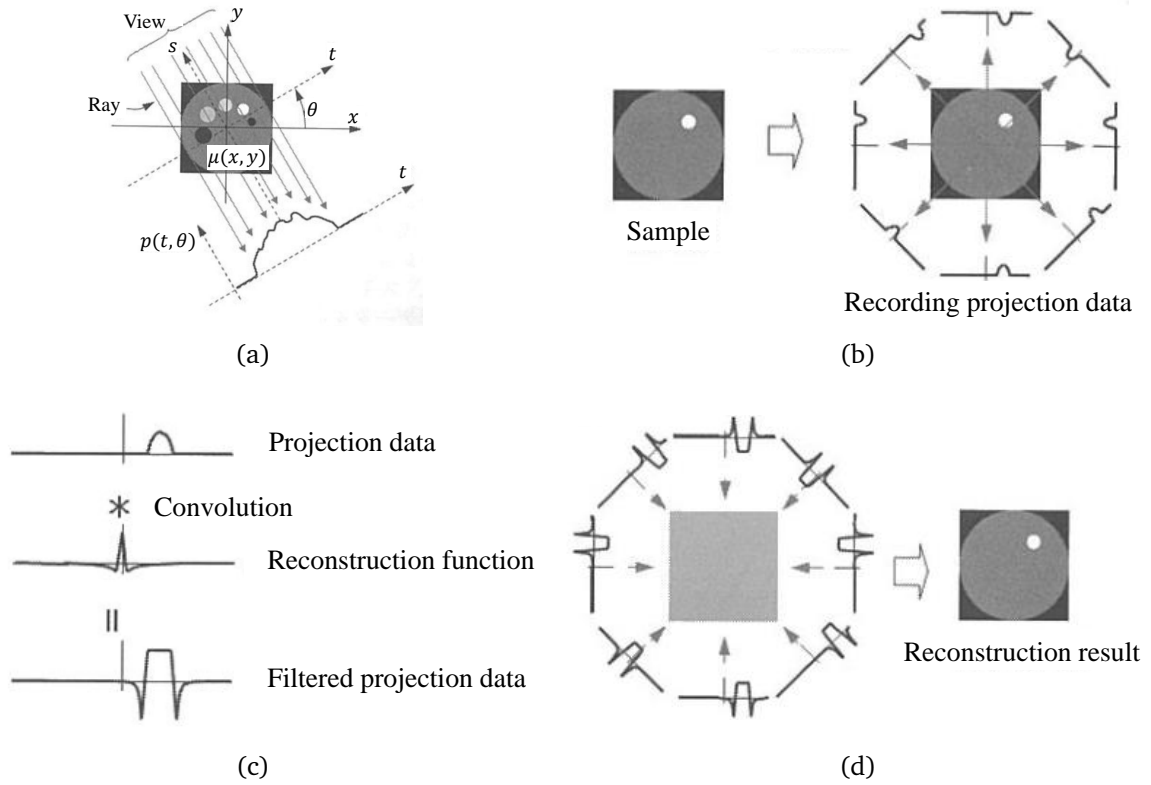


Figure 2.6: Principle of CT reconstruction with filtered-back-propagation (FBP). Figs. 4 and 5 on pp. 191-192 in [127] with modifications by thesis' author. (a) Recording projection data. (b) Recording projection data from various angles. (c) Filtering. (d) Reconstruction with FBP.

$p(t, \theta)$  is calculated (Fig. 2.6 (a)) by

$$I_d(t, \theta) = I_0(t, \theta) \exp \left[ - \int \mu(x, y) ds \right] \quad (2.1)$$

$$= I_0(t, \theta) \exp[-p(t, \theta)] \quad (2.2)$$

$$\therefore p(t, \theta) = - \ln \left[ \frac{I_d(t, \theta)}{I_0(t, \theta)} \right] \quad (2.3)$$

where  $t$  represents the distance from the origin, and  $\theta$  represents the projected angle.

A widely used reconstruction algorithm is filtered-back-projection (FBP). The pro-

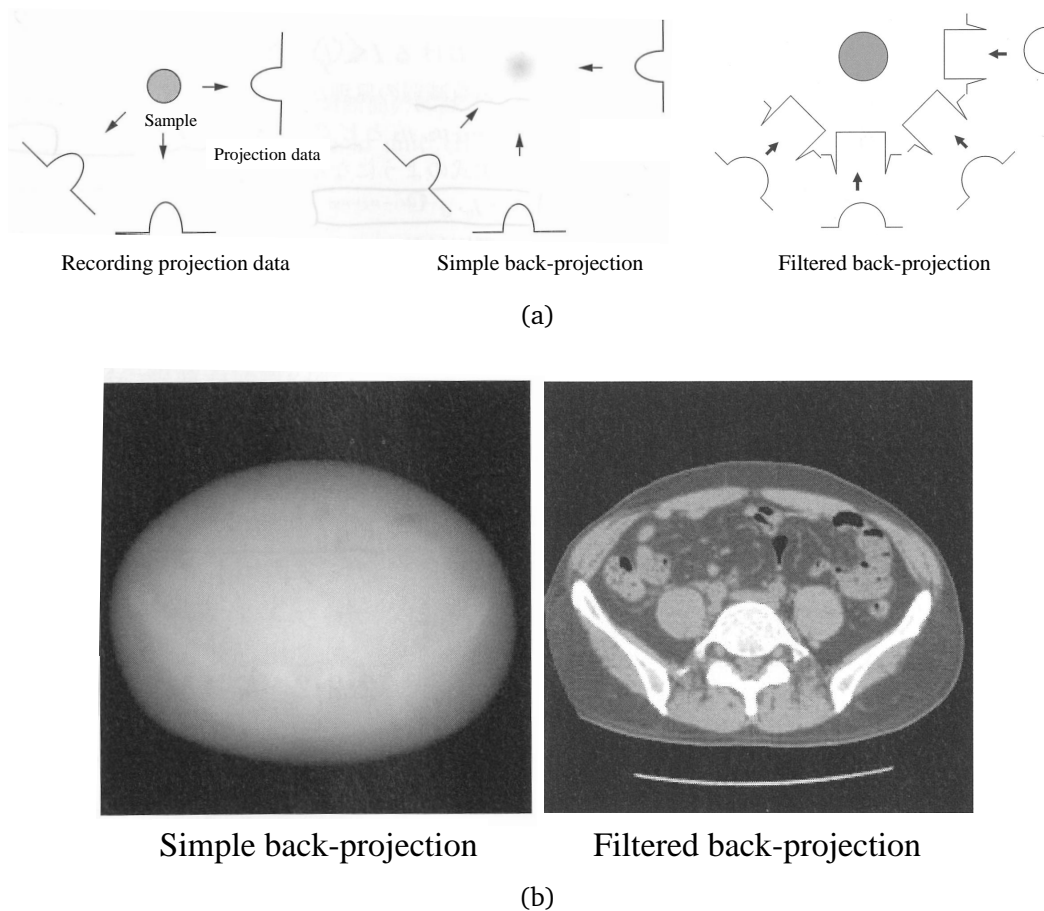


Figure 2.7: Efficacy of filtering. Parts of Fig 2.3, 2.4, 2.5, and 2.6 on [190] with modifications by thesis' author. (a) Schematic illustrations. Simple back-propagation generates blurred images, while filtered back-propagation generates much more clear images. (b) Reconstruction results of abdominal CT volume.

jection data from various angles (Fig. 2.6 (a)(b)) allows us to reconstruct results by simple back-projection. However, the reconstruction results are blurred. Therefore, a reconstruction function is convoluted on the projection data (Fig. 2.6 (c)), and then back-projection is performed (Fig. 2.6 (d)). Reconstruction functions control the characteristics of results. Figure 2.7 shows the efficacy of filtering.

### **Clinical CT**

CT scanners for the human body are sometimes called clinical CT scanners (Fig. 2.3 (f)). The Hounsfield Unit (H.U.) is a unit for clinical CT intensity values that represents radiodensity. It is a quantitative scale that represents -1000 for air and 0 for water. 3D and 4D CT scanning have become ubiquitous in clinical practice. Spatial resolution is currently around 0.5 mm or smaller.

### **Micro-focus X-ray CT ( $\mu$ CT)**

While clinical CT is commonly utilized in clinical practice, its resolution is limited to a millimeter scale. A higher resolution is sometimes required for anatomical, biological, or pathological studies. Moreover, requests for non-destructive inspection exist in engineering. These inspections may require observing much smaller structures, such as cotton tissue or concrete.

Micro-focus X-ray CT ( $\mu$ CT) (Fig. 2.3 (g)) is a CT scanner that has a higher spatial resolution than clinical CT. The X-ray detector can acquire high-resolution projection images than clinical CT.

The X-ray source's focal spot size, the detector's size, and the system's geometry affect the spatial resolution [188]. To make  $\mu$ CT's spatial resolutions higher than clinical CT's, the X-ray detector can be developed densely, and the target object can be smaller than the human body. Reconstruction results from high-resolution images also become high-resolution. Also, if scanners are not for living bodies, X-rays with high radiation doses can be utilized.

$\mu$ CT is clinically utilized in dentistry [186, 187]. Furthermore,  $\mu$ CT is widely used in engineering, for example, in non-destructive inspection [37, 47] and structure investigation [38, 45]. It is also useful for observing natural objects [44] such as plants [43], small animals [39, 40], and insects [41, 42].

### 2.2.7 Magnetic resonance imaging (MRI)

Magnetic resonance imaging (MRI) (Fig. 2.3 (h)) is another 3D non-destructive imaging technique [210]. MRI imaging has many advantages over CT, such as high contrast for some tissues and no X-ray exposure. Major disadvantages are difficulties for patients with internal metal hardware or pacemakers, low contrast for bones, and low spatial resolution. Furthermore, since the scanning time is longer than with CT, MRI is not suitable for moving organs such as the lungs. In contrast, MRI is utilized widely for the head, breasts, and limbs.

The atomic nuclei (proton) of some atoms are magnetic (Fig. 2.8 (a)). MRI focuses on hydrogen, found in water and fat. Usually, these protons are directed arbitrarily.

When a static magnetic field is projected onto the material, proton precession begins and the protons start to rotate rapidly. The frequency of rotation is called the Larmor frequency, which depends on the static magnetic field's strength. The protons' magnetic vector is now directed parallel to the static magnetic field (z-direction) and the rotating protons are now called spins. Along the z-axis, a slightly larger number of spins are now directed in the z-direction than those in the opposite direction.

An electronic pulse, called the 90-degree pulse of the Larmor frequency, is projected perpendicular to the static magnetic field (Fig. 2.8 (b)). This 90-degree pulse causes resonance between spins. In other words, the phases between the spins are fixed. Furthermore, the spins are directed in the same direction as each other along the z-axis. The magnetic vectors generated by the protons are now directed onto the x-y plane. When the 90-degree pulse stops, the protons return to the rotation without resonance (Fig. 2.8 (c)). The relaxation along the z-axis (T1-relaxation) requires more time than the relaxation along the x-y plane (T2-relaxation).

Spin-echo is a widely utilized method of MRI imaging. Fig. 2.8 (d) shows an example of a time sequence. A 90-degree pulse is generated at  $t_{\text{ex}90}$ . After a time  $\frac{TE}{2}$

from the 90-degree pulse, another pulse named 180-degree pulse is generated. “TE” represents the echo time. After another time  $\frac{TE}{2}$ , a large signal called the echo is largely observed. The time between subsequent 90-degree pulses is called “TR”, representing the repetition time.

Coordinates in the images are assigned by changing the frequencies and phases for different positions. In addition to the static magnetic field, the gradient coils offer a gradient magnetic field. The gradient magnetic field can have different strengths for different positions. Offering the gradient magnetic field along the x-axis allows us to change the spins’ frequency according to each position’s strength (frequency encoding). Spin phases can be changed by assigning the gradient magnetic field along the y-axis for a very short time (phase encoding).

T1- and T2-weighted images are types of MRI images widely used in clinical diagnosis. These images have different characteristics for different materials. For both T1- and T2-weighted images, fat is bright, and bones and blood flow are dark. Water is dark and bright on T1- and T2-weighted images, respectively. Mucus has the inverse characteristic of water.

### 2.2.8 Scintigraphy

Scintigraphy is a 2D imaging radiology technique generated by the radiopharmaceuticals injected into the body. A radiopharmaceutical is a drug containing a radioactive isotope (RI). Gamma cameras pick up the gamma-ray generated from the radiopharmaceutical.

$^{123}\text{I}$ -metaiodobenzylguanidine (MIBG) scintigraphy uses a radiopharmaceutical that behaves similarly to norepinephrine (noradrenaline). Norepinephrine acts as a neurotransmitter in the body. The injected  $^{123}\text{I}$ -MIBG clusters at cancers originating in the adrenal medulla or nervus sympathicus. MIBG scintigraphy is often used for the diag-

nosis of these cancers, e.g., melanocytomas and neuroblastomas.

### **SPECT and PET**

Single-photon emission computed tomography (SPECT) and positron emission tomography (PET) are 3D imaging techniques for nuclear medicine. Sometimes SPECT and PET are separately regarded as scintigraphy due to their 3D imaging. These 3D imaging techniques are often integrated with a general clinical CT scanner as a SPECT-CT or a PET-CT scanner.

A radiopharmaceutical is injected into the patient before SPECT or PET scanning is performed. This scheme is different from clinical CT, which records X-rays irradiated from the source outside the bodies.

For instance, PET uses the radiopharmaceutical fluorodeoxyglucose F 18 ( $^{18}\text{F}$ -FDG) is utilized for cancer diagnosis [209].  $^{18}\text{F}$ -FDG is a derivative of glucose, which contains the positron-emitting nuclide  $^{18}\text{F}$ . Since cancers tend to consume a lot of glucose,  $^{18}\text{F}$ -FDG gathers around the cancer and this cancer can be detected in the PET images.

### **2.2.9 Ultrasonography**

Ultrasonography [181] is another imaging technique used inside living bodies. One crucial feature is real-time imaging. The scanning system (Fig. 2.3 (i)) is usually much simpler and easier to operate than CT or MRI and there is no X-ray exposure.

The pulse-echo technique is used for most general ultrasonographic imaging [214]. An ultrasound pulse is sent from the probe to the body. The pulse reflects off the surface of an object as an echo. The distance between the probe and the object is then estimated by the return time of the echo. The propagation velocity of ultrasound is assumed to be constant in the body. Images generated based on the echo strengths are called B-mode images and are common in the medical field.

## 2.3 Thoracic anatomies

### 2.3.1 Exploring thorax

In this thesis, we focus on the thorax. The thorax contains the lungs and the heart, which are essential for the respiratory and circulatory systems, respectively. In brief, the heart receives blood from the entire body, passes the blood through the lungs to receive oxygen, removes the carbon dioxide, and then pushes the blood back through the entire body. The bronchus is an airway tree between the lungs and outside the body.

The thorax is the part between the neck and the abdomen (Fig. 2.9). The breasts are located on the front outside of the thorax (Section 2.1.3). The breasts, bones including the ribs (thoracic skeleton), and muscles are located under the skin. From the systemic approach, the breast belongs to the reproductive system (Sec. 2.1.2).

There are well-known and large organs in the region covered by the thoracic skeleton: the bronchus, lungs, and heart (Fig. 2.10). These three organs are situated near each other and strongly correlate via many arteries and veins. However, from a systemic viewpoint (Sec. 2.1.2), the heart belongs to the circulatory system, while the bronchus and lungs belong to the respiratory system.

In the following, several major thoracic anatomies are briefly described.

### 2.3.2 Lungs

The lungs are the organs for transferring the oxygen from the air to the blood and releasing the blood's carbon dioxide to the air. The lungs are divided into the left and right lungs, as shown in Fig. 2.10. The right lung is divided into three lobes, the superior, middle, and inferior lobes. The left lung consists of only two lobes, the superior and inferior lobe. The right lung is larger than the left lung [172]. The sizes of the lungs change with breathing, as they expand and contract when air is inhaled and

exhaled, respectively.

### 2.3.3 Bronchus

The bronchus is the airway tree that provides air to the lungs. The root of the bronchus (*trachea*) lies between the left and right lungs. The trachea's diameter size is around 12 mm [86] depending on the person and sex. The trachea branches into the left and right lungs (Fig. 2.11 (a)). Each branch further branches several times in the lungs and deeper branches tend to be thinner than their parents. These branches run parallel to the pulmonary arteries. Terminations of the branches consist of the alveolar sacs and the alveoli, which are similar in shape to raspberries (Fig. fig:netterBronchus (b)). The lymph nodes, including the mediastinal lymph nodes, reside beside the bronchus (Fig. 2.12).

### 2.3.4 Lymph nodes

The lymph nodes are tissues for the lymphatic system. Bacterias, viruses, and cancer cells in the lymphatic fluid are cleaned. Numbers of lymph nodes exist all over the body and are bloblike in shape. The region between the left and right lungs is called the *mediastinum*. One group of lymph nodes, called *mediastinal lymph nodes*, exist beside the airways (Fig. and 2.12 annotated in Fig. 2.10). Although reported sizes in the anatomical reports vary ([150–152]), each mediastinal lymph node is usually less than 10 mm in diameter.

For lung cancer diagnosis, it is essential to check lymph node size since lymph nodes metastasized by cancers are enlarged. “10 mm” is the clinical size threshold for checking metastasis [153] in diagnosing lung cancer.

### 2.3.5 Heart and blood vessels

The heart is an organ that pumps blood to the entire body and the lungs. The heart is located below the bronchus and between the lower parts of the lungs. It consists of four chambers: the left ventricle, right ventricle, left atrium, and right atrium. Sizes and shapes change frequently during beating. These chambers are connected to blood vessels. There are also valves for directing blood flow.

Pulmonary arteries and veins spread throughout the lungs. The roots of these arteries and veins are connected to the heart. The pulmonary arteries carry deoxygenated (low oxygen concentration) blood from the heart's right ventricle. After the lungs reduce carbon dioxide and increase oxygen concentration in the blood, the blood returns to the heart's left atrium and is moved to the left ventricle via the mitral valve. The blood is then pushed out throughout the body through the aortic valve and aorta (an artery). During its course through the body, the blood is deoxygenated. The deoxygenated blood first returns to the right atrium through the superior vena cava vein and then to the right atrium via the tricuspid valve.

The heart consists of muscles (cardiac muscles) for pushing out the blood to the lungs and body. It continues to work constantly through life without resting. For efficient blood circulation, the cardiac muscle fibers (cardiac fibers) consist of complicated structures [173, 174]. Unfortunately, such structures are not well illustrated or explained in any well-known gross anatomy book (Fig. 2.13).

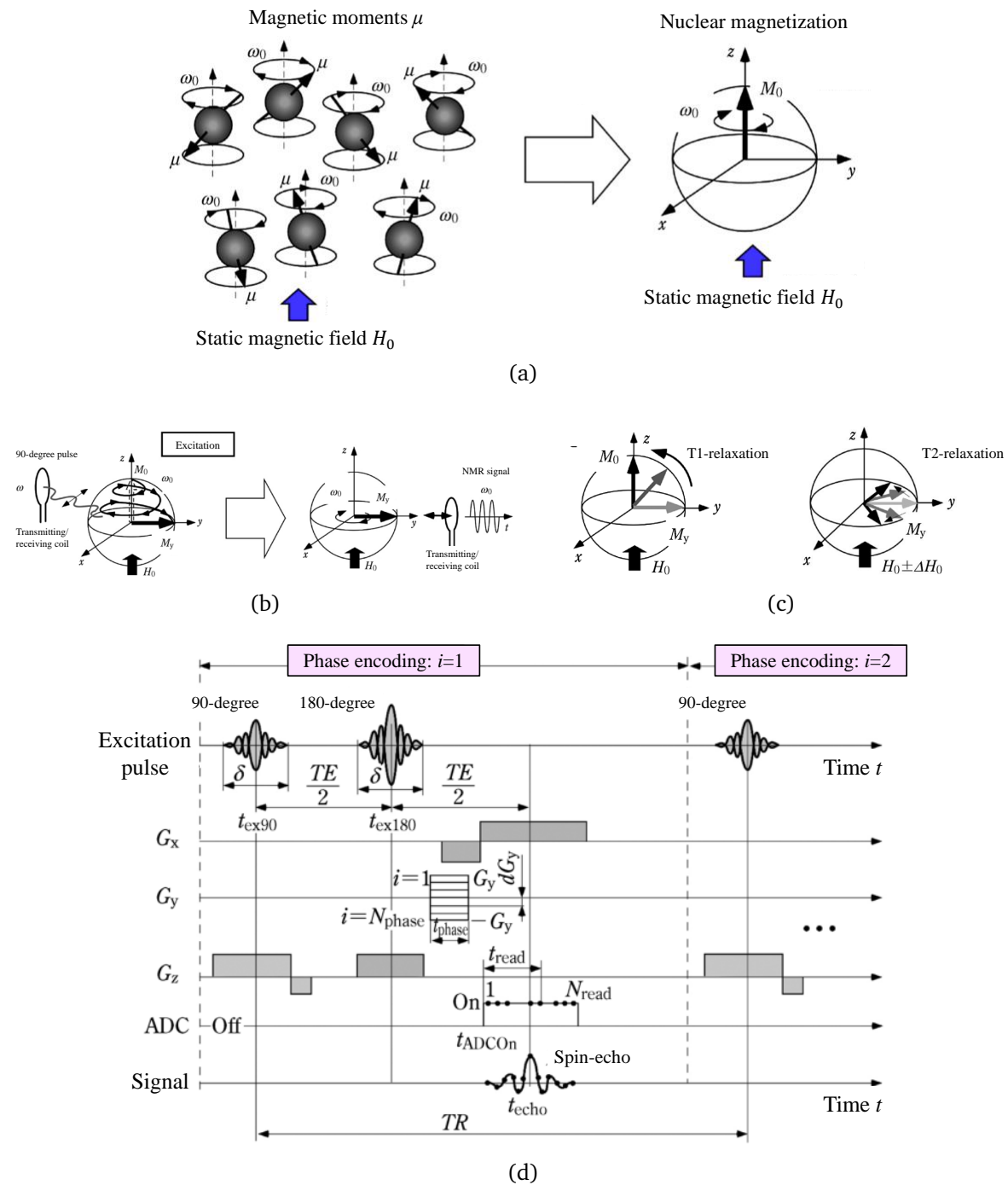


Figure 2.8: Basics of MR imaging. Figures 1, 2, 4 and 5 on [185] with modifications by thesis' author. (a) Protons and nuclear magnification. When static magnetic field  $H_0$  is offered, magnetic field  $M_0$  generated by protons directs along  $z$ -axis. (b) Excitation. When 90-degree pulse is given, magnetic vectors lie on  $x - y$  plane. (c) T1- and T2-relaxations. (d) Example of time sequence for spin-echo method.

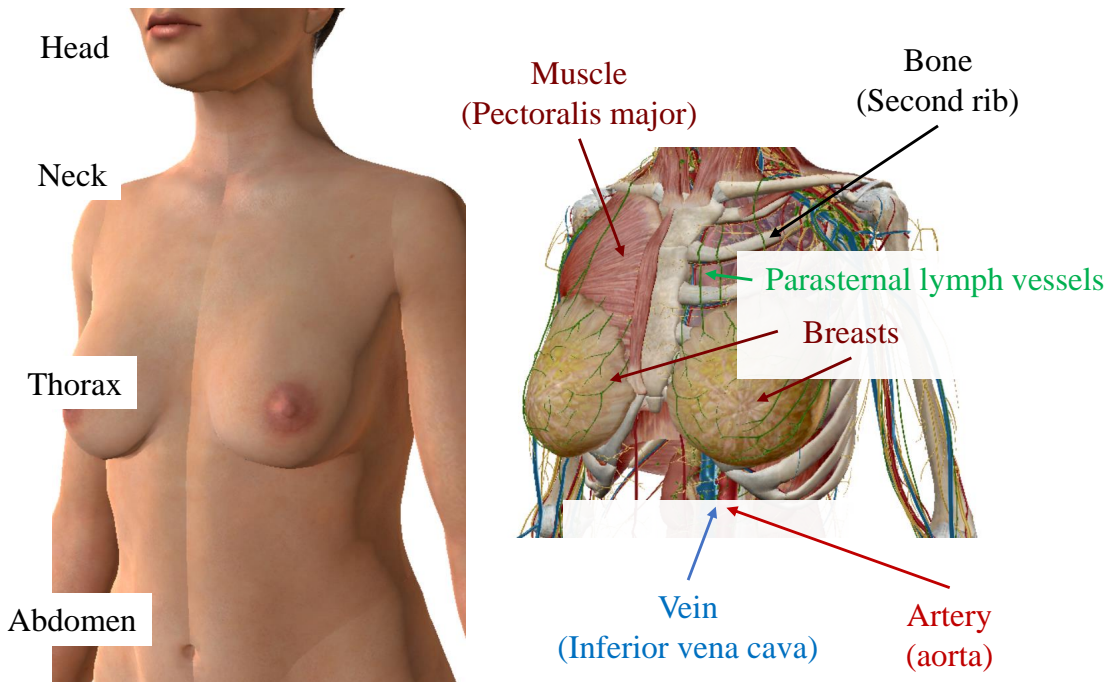


Figure 2.9: Body surface and major anatomies around thorax. Image courtesy of Visible Body [50] (annotations by author of thesis).

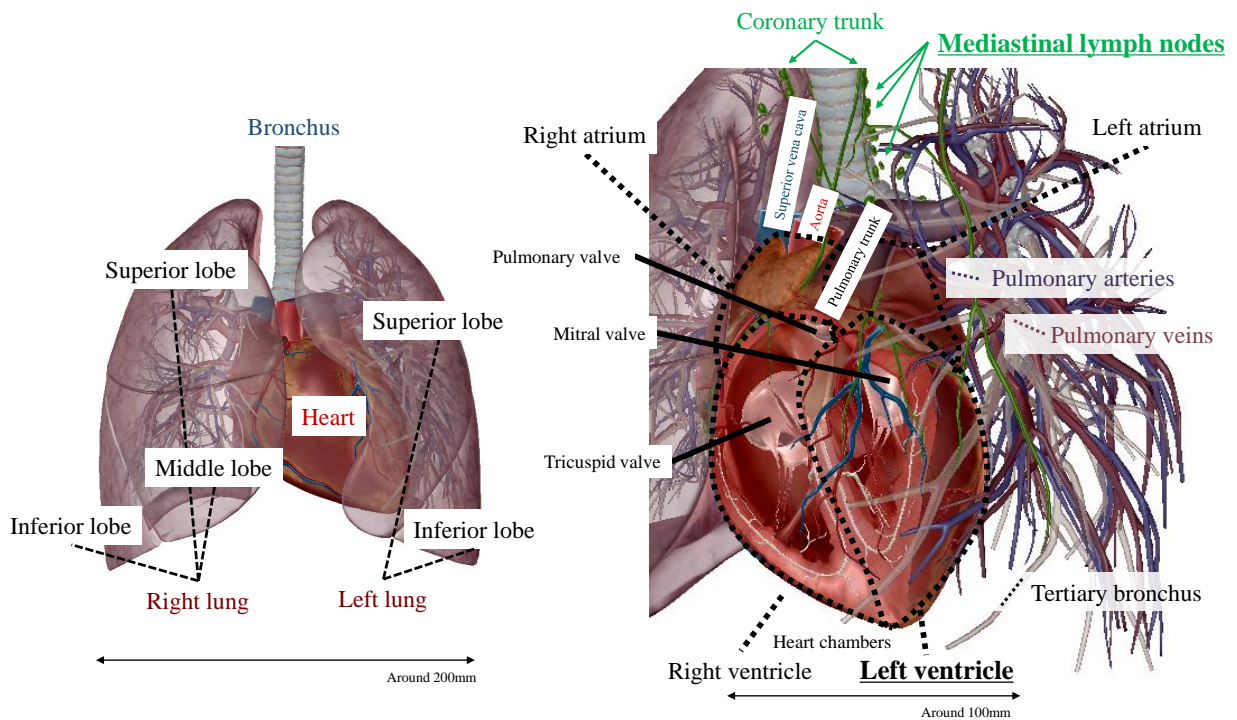
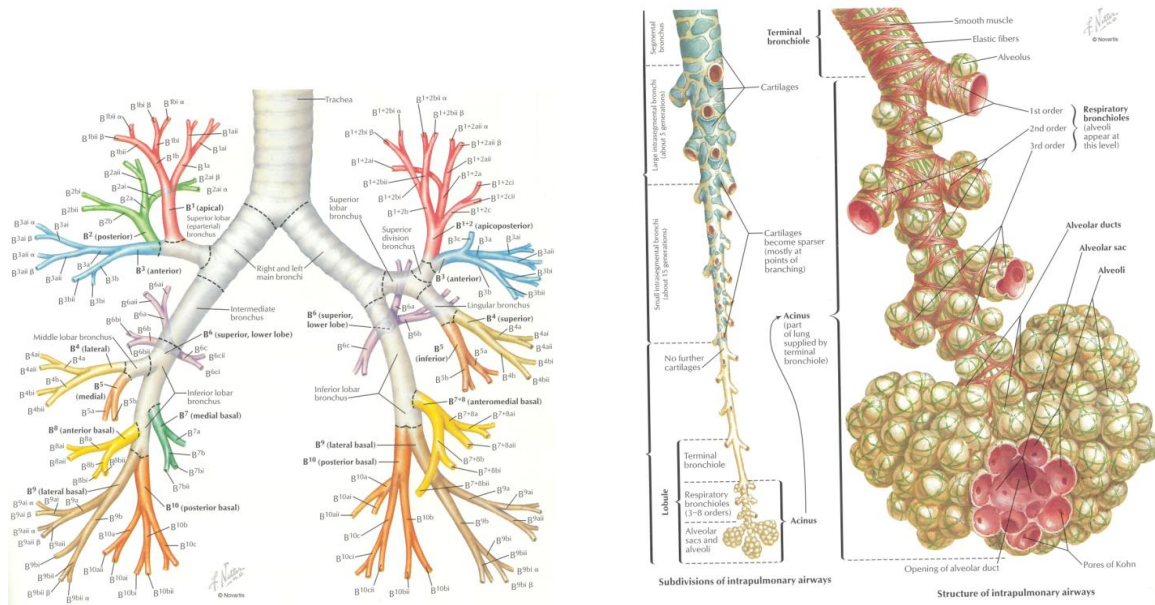


Figure 2.10: Organs (lungs and heart), bronchus and their surroundings. Image courtesy of Visible Body [50] (annotations by author of thesis).



(a) Entire bronchus (pp. 191 in [27]).

(b) Around termination of branches (pp. 192 in [27]).

Figure 2.11: Detailed illustrations of bronchus. (a) Entire bronchus. (b) Around termination of branches.

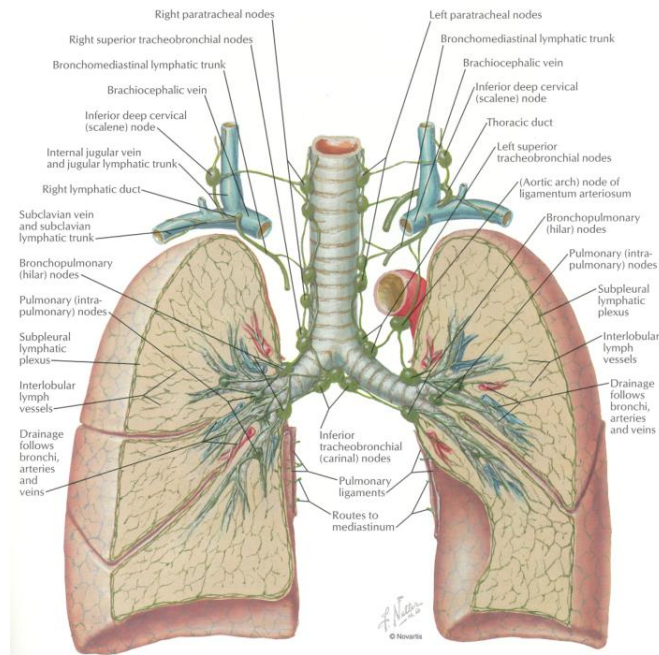


Figure 2.12: Detailed illustrations of lungs, bronchus and surrounding lymph nodes and vessels (pp. 197 in [27]).

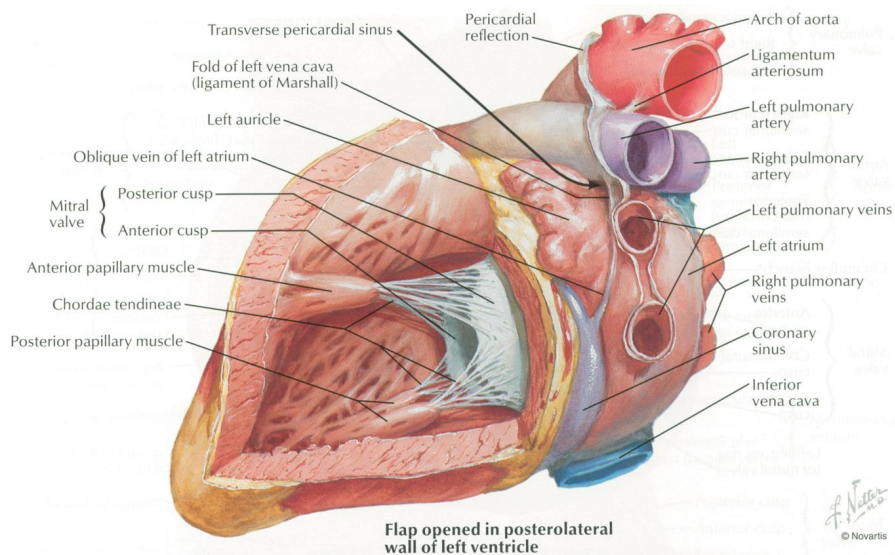


Figure 2.13: Detailed illustrations of the left ventricle of the heart (pp. 209 in [27]).

## 2.4 Computational anatomy in thorax

### 2.4.1 Motivations of focusing on thorax

We focus on the thorax since diseases of the thoracic anatomies are responsible for many deaths each year. It is essential to understand thoracic anatomies by computational techniques for further medical study and to ensure proper treatment.

Japan's Ministry of Health, Labour and Welfare (MHLW) reports the numbers and causes of death every year. According to an MHLW report [1], 1,381,093 people died in 2019. The top five causes of death were cancers (27.3 %), cardiac diseases (15.0 %), senile decay (8.8 %), cerebrovascular diseases (7.3 %), and pneumonia (6.9 %). Cardiac diseases occur in the heart, while pneumonia is an inflammation of the lungs. Some cancers of the thoracic anatomies prove fatal. The top five cancers causing death were of the lungs (20.0 %), stomach (11.4 %), pancreas (9.7 %), colon (9.5 %), and breasts (4.0 %). The lungs and breasts are thoracic anatomies.

### 2.4.2 Assistance of clinical practices

Generally, it is essential to find diseases or lesions as early as possible. Frequent health examinations are recommended. In Japan, some examinations, such as chest X-ray imaging and urinalysis, are legal requirements for employees (Industrial Safety and Health Act). Cancer is of significant interest in these health examinations. If possibilities of disease are detected, further examinations are considered.

As mentioned in Section 2.4.1, cancer can be fatal. When cancers or their precursors are detected, careful diagnosis and precise treatment are essential. Some cancers are difficult to detect until they grow large. Sometimes cancers metastasize to the lymph nodes or other areas. The TNM Classification of Malignant Tumors (TNM) criterion is used to recognize the spread of cancer. Cancers and their metastases to the

lymph nodes or other organs are considered in the TNM. Clinicians create a treatment plan by recognitions based on the TNM. The major treatment methods include surgery, chemotherapy, and radiotherapy. Multidisciplinary therapy is also commonly planned. To properly plan treatment based on the TNM, it is essential to observe the cancer's current growth. However, there is a potential for oversight or misdiagnosis when reviewing medical images. For instance, it has been reported that 25% of lung cancers are overlooked in chest X-ray diagnoses [2]. The oversight (false negative) rate of breast cancers on mammograms is reported as 4%-34% [3]. Suppressing the ribs on chest X-ray images allows clinicians to observe anatomies and lesions overlapped by the ribs [16]. In addition to observing these images by eye, computational techniques assist quantitative diagnosis with little possibility of misdiagnosis. The oversight of lesions that may be cancerous (e.g., lung nodules, breast calcification) may be prevented with automated detection [7, 15]. Interpretation may be quantitatively performed with little variation between observers with automated segmentation [14] and lesions can be classified into malignant or benign [13].

Cardiac diseases are also proving fatal, as mentioned in Section 2.4.1. Cardiac diseases include myocardial infarction, arrhythmia, and heart failure. Computational analysis of cardiac diseases has been widely studied. The electrocardiogram records cardiac activities as electric signals. Arrhythmia has been widely studied for automated diagnosis from electrocardiograms [4, 5]. Imaging techniques are more useful than electrocardiograms for patients' current bodies, such as increasing the image size of the ventricles [19]. The segmentation of heart chambers [18] assists in quantitatively measuring size, shape, and activity. Such information is essential for the diagnosis of various cardiac diseases. For instance, dilated cardiomyopathy [6], a type of heart failure, involves a decrease in the contractile activity of the ventricles, resulting in an enlargement of the cavity sizes of the ventricles. Segmentation of the chambers from MRI volumes [18] or ultrasonographies [17] is useful for detecting dilated cardiomyopathy and quantita-

tively measuring its progress.



# Chapter 3

## Mediastinal lymph node detection

### 3.1 Overview

This chapter addresses mediastinal lymph node detection from CT volumes. CT is widely utilized for imaging around the lungs in clinical practice because of the amount of air contained in the lungs. CT volumes show considerable contrast between air and non-air regions. In clinical practice, detecting mediastinal lymph nodes is essential in lung cancer patients' CT volumes. Mediastinal lymph nodes are small and not readily apparent on CT volumes because there are various tissues with unique intensity ranges in the vicinity of the lymph nodes. It is challenging to model target conditions such as “bloblike structure that is slightly brighter than its surroundings.” It is essential to focus on small intensity gradients around the lymph nodes for detection.

Therefore, in this chapter, a filtering method that works efficiently even among various tissues is proposed and applied for mediastinal lymph node detection. This chapter is based on a paper entitled “Automated mediastinal lymph node detection from CT volumes based on intensity targeted radial structure tensor analysis” published in the *Journal of Medical Imaging* in 2017.

## 3.2 Background

Lung cancer is the leading cause of cancer-related deaths in the United States [90] and China [91]. It is also the leading cause of cancer-related deaths among men worldwide [87]. There are several treatment methods for lung cancer, e.g., surgery, chemotherapy, and radiotherapy. To choose the best treatment method, cancer staging based on the TNM staging system [92] is required. Three factors are focused on in staging: T (tumor), N (lymph nodes), and distant M (metastasis). In the preoperative diagnosis of lung cancer, radiologists check mediastinal lymph nodes on computed tomography (CT) volumes. However, because lymph nodes are small and their silhouette is not clear, they might be overlooked. A computer-Aided Detection (CADe) system for automated lymph node detection is strongly desired. It prevents medical doctors from overlooking and lighten their burden.

There are various approaches for detecting lymph nodes from CT volumes: random forest statistical classifier [125], and local intensity structure analyses based on Hessian matrix [120, 121, 126] or radial structure tensor (RST) [130]. 3D Haar-like features are a three-dimensional feature point detection method that can detect bloblike structures in volumetric images. Barbu et al. [123] introduced 3D Haar-like features for axillary, pelvic, and abdominal lymph nodes. Feulner et al. [132] utilized them for mediastinal lymph node detection. The random forest statistical classifier is an unsupervised machine learning technique that can enhance target objects in image volumes. Cherry et al. [124] utilized random forest statistical classifiers for abdominal lymphadenopathy detection.

Local intensity structure analysis based on the Hessian matrix has been widely used for automated detection and segmentation of organs [163, 164, 166] and lesions [160–162, 165]. The Hessian matrix is computed for each location. It describes the local intensity structure as a blob, line, or sheet around the location and whether it is brighter

or darker than surrounding regions. The bright bloblike structure enhancement filter based on the Hessian matrix (Hessian filter) responds with a high value at the central part of the bloblike regions, brighter than surrounding regions. Feuerstein et al. [101] proposed a mediastinal lymph node detection method using this. Another method proposed by Liu et al. [100] is also based on the Hessian analysis. Random forest [125] and support vector machine (SVM) [159] classifiers were introduced for improvement of performance. Roth et al. [135] introduced deep convolutional neural networks [128] for further improvement.

Another method of detection is through local intensity structure analysis based on RST [130]. Nimura et al. [122] introduced the bright bloblike structure enhancement filter based on RST (RST filter) for detecting the abdominal lymph nodes. Its benefit is that it can enhance the entire region of the target object, in contrast to the Hessian filter, which only enhances the region's central part. The RST filter can capture the lymph node shape more properly than the Hessian filter. The features extracted can be used to determine whether each candidate region is a true positive (TP) or a false positive (FP) using machine learning techniques. However, the RST filters have not performed well on mediastinal lymph node detection. The current RST filter fails when tissues have largely varying intensity distributions close to the target, for instance, in the case of air and contrasting blood vessels.

Lymph nodes on CT volumes typically show the following characteristics:

Characteristics 1) slightly higher intensity than surrounding regions,

Characteristics 2) spherical shape,

Characteristics 3) narrow intensity range similar to soft tissue.

The RST filter is designed to detect the regions having Characteristics 1) and 2). However, mediastinal lymph node detection is a challenging problem in the medical imaging area. Mediastinal lymph nodes are closely surrounded by many structures, such as contrast-enhanced blood vessels or air, as shown in Fig. 3.1. Although several methods

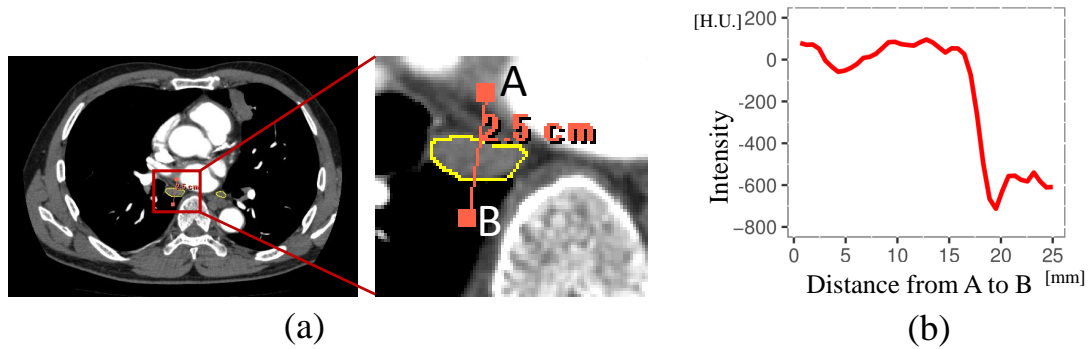


Figure 3.1: Intensity profile of lymph node. (a) Example of axial slice and its magnification of lymph node. Yellow represents lymph nodes. (b) Intensity profile on the line segment A–B shown in (a).

have been proposed for lymph node detection on CT volumes, they fail in detecting such lymph nodes. This chapter proposes a new filter called the ITRST (Intensity Targeted Radial Structure Tensor) filter. The ITRST filter can detect lymph nodes located around the anatomical structures of extremely higher or lower intensities. The ITRST filter's idea is to ignore extremely higher or lower intensity regions in RST computation to meet the requirement of Characteristics 1). This allows us to detect lymph nodes that regions having extremely high or low intensities are neighboring.

This chapter's contribution is summarized as (a) to propose a new lymph node detection filter called the ITRST filter and (b) to evaluate the performances of the ITRST filter by using artificial and clinical CT volumes.

In Section 3.4, we propose the automated mediastinal lymph node detection method based on the ITRST filter and SVM classifier. In Section 3.5, we present two experiments showing the ITRST filter's efficacy. The results are discussed in the following sections.

### 3.3 Conventional local intensity structure analyses

#### 3.3.1 Hessian analysis

As mentioned in Section 3.2, the local intensity structure analysis based on the Hessian matrix [120, 121, 126] has been widely utilized for medical image processing. The Hessian matrix for a point  $\mathbf{x} = [x, y, z]^T$  in the CT volume  $I$  is written by

$$\mathbf{H}(\mathbf{x}) = \begin{bmatrix} \frac{\partial^2}{\partial x^2} I(\mathbf{x}) & \frac{\partial^2}{\partial x \partial y} I(\mathbf{x}) & \frac{\partial^2}{\partial x \partial z} I(\mathbf{x}) \\ \frac{\partial^2}{\partial y \partial x} I(\mathbf{x}) & \frac{\partial^2}{\partial y^2} I(\mathbf{x}) & \frac{\partial^2}{\partial y \partial z} I(\mathbf{x}) \\ \frac{\partial^2}{\partial z \partial x} I(\mathbf{x}) & \frac{\partial^2}{\partial z \partial y} I(\mathbf{x}) & \frac{\partial^2}{\partial z^2} I(\mathbf{x}) \end{bmatrix} \quad (3.1)$$

where  $\frac{\partial^2}{\partial x \partial y} I(\mathbf{x})$  and similar components represent the second derivatives of  $I$  at  $\mathbf{x}$ . The second derivative is given by

$$\frac{\partial^2}{\partial x \partial y} = \frac{\partial^2}{\partial x \partial y} G(\mathbf{x}; \sigma_H) * I(\mathbf{x}) \quad (3.2)$$

where  $G(\mathbf{x}; \sigma_H)$  represents an isotropic 3D Gaussian function with a standard deviation  $\sigma_H$  (Section 3.2 in [121] for more detail). The symbol  $*$  represents convolution.

Eigenvalues of the Hessian matrix are evaluated for filtering. For instance,  $I(\mathbf{x})$  is brighter than the surrounding region if all eigenvalues are negative. The larger the magnitude of the eigenvalue, the larger the gradient. The eigenvalues are utilized to enhance the bright bloblike structure regions that have the condition  $\lambda_1 \simeq \lambda_2 \simeq \lambda_3 \ll 0$  using an evaluation formula. For example, a simple evaluation formula

$$f_{\text{blob}}(\lambda_0, \lambda_1, \lambda_2) = \begin{cases} |\lambda_2| \frac{|\lambda_2|}{|\lambda_0|} & \text{if } \lambda_2, \lambda_1, \lambda_0 < 0, \\ 0 & \text{otherwise,} \end{cases} \quad (3.3)$$

was proposed by Li et al. [120]. Such formulae produce high responses in the bright bloblike regions.

### 3.3.2 RST analysis

The Radial Structure Tensor (RST) is given as the second-order tensor matrix ( $3 \times 3$  matrix). The RST is given by

$$\mathbf{T}(\mathbf{x}) = \sum_i \sum_j \alpha_{i,j} \mathbf{r}_i \mathbf{g}_{i,j}^T, \quad (3.4)$$

where  $\mathbf{x} = (x, y, z)^T$  represents the coordinate of a voxel where the RST is computed,  $\mathbf{r}_i$  represents an  $i$ -th search direction from  $\mathbf{x}$ , and  $\mathbf{g}_{i,j}$  represents a local gradient vector of  $I(\mathbf{x}_{i,j})$ .  $\alpha_{i,j}$  represents the opacity, given by

$$\alpha_{i,j} = \begin{cases} 0 & \text{if } |I(\mathbf{x}) - I(\mathbf{x}_{i,j})| < t_{\min}, \\ \frac{|I(\mathbf{x}) - I(\mathbf{x}_{i,j})|}{|t_{\max} - t_{\min}|} & \text{if } t_{\min} \leq |I(\mathbf{x}) - I(\mathbf{x}_{i,j})| < t_{\max}, \\ 1 & \text{otherwise,} \end{cases} \quad (3.5)$$

where  $i$  is the index of search directions,  $j$  is the index of search steps of each search,  $\mathbf{x}_{i,j}$  is a voxel located in the  $j$ -th search step on the  $i$ -th search direction,  $t_{\min}$  and  $t_{\max}$  ( $t_{\min} < t_{\max}$ ) are parameters for controlling the sensitivity of the gradient. For definition of the search directions  $\mathbf{r}_i$  ( $i = 1, \dots, 42$ ), a pentakis icosidodecahedron (PI) is utilized.  $\mathbf{r}_i$  ( $i = 1, \dots, 42$ ) are defined as direction vectors from the PI's center to the PI's 42 vertices.

When an accumulated opacity  $\beta_i = \sum_j \alpha_{i,j} \simeq 1$  or a search length becomes  $t_{\text{len}}$  or larger, a search for the  $i$ -th search direction is terminated.

Eigenvalues  $\lambda_0, \lambda_1, \lambda_2$  ( $|\lambda_0| \geq |\lambda_1| \geq |\lambda_2|$ ) of  $\mathbf{T}(\mathbf{x}) + \mathbf{T}^T(\mathbf{x})$  represent the magnitude of the gradient directing the corresponding eigenvector around  $\mathbf{x}$ . Those eigenvalues can be evaluated as the same scheme as those of the Hessian matrix for filtering.

## 3.4 ITRST-based lymph node detection method

### 3.4.1 ITRST filter

This chapter introduces a novel bloblike structure enhancement filter called the ITRST filter, a modified version of the RST filter. Before explaining the ITRST filter, we will give a brief overview of the RST filter.

However, suppose some of the radial searches incorporate regions whose intensities are extremely high or low. In that case, huge intensity gradients of some specified directions are summed into the RST  $\mathbf{T}(\mathbf{x})$ , according to Eq. (3.4). The eigenvalues calculated in such regions may become  $\lambda_0 \ll \lambda_1 \leq \lambda_2 \leq 0$  or  $\lambda_1 \leq \lambda_2 \leq 0 \ll \lambda_0$ , and the responses of an evaluation formula such as Eq. (3.3) become low.

To prevent the effect of the huge intensity gap explained above, we propose the ITRST filter. Schematic illustration showing the difference between the RST and the ITRST filters is summarized in Fig. 3.2. The ITRST filter introduces the target region's prior knowledge to prevent summing huge intensity gradients into the ITRST. Intensity gradients at higher or lower intensity regions than the thresholds are not summed into the ITRST. The ITRST is defined by modifying Eq. (3.4) as

$$\mathbf{T}'(\mathbf{x}) = \sum_i \sum_j \alpha_{i,j} \gamma_{i,j} \mathbf{r}_i \mathbf{g}_{i,j}^T \quad (3.6)$$

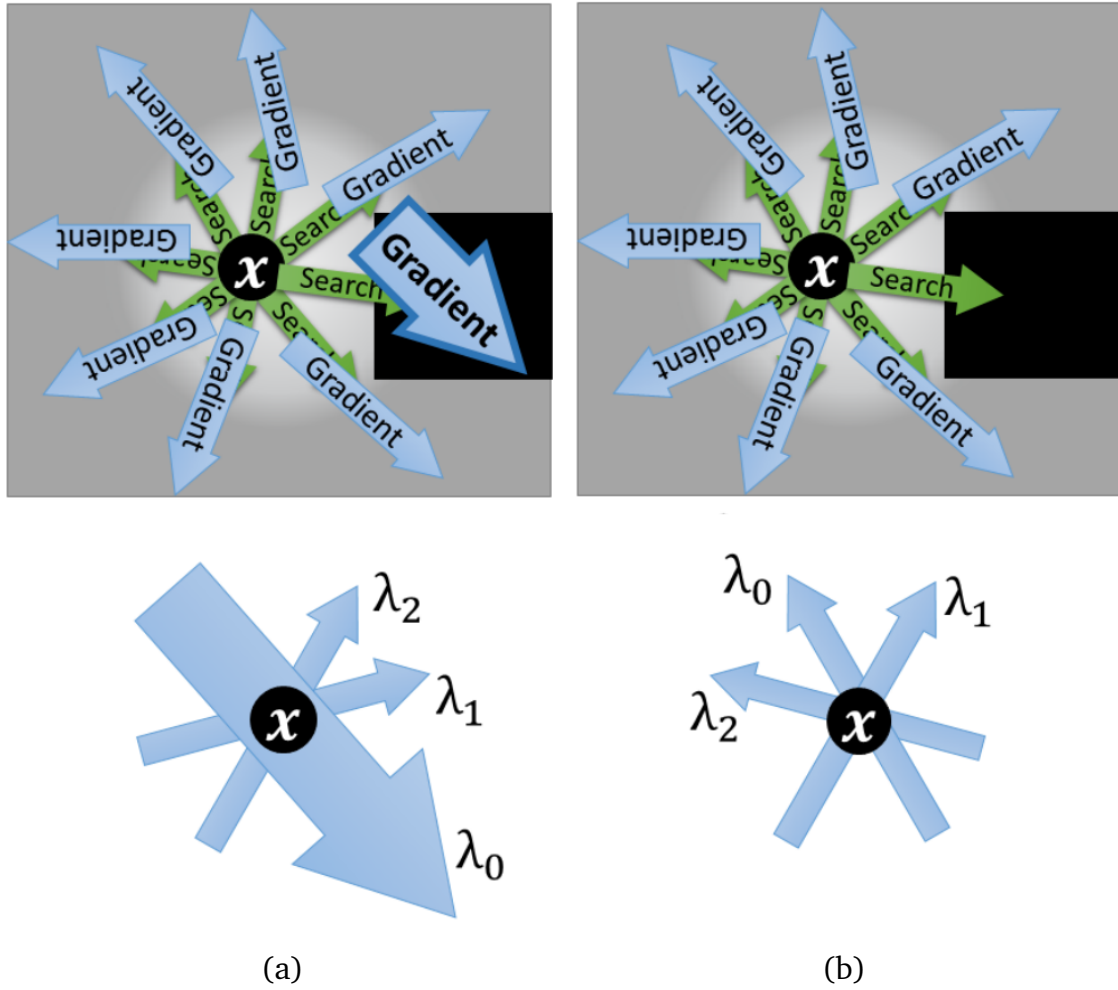


Figure 3.2: Schematic illustration showing differences between (a) RST and (b) ITRST filters. Point  $x$  is in sphere, and sphere is touching region with very low intensities. Top row represents intensity gradients that are summed into RST and ITRST, respectively. Bottom row represents magnitudes of eigenvalues  $\lambda_0, \lambda_1, \lambda_2$  ( $|\lambda_0| \geq |\lambda_1| \geq |\lambda_2|$ ) with corresponding eigenvectors of RST and ITRST, respectively.

where  $\gamma_{i,j}$  is a function that classifies whether all points utilized for computing  $g_{i,j}$  have the intensity within a predetermined range or not, which is defined as

$$\gamma_{i,j} = \begin{cases} 1 & \text{if } t_{\text{dark}} \leq I(\mathbf{x}') \leq t_{\text{bright}} \text{ for } \forall \mathbf{x}' \in \mathcal{N}(i, j) \\ 0 & \text{otherwise,} \end{cases} \quad (3.7)$$

where  $\mathcal{N}(i, j)$  is a set of 6-neighborhood voxels around  $\mathbf{x}_{i,j}$ . In Eq. (3.7),  $t_{\text{dark}}$  and  $t_{\text{bright}}$  are upper and lower limits of target intensity range, respectively. The parameters  $t_{\text{dark}}$  and  $t_{\text{bright}}$  affect the enhancement results as follows. If we lower  $t_{\text{dark}}$ , this causes FPs of lymph nodes located at neighbors of air regions. If we set  $t_{\text{bright}}$  higher, this setting produces false negatives (FNs) of lymph nodes located at neighbors of contrast-enhanced blood vessels (intensities of 150 – 300 H.U.) are produced. Choosing higher  $t_{\text{dark}}$  or lower  $t_{\text{bright}}$  makes the filter responses lower, because it reduces the intensity gradients summed into the ITRST. When an accumulated opacity  $\beta'_i = \max\left(\sum_j \alpha_{i,j}, \gamma_{i,j}\right) \simeq 1$  or a search length becomes  $t_{\text{len}}$  or larger, a search for the  $i$ -th search direction is terminated. Eigenvalues of  $\mathbf{T}'(\mathbf{x}) + \mathbf{T}'^T(\mathbf{x})$ ,  $\lambda'_0, \lambda'_1, \lambda'_2$  ( $|\lambda'_0| \geq |\lambda'_1| \geq |\lambda'_2|$ ) can be utilized in the same manner as those of the RST filter.

### 3.4.2 Mediastinal lymph node detection

#### Overview

This section explains a mediastinal lymph node detection method from CT volumes based on the ITRST filter. In this method, we assume that the input of the method is a chest CT volume. The output is mediastinal lymph node detection results. Detection targets are the mediastinal lymph nodes having specified least short axis or above. This is because enlarged lymph nodes have a high possibility to be metastasized. The entire process consists of (1) preprocessing, (2) obtaining candidate regions by thresholding against the responses of the ITRST filter, and (3) FP reduction using a machine-learning.

The input volume  $I$  is a chest CT volume. The ground-truth binary volume  $I_g$  of mediastinal lymph nodes is required if  $I$  is utilized for training only. The output is a binary volume  $I_{\text{out}}$ , which has lymph node regions denoted by the value 1. We describe the size of each lymph node using Principal Components Analysis. We focus on detecting lymph nodes above a specified size, defined by a short axis length of at least  $r_{\text{target}}$  [mm].

## Preprocessing

First, we interpolate an input volume to generate an isotropic resolution volume. We apply the cubic interpolation on  $I$  to obtain a volume with isotropic resolution  $w_{\text{reso}}$  [mm]  $\times w_{\text{reso}}$  [mm]  $\times w_{\text{reso}}$  [mm] per voxel [89]. Furthermore, we apply a Gaussian smoothing filter with standard deviation  $\sigma_{\text{smooth}}$  [mm] to reduce noise and make local gradients more stable. We denote the preprocessed input volume as  $I'$ .

## Target region of detection

We restrict the target region for lymph node detection to inside the mediastinal region. We define the mediastinal region simply as the region between the right and left lungs. A lung region  $A_{\text{lung}}$  is segmented by some automatic segmentation method. We use a lung segmentation method similar to Hu et al.[136].

Firstly, we obtain air regions  $A_{\text{air}}$  in  $I'$  as regions having lower intensities than a given threshold  $t_{\text{air}}$  and not touching to the boundary of the input CT volume. Then, we select the first and second largest connected components from the air regions detected. If the second largest component of the air regions is less than 20% of the largest one, we choose the largest component of the air regions as  $A_{\text{lung}}$ . Finally, the mediastinum region  $A_{\text{media}}$  is obtained by  $A_{\text{lung}}$  using **Algorithm 1**. The function  $\max(a)$  represents the maximum value of  $a$  in this algorithm.

We assume that the  $x$ -axis of the input volume  $I$  corresponds with the right-to-left direction of the body, the  $y$ -axis corresponds with the front-to-back direction, and  $z$ -axis corresponds with the head-to-foot direction. We scan the lung region  $A_{\text{lung}}$  from each pair of  $(y, z)$  toward the right-to-left direction (along the  $x$ -axis). For each scan, we check whether no fewer than two components exist in the scan line. This means that there are right and left lung regions in the scan line. If no fewer than two components exist, we fill the gap between each component by the value 1.

**Algorithm 1** Segmentation of Mediastinum Region  $A_{\text{media}}$ 


---

Input: lung region  $A_{\text{lung}}$   
**for**  $z = 0$  to  $\max(z)$  **do**  
  **for**  $y = 0$  to  $\max(y)$  **do**  
     $a_1 = 0$   
    **for**  $x = 0$  to  $\max(x) - 1$  **do**  
      **if**  $A_{\text{lung}}(x, y, z) = 1 \cap A_{\text{lung}}(x + 1, y, z) = 0$  **then**  
         $a_1 \leftarrow a_1 + 1$   
      **end if**  
    **end for**  
    **if**  $a_1 \geq 2$  **then**  
       $a_2 = 0$   
      **for**  $x = 0$  to  $\max(x) - 1$  **do**  
        **if**  $1 \leq a_2 < a_1 \cap A_{\text{lung}}(x + 1, y, z) = 0$  **then**  
           $A_{\text{media}}(x, y, z) \leftarrow 1$   
        **end if**  
        **if**  $A_{\text{lung}}(x, y, z) = 1 \cap A_{\text{lung}}(x + 1, y, z) = 0$  **then**  
           $a_2 \leftarrow a_2 + 1$   
        **end if**  
      **end for**  
    **end if**  
  **end for**  
**end for**  
Output: mediastinum region  $A_{\text{media}}$

---

**Initial lymph node detection using ITRST filter**

We obtain the candidate regions using the ITRST filter. Firstly we apply the ITRST filter with the evaluation formula (3.3) to  $I'$ . Since each point of  $I'$  has one response, we obtain the volume of filter response  $F$ . Because responses of the ITRST filter sometimes become zero in the bloblike regions as like an individual hole, we apply a median filter of  $w_{\text{hole}} \times w_{\text{hole}} \times w_{\text{hole}}$  [voxels] to  $F$  for normalizing such points. Then, we perform thresholding onto the result of the median filter  $F'$  as

$$F'_{\text{blob}}(\mathbf{x}) \geq t_{\text{blob}} \quad (3.8)$$

with the threshold value  $t_{\text{blob}}$ . Regions of connected components whose volume is less than that of the sphere with radius  $t_{\text{small}}$  (mm) and ones that are not touching the mediastinum region  $A_{\text{media}}$  are eliminated. The remaining are denoted as candidate regions.

### FP reduction

Candidate regions generated by the ITRST filter contain many FP regions. The SVM classifier is utilized to classify each candidate region into a TP or an FP.

$(10 + 7|\mathcal{D}|)$ -dimensional features are utilized for each candidate region, as shown in Table 3.1.  $\mathcal{D}$  is the permutation of radii utilized for computation of features related to the intensity. The number of elements of  $\mathcal{D}$  is  $|\mathcal{D}|$ , index of  $\mathcal{D}$  is  $p$  ( $1 \leq p \leq |\mathcal{D}|$ ), and one of its elements is written as  $d \in \mathcal{D}$ . When  $d > 0$  mm, the target region for calculating the intensity features is obtained by dilation of the candidate region. The dilation is performed using a structural element of a sphere whose radius is  $d$  mm. The target region represents the candidate region's neighbor, and larger values of  $d$  bring the target region thicker. When  $d = 0$  mm, the target region is the same as the candidate region. Features are computed for both the training step and the testing step and utilized as follows.

- *Training step*

Feature vectors obtained from candidate regions of all volumes in the training dataset are used for training of the SVM [159]. The set of lymph node regions whose short axis is at least  $r_{\text{target}}w_{\text{train}}$  mm in the ground truth  $I_g$  is written as  $\mathcal{G}$ .  $r_{\text{target}}$  is a parameter representing the minimum length of the target lymph nodes' short axis.  $w_{\text{train}}$  ( $0 < w_{\text{train}} < 1$ ) is the parameter for setting the smallest size of a lymph node that is utilized for training. If the center of a candidate region is in one of the lymph node regions of  $\mathcal{G}$ , its feature vector is utilized as a positive

sample. If the center of a candidate region is outside the lymph node regions, its feature vector is utilized as a negative sample.

- *Testing step*

A candidate region extracted from a test volume is classified into TP or FP with its feature vector by using an SVM trained as above. If a candidate region is predicted as a TP, the values of the output binary volume  $I_{\text{out}}$  are set to 1 in the candidate region.

Table 3.1: Features for FP reduction step.

Group	Symbol	Definition
Geometry	$u_1$	Volume ( $\text{mm}^3$ )
	$u_2$	Surface area ( $\text{mm}^2$ )
	$u_3$	Sphericity
	$u_4$	Maximum length from contour (mm)
	$u_5$	Length of long axis (mm)
	$u_6$	Length of short axis (mm)
Location	$u_7$	$x$ - coordinate
	$u_8$	$y$ - coordinate
	$u_9$	$z$ - coordinate
Intensity	$u_{10+7(p-1)}$	Average
	$u_{11+7(p-1)}$	Variance
	$u_{12+7(p-1)}$	Median
	$u_{13+7(p-1)}$	Maximum of $I$ in the target region. See section 3.4.2 for the detail.
	$u_{14+7(p-1)}$	Minimum
	$u_{15+7(p-1)}$	Skewness
	$u_{16+7(p-1)}$	Kurtosis

## 3.5 Experiements

### 3.5.1 ITRST filter

#### Synthetic data

A synthetic volume is utilized for the evaluation of the ITRST filter. This volume includes seven objects imitating lymph nodes, three objects imitating contrast-enhanced blood vessels, and three objects imitating air regions. Figures 3.3 (a) and (b) show the blueprint and one slice of the artificially-generated volume containing the synthetic objects, respectively. This volume contains one isolated sphere, three spheres overlapping with 300 H.U. square poles, and three spheres overlapping with -1,000 H.U. square poles. The background of the volume is 0 H.U. The spheres whose diameter is 15 mm are drawn as the uniform of 50 H.U. Gaussian smoothing of  $\sigma = 1.0$  mm is applied to make the spheres similar to lymph nodes of real CT volumes. After that, the square poles whose thickness is 15 mm and length is 50 mm are drawn.

#### Filter responses

We apply the ITRST, the RST, and the Hessian filters to the artificially-generated volume explained above. Firstly, we examine the filter responses. In this experiment, we obtain the eigenvalue profile on the two spheres shown in Fig. 3.3 (b). The line A–B on Fig. 3.3 (b) crosses one of the spheres overlapping with a dark region. The line C–D is on one of the spheres overlapping with a bright region.

Parameters used in the experiments are shown in Table 3.4 (a). We set  $t_{\text{bright}} = 100$  H.U. and  $t_{\text{dark}} = -100$  H.U. since the spheres have comparability with lymph nodes ranging from -100 H.U. to 100 H.U. We also set  $t_{\text{len}} = 15$  mm as the upper limit of the radius of lymph nodes to be detected in real CT volumes.

Table 3.2: Specification of CT volumes used in experiments of mediastinal lymph node detection.

Item	Spec
Number of volumes	47
Dimension	3
Phase	Arterial
Device	Aquilion 64, Toshiba
Reconstruction function	FC11
Size	$512 \times 512 \times (338\text{--}463)$ voxels
Resolution	$(0.625\text{--}0.782) \times (0.625\text{--}0.782) \times (0.799\text{--}0.801)$ mm <sup>3</sup>

### 3.5.2 Mediastinal lymph node detection

Table 3.3: Number of lymph nodes categorized by short axes.

Size category	Number of lymph nodes
[10 mm, $\infty$ )	57
[7.5 mm, 10 mm)	62
[5 mm, 7.5 mm)	145
[3 mm, 5 mm)	284
Total	548

#### Materials

Forty-seven chest CT volumes are prepared for the experiments of mediastinal lymph node detection. These volumes are authorized by the ethics committee of Nagoya University Hospital. The specifications of the volumes are shown in Table 3.2. We evaluate the performance of lymph nodes for a range of minimum sizes: the short axis is at least  $r_{\text{target}} \in \{10, 7.5, 5 \text{ mm}\}$ . Ground-truth data is a set of mediastinal lymph node labels. Two technical researchers who have enough knowledge of lymph nodes traced lymph

node candidate regions on the CT volumes manually. Then, an expert radiologist confirmed these traced data, including missing lymph nodes on CT slices. Table 3.3 shows the number of lymph nodes of each size category.

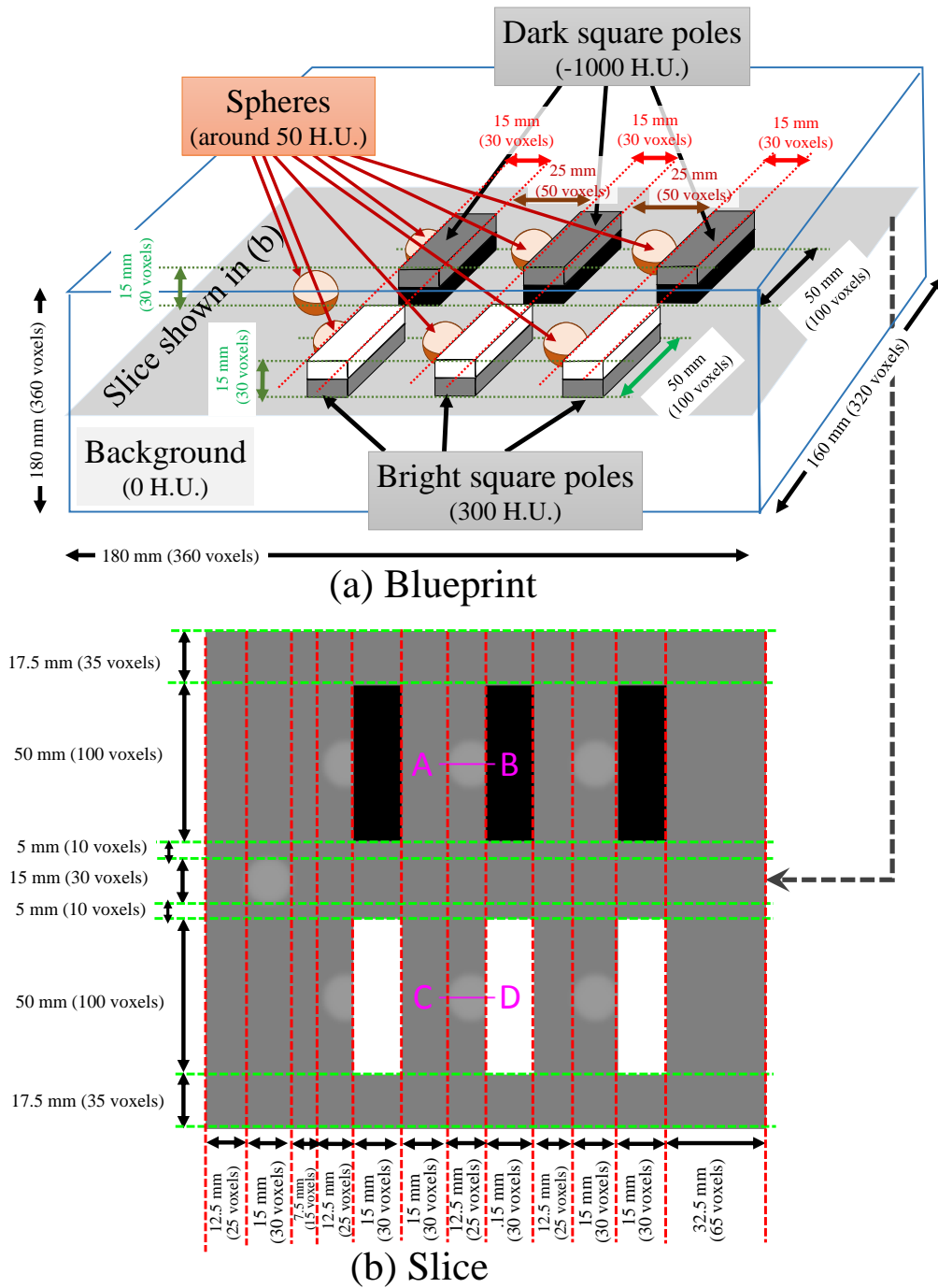


Figure 3.3: Synthetic examples of solid objects. (a) Blueprint of artificially-generated volume. Slice contains centers of all spheres. (b) Slice containing one isolated sphere and six spheres touching bright (300 H.U.) or dark (-1000 H.U.) square poles.

Table 3.4: Constant parameter values. (a) ITRST filter. (b) Mediastinal lymph node detection: Initial detection evaluation. (c) Mediastinal lymph node detection: Overall detection performance evaluation. Note that  $r_{\text{target}}$ ,  $t_{\text{blob}}$ , and  $w_{\text{F}}$  are not shown here since they are varied for evaluating the performances of different conditions.

Symbol	Value	Definition
<b>(a) ITRST filter</b>		
$t_{\text{bright}}$	100 H.U.	Upper limit of intensity target range of ITRST filter
$t_{\text{dark}}$	-100 H.U.	Lower limit of intensity target range of ITRST filter
$t_{\text{len}}$	15 mm.	Maximum search length of ITRST filter
<b>(b) Mediastinal lymph node detection: Initial detection evaluation</b>		
$t_{\text{bright}}$	100 H.U.	Upper limit of intensity target range of ITRST filter
$t_{\text{dark}}$	-100 H.U.	Lower limit of intensity target range of ITRST filter
$t_{\text{len}}$	15 mm.	Maximum search length of ITRST filter
$t_{\text{air}}$	-200 H.U.	Threshold for dividing air and other regions
$w_{\text{reso}}$	0.625 mm	Isotropic resolution that input volume is interpolated
$\sigma_{\text{smooth}}$	1 mm	Standard deviation of Gaussian smoothing filter
$w_{\text{hole}}$	3 voxels	Size of median filter applied for output of ITRST filter
<b>(c) Mediastinal lymph node detection: Overall detection performance evaluation</b>		
$w_{\text{train}}$	0.5	Tolerance of using feature vectors extracted from candidate regions of smaller lymph nodes than $r_{\text{target}}$ for training SVM
$\mathcal{D}$	{0, 1, 2} mm	Width of regions for computing feature values regarding intensity

### Initial detection performances

We compute FROC curves of initial detection results by changing the parameter  $t_{\text{blob}}$  for comparing the ITRST, the RST, and the Hessian filters. The filter output is binarized in different thresholds ( $t_{\text{blob}} = 20, 40, 80,$  and  $160$  for the ITRST filter,  $t_{\text{blob}} = 20, 40, 80,$  and  $160$  for the RST filter, and  $t_{\text{blob}} = 2000, 4000, 8000,$  and  $16000$  for the Hessian filter), as explained in Section 3.4.2.

Each point on FROC curves represents the averages of the detection rate and the number of FPs/volume among all volumes. The corresponding error bars represent the standard deviation of the detection rate. Our detection targets are mediastinal lymph nodes whose short axes are at least  $r_{\text{target}}$  [mm]. Each mediastinal lymph node is classified and counted as a TP or an FN. If at least one region produced by the filter is overlapping with a mediastinal lymph node of the detection target, the lymph node is counted as a TP. The detection rate of each volume is defined as

$$(\text{Detection rate of each volume}) = \frac{(\text{Number of TPs})}{(\text{Number of detection targets})}.$$

The number of FPs in each volume is the count of regions produced by the filter that does not overlap with any lymph nodes or lung cancers.

The FROC curves are drawn for each value (5, 7.5, 10 mm) of the least short axis parameter  $r_{\text{target}}$ . Parameters of  $t_{\text{bright}}, t_{\text{dark}},$  and  $t_{\text{len}}$  are the same as the experiment of Section 3.5.1. Other parameters are set empirically (Table 3.4 (b)). Air region segmentation threshold  $t_{\text{air}}$  is set as -200 H.U. This threshold is set as enough lower than lymph nodes or surrounding soft tissues, which have around -100 H.U. or above. Isotropic resolution parameter  $w_{\text{reso}}$  is set as 0.625 mm. This is equals to the smallest pixel size of axial slices of the CT volumes (Table 3.2). Standard deviation of Gaussian smoothing filter  $\sigma_{\text{smooth}}$  is set as 1 mm. This setting is good for reducing noise on chest CT volumes

without severely blurring edges. The parameter  $w_{\text{hole}}$ , the size of the median filter applied for the output of the ITRST filter, is set as three voxels. This is the smallest size of the median filter.

### Overall detection performances

We compute the FROC curves as the overall performances. This performance includes FP reduction by SVM. An FROC curve is obtained by changing the weighting parameter  $w_{\text{F}}$  of negative samples for the SVM classifier [159] utilized in the FP reduction step (explained in Section 3.4.2). Leave-one-out cross-validation is conducted to evaluate the performance of FP reduction for each volume. The SVM classifier is tested by the data not used in the training process.

We also conduct the statistical test (Fisher’s exact test) of the detection rate obtained by the ITRST filter and the others. For a fair comparison of detection rates between the filters, we draw the FROC curve with various values of  $w_{\text{F}}$ , and estimate the detection rate at the point of 10.0 FPs/volume on the FROC curve.

The threshold for the filter output is chosen as  $t_{\text{blob}} = 20$  for the ITRST and the RST filters, and  $t_{\text{blob}} = 2000$  for the Hessian filter, since these settings of  $t_{\text{blob}}$  gave the highest initial detection rate with each filter. For computing the FROC curves, the weighting parameter  $w_{\text{F}}$  is changed as 0.025, 0.05, 0.075, 0.10, 0.125, 0.15, 0.20, 0.25, 0.30, 0.40, and 0.50. Other parameters utilized for the FP reduction step are set empirically (Table 3.4 (c)). The parameter  $w_{\text{train}}$  for the tolerance of using feature vectors extracted from candidate regions of smaller lymph nodes than the  $r_{\text{target}}$  is set as 0.5, for preventing FNs of lymph nodes whose short axis is almost the same as  $r_{\text{target}}$ . Permutation  $\mathcal{D}$  representing the width of regions for computing feature values regarding intensity is set as  $\{0, 1, 2\}$  for focusing on each candidate region’s inside and neighboring regions. The LIBSVM 3.17 [158] library is utilized as an SVM implementation.

## 3.6 Results

### 3.6.1 ITRST filter

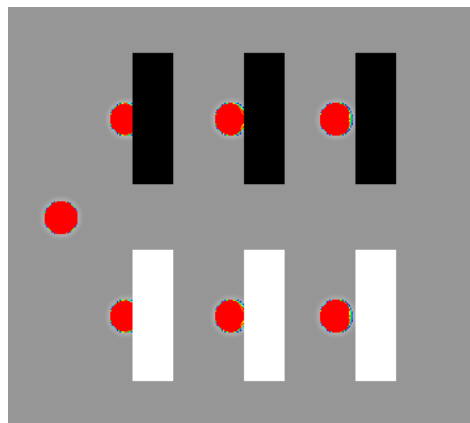
The responses of the ITRST, RST, and Hessian filters for the synthetic volume are shown in Figs. 3.4 (a), (b), and (c), respectively. The responses were higher in most sphere regions than those of the RST and the Hessian filters, despite the overlapping of square poles.

The eigenvalue profiles obtained by the ITRST, RST, and Hessian filters are shown in Fig. 3.5 (a), (b), and (c), respectively. Using the ITRST filter, all eigenvalues were negative. Their magnitudes are not very different from each other in the whole part of both spheres. Using the RST filter,  $\lambda_1$  became far smaller or larger than other eigenvalues, in the spheres touching to the bright and dark square poles, respectively. Eigenvalues of the Hessian filter also become positive in the parts near the square poles.

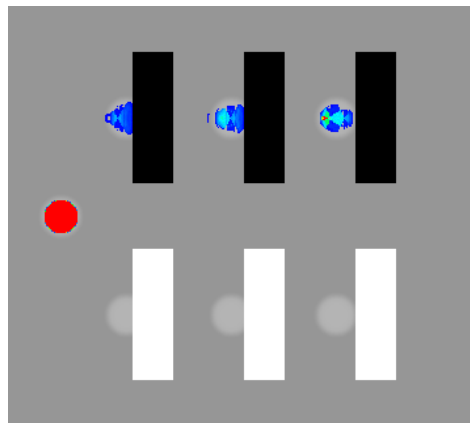
### 3.6.2 Mediastinal lymph node detection

#### Initial detection

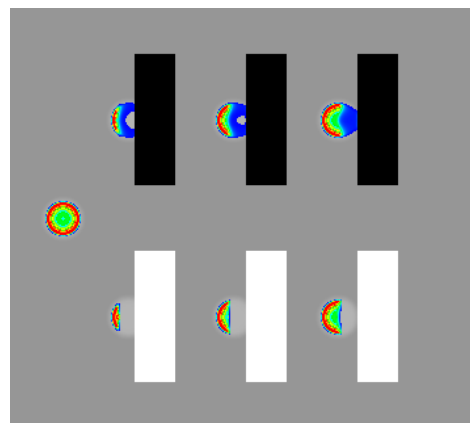
The FROC curves of initial detection are shown in Fig. 3.6. As shown in Table 3.5, a higher detection rate was achieved by the proposed method (ITRST filter) than by the RST filter. For instance, when  $r_{\text{target}} = 10$  mm and  $t_{\text{blob}} = 20$ , 97.1% of lymph nodes were detected with 692.1 FPs/volume by the proposed method (ITRST filter). Using the RST ( $t_{\text{blob}} = 20$ ) or the Hessian filters ( $t_{\text{blob}} = 2000$ ), 75.4% or 91.1% were detected with 377.8 or 683.2 FPs/volume, respectively. Examples of the detection results are shown in Fig. 3.8.



(a) ITRST filter

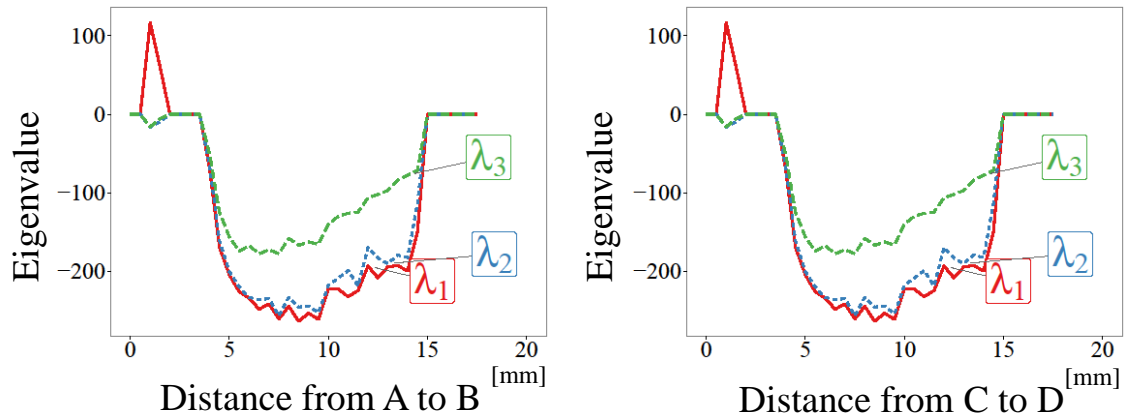


(b) RST filter

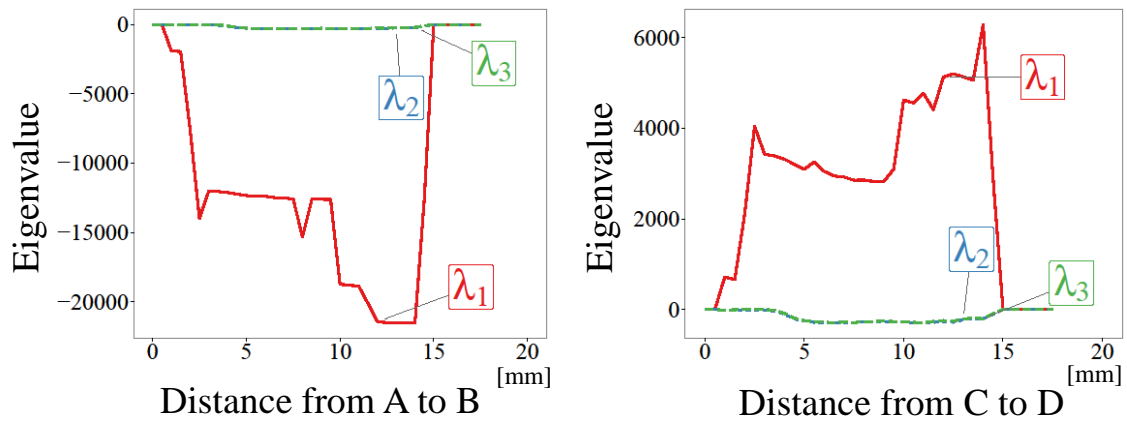


(c) Hessian filter

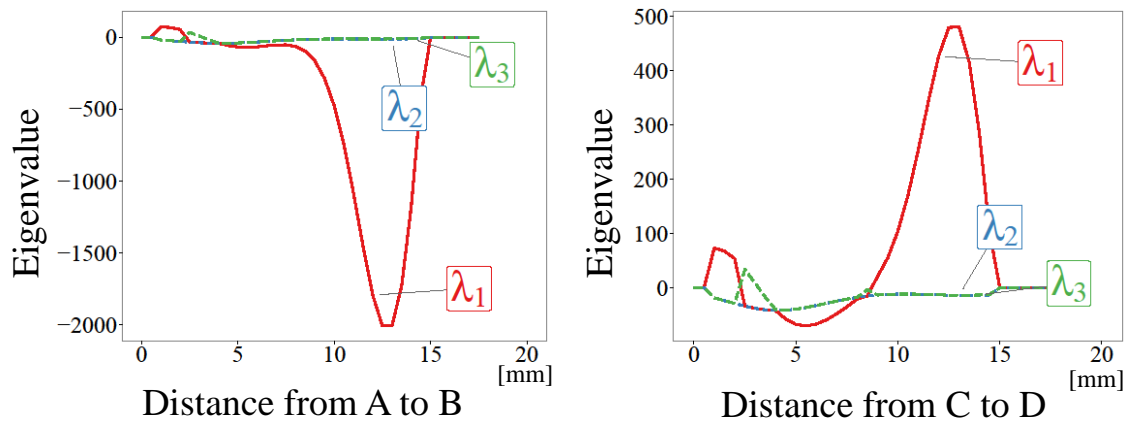
Figure 3.4: Responses for synthetic volume. (a) ITRST filter. (b) RST filter. (c) Hessian filter. Color scheme is same as (a). Blue represents low response (around 1), yellow represents medium response (around 125), and red represents high response (around 250).



(a) ITRST filter



(b) RST filter



(c) Hessian filter

Figure 3.5: Eigenvalue profiles on lines A–B and C–D shown in Fig. 3.3 (b). (a) ITRST filter. (b) RST filter. (c) Hessian filter.

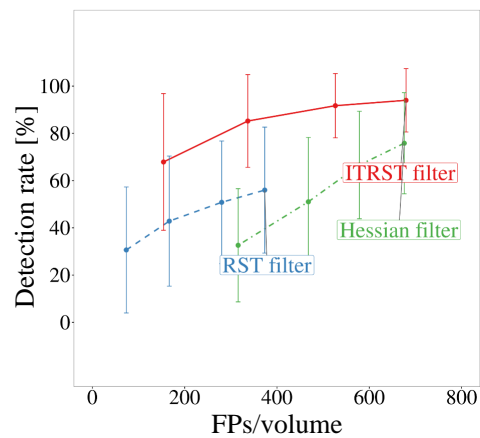
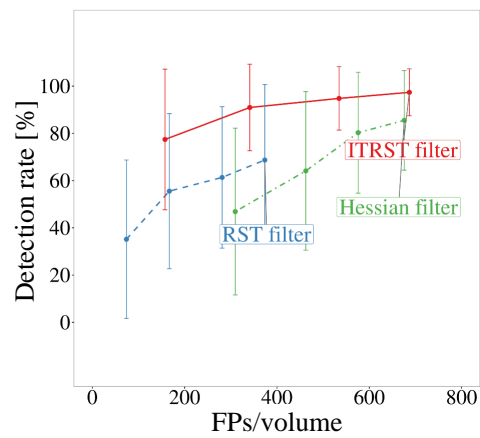
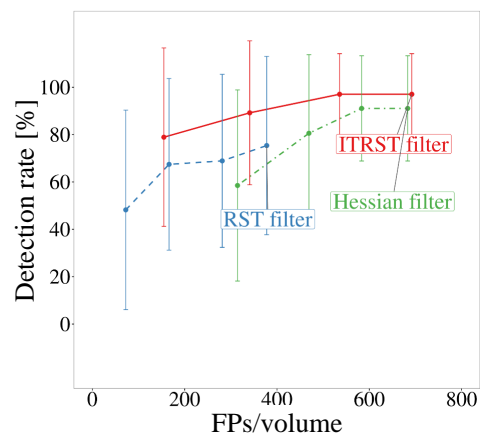
(a)  $r_{\text{target}} = 5$  mm(b)  $r_{\text{target}} = 7.5$  mm(c)  $r_{\text{target}} = 10$  mm

Figure 3.6: FROC curves obtained after initial detection ( $t_{\text{blob}}$  for 20.0, 40.0, 80.0, and 160.0 for ITRST and RST filters, and  $t_{\text{blob}}$  for 2000, 4000, 8000, and 16000 for Hessian filter). (a)  $r_{\text{target}} = 5$  mm. (b)  $r_{\text{target}} = 7.5$  mm. (c)  $r_{\text{target}} = 10$  mm.

Table 3.5: Comparison of lymph node detection performances. Note that symbol \* represents performance shown in publications. Their experiments were performed using different datasets or criteria from ours.

method	Least short axis [mm]	Initial detection		After FP reduction	
		Detection Rate [%]	FPs/volume	Detection Rate [%]	FPs/volume
Proposed method	5	94.0±13.4	679.6±83.6	68.4±25.7	10.0±5.2
RST filter	5	56.0±26.7	373.5±80.7	44.0±24.6	6.6±4.2
Hessian filter	5	75.8±21.4	675.8±117.0	54.9±25.6	11.9±5.3
Proposed method	7.5	97.4±9.9	686.8±84.3	72.8±29.6	10.1±5.3
RST filter	7.5	68.7±32.0	373.7±80.4	55.8±33.4	6.6±4.3
Hessian filter	7.5	85.5±21.1	675.6±118.1	68.6±33.5	11.7±5.3
Proposed method	10	97.1±17.1	692.1±82.6	84.2±31.0	9.1±5.1
RST filter	10	75.4±37.6	377.8±77.2	63.9±41.4	6.3±4.2
Hessian filter	10	91.1±22.2	683.2±121.7	78.2±35.3	11.1±5.1
* Roth et al.[135]	10	-	-	84	6
* Liu et al.[131]	10	-	-	80	8
* Feulner et al.[132]	10	-	-	60.9	6.1

### Overall performances

Table 3.5 and Fig. 3.7 show the overall performances calculated from the detection method's output, with parameters  $t_{\text{blob}} = 20$  ( $t_{\text{blob}} = 2000$  for Hessian filters) and  $w_F = 0.075$ . For example, when  $r_{\text{target}} = 10$  mm, 84.2% of lymph nodes were detected with 9.1 FPs/volume by the proposed method (the ITRST filter). Table 3.6 displays the results of Fisher's exact test at 10.0 FPs/volume. Performances of the proposed method were not always significantly better. It was showed that detection rates of ITRST and RST filters were significantly different ( $p < 0.05$ ) with all settings (5, 7.5, 10 mm) of the least short axis. On the other hand, the ITRST and the Hessian filters' detection rates were significantly different when the least short axis was 5 mm.

Table 3.6: Fisher's exact test among detection rate at 10.0 FPs/volume.

Least short axis [mm]	Detection rate [%]			$p$ -value	
	ITRST	RST	Hessian	ITRST-RST	ITRST-Hessian
5	68.3	46.4	53.0	0.003	0.043
7.5	72.5	57.5	65.6	0.037	0.357
10	85.1	66.4	76.8	0.003	0.207

## 3.7 Discussion

### 3.7.1 ITRST filter

The ITRST filter responses were higher in most of the sphere regions than those of the RST filter, even if the square poles were overlapping, as shown in Fig. 3.4. It suppressed the negative effect of the regions with much higher or lower intensity than the detection target. The Hessian filter responded positive values only on some parts of the spheres.

The magnitude of  $\lambda_1$  computed from the ITRST filter was similar to  $\lambda_2$  and  $\lambda_3$ , and it was negative on almost all of A-B or C-D, as shown in Fig. 3.5 (a). Huge intensity

gradients were not summed into the ITRST, and the eigenvalues followed the condition of the bright bloblike structure. In contrast, as shown in Fig. 3.5 (b), the magnitude of  $\lambda_1$  computed from the RST filter was far larger than  $\lambda_2$  and  $\lambda_3$  in the sphere. This is because huge intensity gradients directed from the sphere to the square pole were accumulated into the RST. Figure 3.5 (c) shows the magnitude of  $\lambda_1$  computed from the Hessian filter, which becomes large near the square poles of in the Hessian filter. The eigenvalues did not follow the condition of the bright bloblike structure ( $\lambda_1 \simeq \lambda_2 \simeq \lambda_3 \ll 0$ ) in the part having large magnitude of  $\lambda_1$ , and the responses became low according to Eq. (3.3).

By comparing the FROC curves of initial detection shown in Fig. 3.6, the ITRST filter had a higher detection rate for large and small lymph nodes than the RST filter. After FP reduction of the proposed method (ITRST filter), results were also better than those of the RST filter. The ITRST filter is more useful than the RST filter for mediastinal lymph node detection.

### 3.7.2 Mediastinal lymph node detection

#### Efficacy of ITRST filter

The lymph node shown in Fig. 3.8 (a) was detected correctly by the proposed method (ITRST filter) and the Hessian filter. In contrast, the RST filter was not able to detect it. This was likely due to contrast-enhanced blood vessels and the air region adjacent to the lymph node. In contrast to the RST filter, the ITRST filter reduced the large intensity gradients' impact around the lymph node. The eigenvalues still followed the condition of the bright bloblike structure. Extremely high- or low-intensity regions did not surround this lymph node. Some intensity gradients derived from soft tissue could still be utilized for describing the bright bloblike structure.

The lymph node shown in Fig. 3.8 (b) was detected initially by all methods. The

candidate region obtained by the RST filter was poorly segmented because of the negative effect of the contrast-enhanced blood vessels and the air. It was removed by SVM. However, the candidate region obtained by the ITRST filter covered most of the lymph node region, and it was classified as a lymph node. The ITRST filter prevented the negative effect of the surrounding regions and contributed to accurate classification. Although the candidate region obtained by the Hessian filter was a little smaller than the one of the ITRST filter, it was also properly classified.

### **Still produced FNs**

Some lymph nodes were still missed by the ITRST filter, as shown in the FROC curves in Fig. 3.6. This is because they tend to be sandwiched by extremely high or low intensity regions. For instance, the lymph node shown in Fig. 3.8 (c) could not be detected by the ITRST or the RST filters. It was sandwiched by the contrast-enhanced blood vessels, and the air region, and very little amount of soft tissue was touching the lymph node. Most gradient vectors around it were not summed into the ITRST, so the magnitude of eigenvectors did not follow the condition of the bright bloblike structure. In contrast to the ITRST or the RST filters, the Hessian filter does not strongly suffer from intensity differences between lymph nodes and neighboring regions. The small candidate region detected by the Hessian filter was finally classified into lymph node class after the FP reduction process. Future work is to improve the ITRST filter that can segment lymph nodes surrounded by extremely high or low intensity regions.

The ITRST filter initially detected the lymph node shown in Fig. 3.8 (d). However, the SVM classifier removed it. To prevent generating such kind of FNs, we will improve the classification accuracy by introducing deep learning techniques as future work. Note that the candidate region of the ITRST filter was classified correctly as a lymph node with  $w_F = 0.025$ .

### **Promise for application to segmentation**

As shown in Fig. 3.8 (e), some lymph nodes are detected by all filters (the ITRST, the RST, and the Hessian). However, the ITRST filter produced more proper segmentation results of lymph nodes than other filters. In the future, the ITRST filter can be improved for application to the segmentation of lymph nodes, not only for detection. This will assist radiologists in measuring the size and shape of each lymph node.

### **3.7.3 Lung area segmentation**

We have extracted mediastinum regions from CT volumes by extracting lung regions. There is some possibility to fail in lung region segmentation in the pathological lung having lung cancer, as shown in Fig. 3.9. However, that does not affect the subsequent processes since lung segmentation is only for obtaining the mediastinum region sandwiched by the left and right lungs. The lung cancer region is merged into the target region.

## **3.8 Conclusions**

This chapter proposed a novel mediastinal lymph node method based on the intensity targeted radial structure tensor (ITRST) filter. The conventional radial structure tensor (RST) filter cannot detect some lymph nodes due to the effects of neighboring lymph node regions, which have extremely high or low intensities. We proposed the ITRST filter by modifying the RST filter to prevent such negative effects by introducing knowledge about the detection target's intensity range. This allows us to exclude neighboring regions for computing the filter response and increase the lymph node detection rate.

We evaluated the ITRST filter's efficacy by applying it to both an artificially generated volume and chest CT volumes. In the synthetic data experiment, the ITRST filter

produced high responses of detection in the spheres neighboring bright or dark square poles. In contrast, the RST filter responses were very low. These results show that the ITRST filter can prevent the negative effect caused by neighboring regions in contrast to the RST filter, which severely suffers from these types of regions.

Furthermore, experimentation with real clinical images for mediastinal lymph node detection showed that the ITRST filter outperformed the RST filter. This is because most of the mediastinal lymph nodes adjacent to air or contrast-enhanced blood vessels in the chest CT volumes can be detected using the ITRST filter. The detection performance after FP reduction was also better than the RST filter. The proposed ITRST filter could potentially detect other organs or tissues of interest in medical imaging.

This chapter presented a detection method for bloblike structures, which are not clearly shown in clinical CT volumes. Lymph nodes regarded as bloblike structures were detected from the clinical CT volumes. Chapter 3 will present analysis of cardiac fibers. Chapter 3's topic presents many different aspects to mediastinal lymph node detection. Fiber-like structures are targeted for fiber tracking on the  $\mu$ CT volumes of animal hearts. While lymph node detection is clinically useful in lung cancer diagnosis, fiber tracking is beneficial for anatomical investigation of the heart.

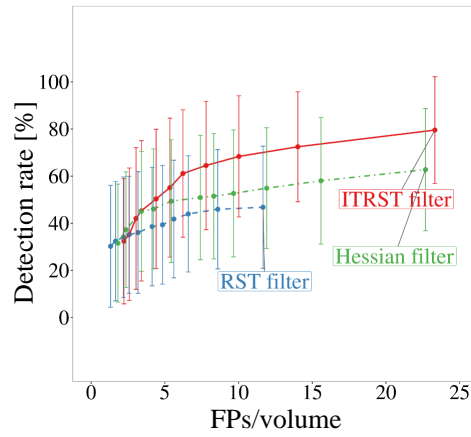
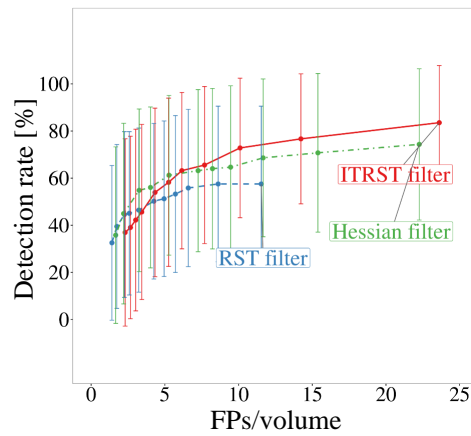
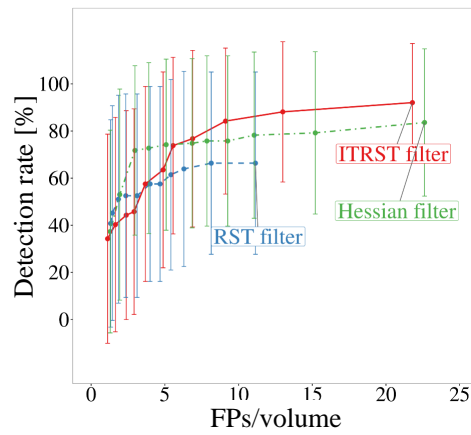
(a)  $r_{\text{target}} = 5$  mm(b)  $r_{\text{target}} = 7.5$  mm(c)  $r_{\text{target}} = 10$  mm

Figure 3.7: FROC curves obtained after FP reduction ( $w_F$  for 0.025, 0.05, 0.075, 0.10, 0.125, 0.15, 0.20, 0.25, 0.30, 0.40, and 0.50) with  $t_{\text{blob}} = 20$  for ITRST and RST filters, and  $t_{\text{blob}} = 2000$  for Hessian filter. (a)  $r_{\text{target}} = 5$  mm. (b)  $r_{\text{target}} = 7.5$  mm. (c)  $r_{\text{target}} = 10$  mm.

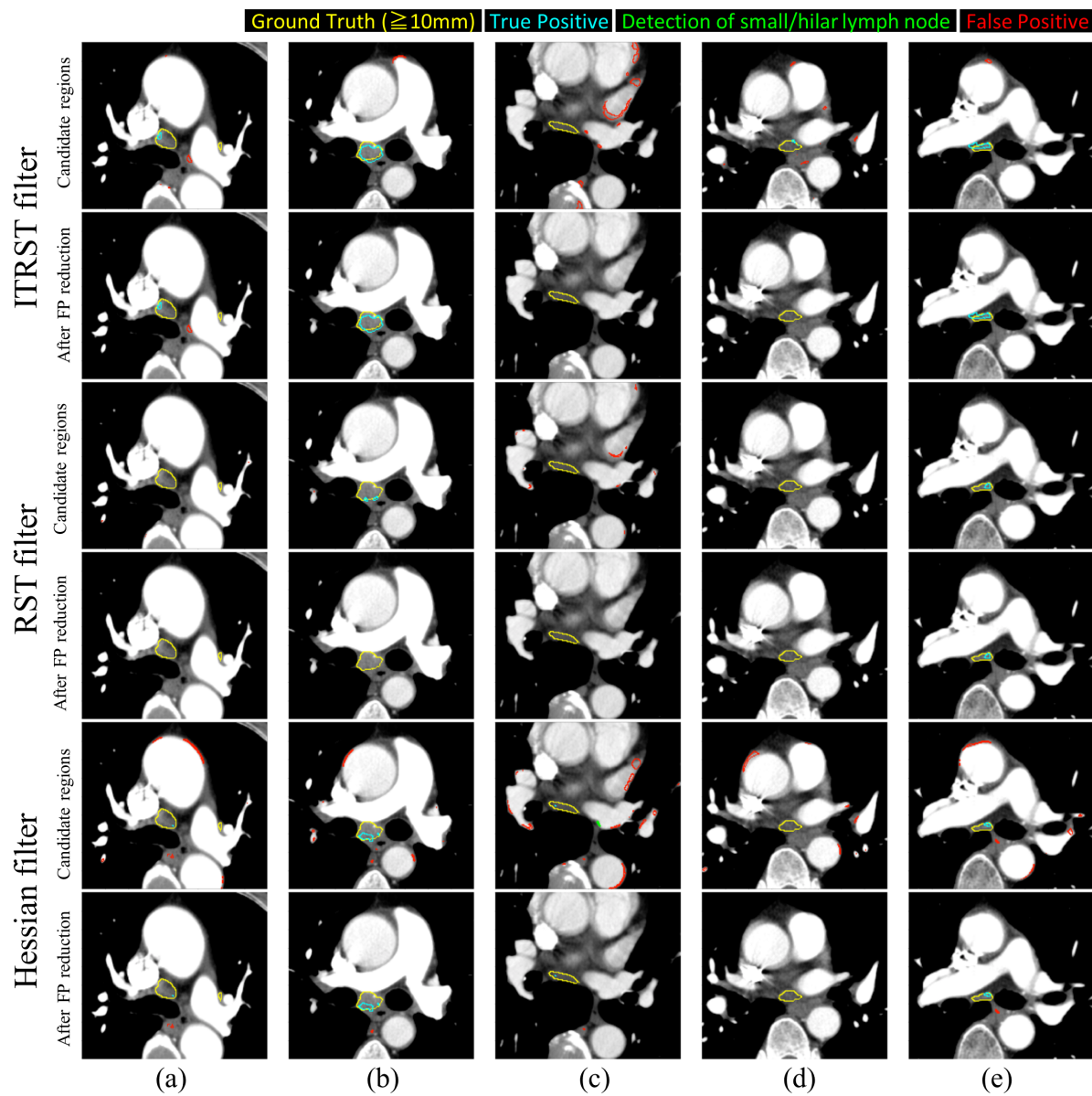


Figure 3.8: Examples of detection results (a)–(e) with parameters  $t_{\text{blob}} = 20$  and  $r_{\text{target}} = 10$  mm. Yellow denotes ground truth. Cyan denotes TP detection. Red denotes FP detection. Green represents detection of small or hilar lymph nodes. First two rows represent candidate regions and after FP reduction using ITRST filter. Third and fourth rows represent results of RST filter. Fifth and sixth rows are of Hessian filter.

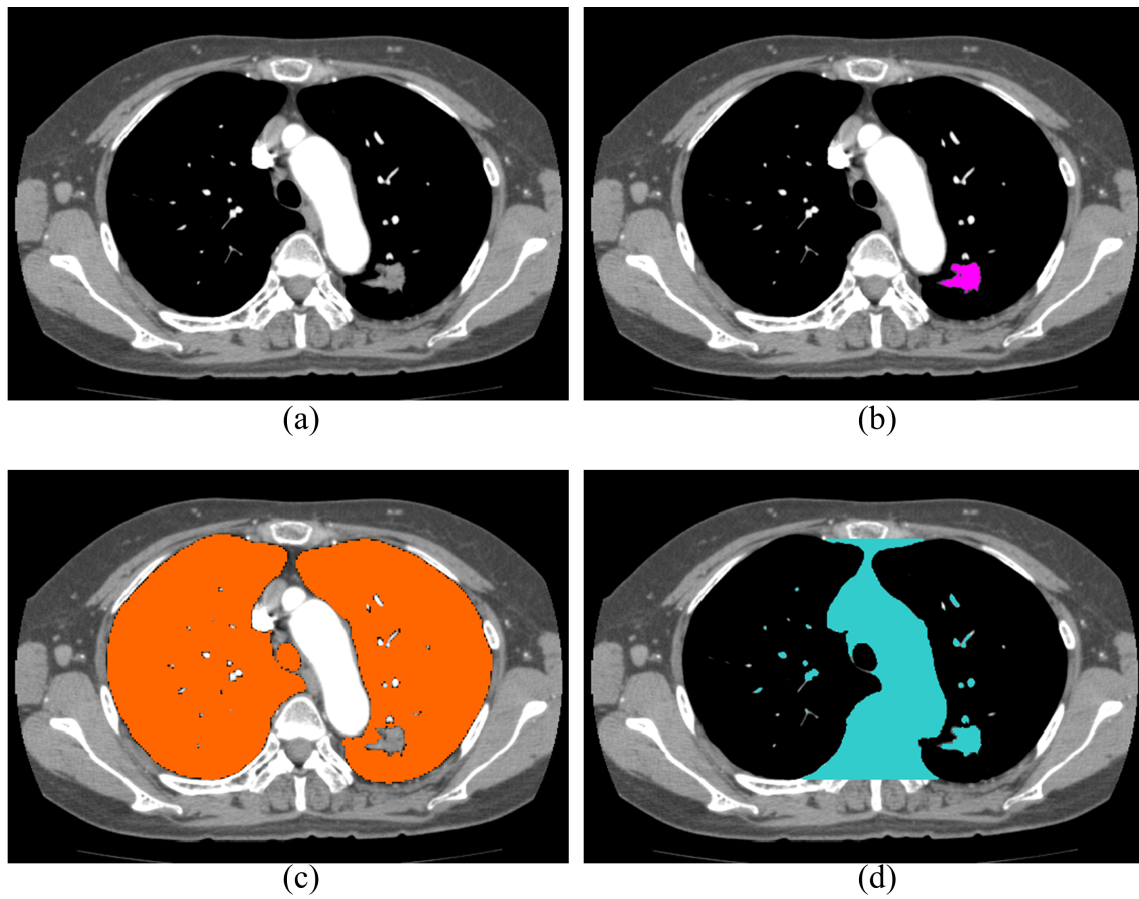


Figure 3.9: Target region extraction on volume having lung cancer region. (a) Input volume. (b) Lung cancer region. (c) Lung region. (d) Target region.

# Chapter 4

## Cardiac fiber tracking

### 4.1 Overview

In Chapter 3, we presented a mediastinal lymph node detection method from clinical CT volumes. Since mediastinal lymph nodes are surrounded by a variety of tissues, we are required to focus on small intensity gradients for detecting them. A filtering scheme was proposed for detecting those lymph nodes.

This chapter describes a different topic: cardiac fiber tracking on  $\mu$ CT volumes. 3D imaging of cardiac fibers by clinically available imaging techniques (e.g., CT, MRI) is infeasible. Since cardiac fibers are tiny, they cannot be represented by clinically utilized CT or MRI scanners. Even if  $\mu$ CT is used to scan animal hearts, the cardiac fibers are still vague and unclear. This is because cardiac fibers can be recognized by contrast with their extracellular matrices consisting of collagen. These regions are not clearly divided on  $\mu$ CT volumes, and air- and non-air regions are not separated.

We discovered  $\mu$ CT's usefulness for anatomical investigation in 3D. The efficacy of  $\mu$ CT volumes is evaluated by comparing them with another high-end scanning technique. This chapter is based on a paper entitled "**Cardiac fiber tracking on super**

high-resolution CT images: A comparative study” [88] published in the Journal of Medical Imaging in 2020.

## 4.2 Background

A deep understanding of the cardiac fiber structure in the left ventricle (LV) is required to understand cardiac anatomy and such diseases as heart failure. 6.5 million people experienced heart failure between 2011 and 2014 in the United States [236]. Although the fiber structure may also be changed by heart failure, the details have not been investigated deeply. High-resolution cardiac imaging and analysis methods in 3D space are needed.

Diffusion tensor magnetic resonance imaging (DT-MRI) is well-known for analyzing cardiac fiber structure [179, 180, 235]. With DT-MRI, we estimate the fiber orientation at a point as the orientation with the strongest diffusion of water molecules. However, DT-MRI’s resolution is inadequate. For instance, Helm, et al. [179] used a 1.5 T CV/I MRI Scanner (General Electric) whose resolutions were 300, 300, and 800  $\mu\text{m}$  for each of three axes. Histopathological images have also been used [233, 237] for cardiac imaging with much higher resolution than DT-MRI. However, precise reconstruction of the heart’s stacked section images is complicated due to the tissue damage caused by cutting the sections and the banana problem [175]. 3D analysis from a heart’s histopathological stacks is challenging.

We explored two alternate imaging techniques: refraction-contrast X-ray CT (RCT) and micro-focus X-ray CT ( $\mu\text{CT}$ ). RCT [247, 248] is a 3D imaging technique, one type of phase-contrast CT scanning based on observing the refraction of X-rays. It has very high soft-tissue contrast, even for cardiac fibers. However, the RCT is not commercially available and cannot be utilized publicly because the RCT requires a synchrotron system.

$\mu$ CT is a commercially-available 3D imaging technique. Generally, scanning is done by observing the absorption of X-rays that run through target objects. The resolution, contrast, and image size vary, as do their price ranges. Some scanners observing phase shift have very high spatial resolutions; SCYSCAN 1727 (Bruker, United States) has the highest resolution: 0.35  $\mu$ m resolution). We utilize a relatively low-end type of scanner, inspeXio SMX-90CT Plus (Shimadzu, Japan), which only observes X-ray absorption. Its highest spatial resolution is around 5  $\mu$ m. Although cardiac fibers can be observed on the  $\mu$ CT volumetric images (volumes) produced by this scanner, their contrast is not as high as the RCT volumes.

This chapter first describes the fiber analysis method from the RCT or  $\mu$ CT volumes of the heart. Then, we evaluate how  $\mu$ CT produces proper fiber analysis results by comparing them with RCT. Fiber analysis consists of estimating the orientation and the tracking fibers. The results from a  $\mu$ CT volume are compared with those of an RCT volume. We prepared a heart specimen with our original protocols and scanned it with RCT and  $\mu$ CT, and registered their volumes. Using the registered RCT and  $\mu$ CT volumes, we compared the fiber orientation estimation results on a slice to check quantitatively whether the  $\mu$ CT volume produces similar fiber orientation estimation results as the RCT volume. Moreover, we tracked the fibers to investigate whether fiber orientation can be estimated well on the  $\mu$ CT volume in the entire LV. The experimental results demonstrated that  $\mu$ CT scanning could be utilized for cardiac fiber analysis. However, further investigation is required in differences in fiber analysis results on RCT and  $\mu$ CT.

## 4.3 Fiber analysis method

### 4.3.1 Overview

Our fiber analysis method consists of two schemes: (1) estimation of the fiber orientation and (2) fiber tracking.

We conducted scheme (1) for each voxel in the input CT volume to estimate the fiber orientation around the voxels to quantitatively analyze the fiber orientation statistics.

We performed scheme (2) on the entire CT volume to produce trajectories that follow the fibers. Scheme (1) must be performed during the tracking process. The scheme (2) is useful for qualitatively visualizing how fibers flow in the entire LV.

### 4.3.2 Fiber orientation estimation

Structure tensor (ST) analysis is commonly used for estimating the cardiac fiber orientation in  $\mu$ CT volumes [245, 246]. First, for each volume, we apply a Gaussian smoothing filter with a standard deviation  $\sigma_p$  to smooth the intensity gradients and empirically set  $\sigma_p = 20 \mu\text{m}$ .

ST  $\mathbf{T}(\mathbf{x})$  at voxel  $\mathbf{x}$  is defined:

$$\mathbf{T}(\mathbf{x}) = \sum_{\mathbf{x}' \in \mathcal{N}} w(\sigma_T, \|\mathbf{x} - \mathbf{x}'\|) \mathbf{g}(\mathbf{x}') \mathbf{g}^T(\mathbf{x}'), \quad (4.1)$$

where  $\mathcal{N}$  is a set of the neighboring voxels around  $\mathbf{x}$ ,  $\mathbf{x}'$  is one of the voxels in  $\mathcal{N}$ ,  $w(\sigma_T, \|\mathbf{x} - \mathbf{x}'\|)$  is the Gaussian weight with standard deviation  $\sigma_T$  and distance  $\|\mathbf{x} - \mathbf{x}'\|$  from the center, and  $\mathbf{g}(\mathbf{x}')$  is a local intensity gradient vector around  $\mathbf{x}'$ .  $\mathbf{T}(\mathbf{x})$  can be written as a  $3 \times 3$  matrix. The eigenvector of  $\mathbf{T}(\mathbf{x})$ , which corresponds to the smallest eigenvalue  $f(\mathbf{x})$ , is assumed to be a direction of the fiber orientation at  $\mathbf{x}$ , which has the smallest intensity changes around  $\mathbf{x}$ . We set  $\sigma_T$  to  $400 \mu\text{m}$ .

### 4.3.3 Fiber tracking

We randomly generated  $N$  initial points in the mask of the LV region. From each initial point, fiber tracking was done by an iterative process. First (iteration  $k = 0$ ), we estimated the fiber direction vector  $\mathbf{f}(\mathbf{x}_0)$  at each initial point  $\mathbf{x}_0 \in \mathcal{I}$  using the structure tensor analysis described in Section 4.3.2. Since fibers are running in both positive and negative directions  $\mathbf{f}(\mathbf{x}_0)$  and  $-\mathbf{f}(\mathbf{x}_0)$ , fiber tracking was also performed for both directions. We calculated the endpoint coordinates of the trajectories at the  $k$ -th iteration ( $k > 0$ ):

$$\begin{aligned}\mathbf{x}_k &= \mathbf{x}_{k-1} + s\mathbf{f}(\mathbf{x}_{k-1}), \\ \mathbf{x}_{-k} &= \mathbf{x}_{-(k-1)} - s\mathbf{f}(\mathbf{x}_{-(k-1)}),\end{aligned}\tag{4.2}$$

where  $s$  represents the step size,  $\mathbf{f}(\mathbf{x}_{k-1})$  represents the orientation vector at  $\mathbf{x}_{k-1}$ , and  $\mathbf{f}(\mathbf{x}_{-(k-1)})$  represents the orientation vector at  $\mathbf{x}_{-(k-1)}$ . We terminated the tracking for each direction when  $\mathbf{x}_k$  or  $\mathbf{x}_{-k}$  was outside the LV mask, or index  $k$  of the iterations reached  $k_{\max}$ . We set the parameters to  $n_i = 1000$ ,  $s = 4$  voxels, and  $k_{\max} = 1000$ . The trajectories, which were tracked from all the initial points, are output.

## 4.4 Materials

### 4.4.1 Scanning

The following sequence obtained RCT and  $\mu$ CT volumes of a rabbit heart: (1) harvesting a heart, (2) ethanol fixation, (3) RCT scanning, (4) contrast enhancement, (5) rinse, and (6)  $\mu$ CT scanning. Fixation was performed once by using ethanol. I<sub>2</sub>KI was used for contrast enhancement for  $\mu$ CT scanning. Ethanol was used again in preparation for  $\mu$ CT scanning for rinsing excess I<sub>2</sub>KI to reduce artifact.

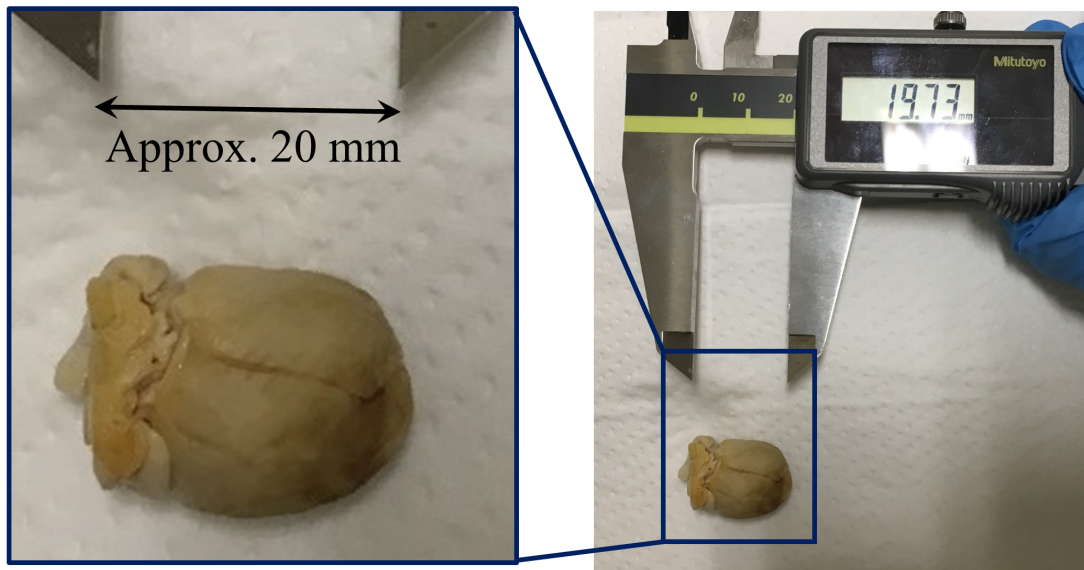
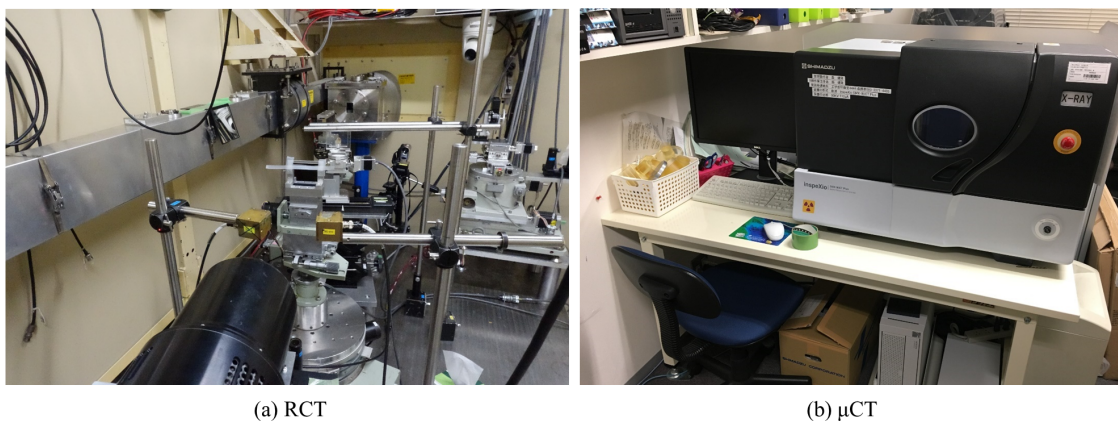


Figure 4.1: Rabbit heart: longest axis is about 20 mm.



(a) RCT

(b)  $\mu$ CT

Figure 4.2: Machines that scanned rabbit heart shown in Fig. 4.1: (a) RCT and (b)  $\mu$ CT

Specimen preparation and scanning procedures are as follows: We scanned one  $\mu$ CT and one RCT volume of the rabbit heart shown in Fig. 4.1 under the IRB approval of Nagoya University. We harvested the heart of a Japanese white rabbit (10-week-old

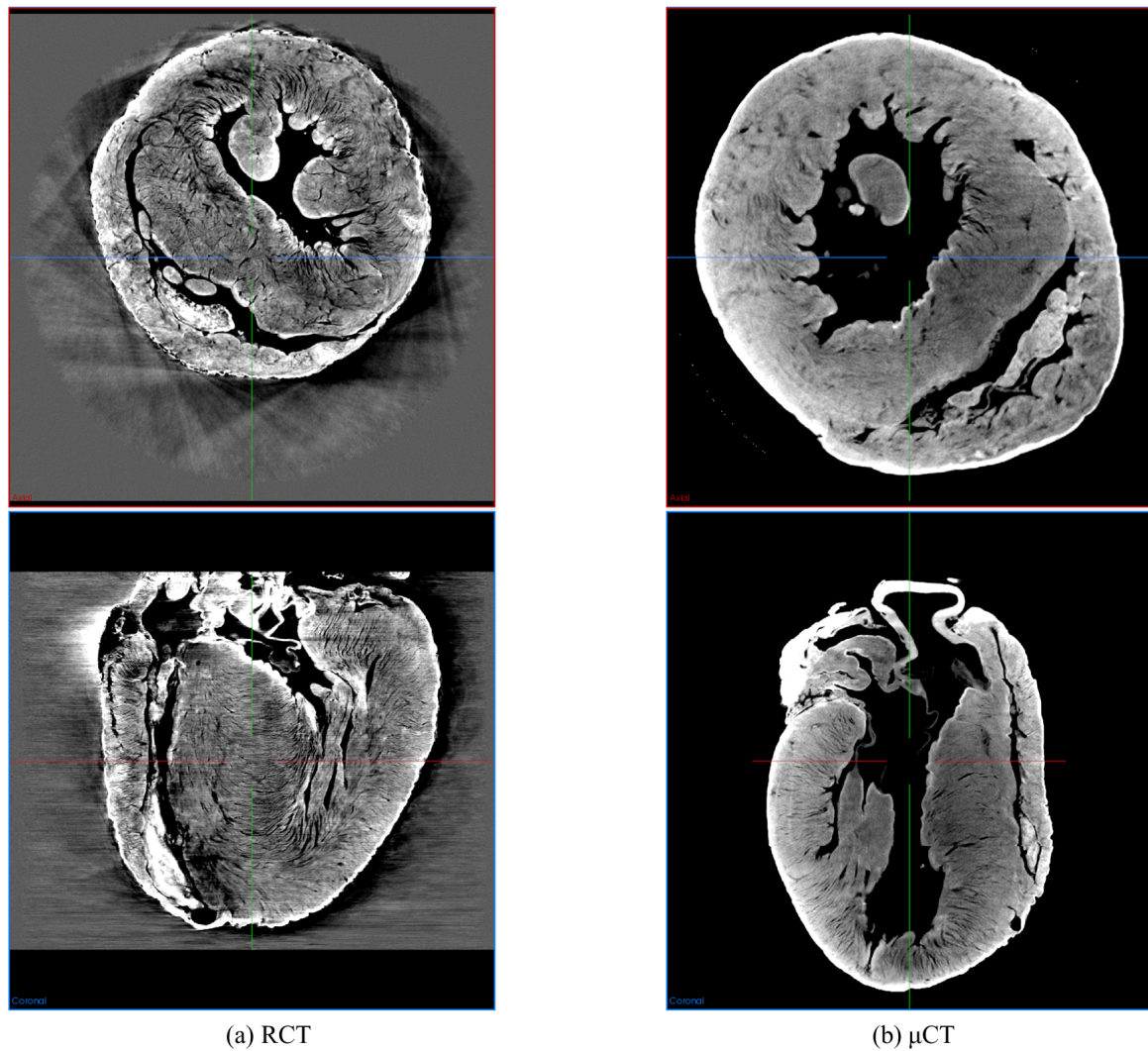


Figure 4.3: Axial and coronal slices of (a) RCT and (b)  $\mu$ CT volumes. Fibers on RCT volume look clearer than those of  $\mu$ CT volume. Registration is required for comparison due to different heart positions.

male) just after euthanasia with a KCl injection into the aortic arch and obtained a heart specimen. RCT scanning is as follows: (1) Ethanol fixation: The heart was fixated with an 80 % ethanol-water solution since ethanol fixation effectively improves the tissue contrast better than formalin fixation for the other phase-contrast imagings of hearts [238]. (2) RCT scanning: RCT scanning was performed using the synchrotron system

Table 4.1: Specification of RCT scanning.

Item	Value
Location for scanning	Photon Factory, High Energy Accelerator Research Organization (Tsukuba, Japan)
Camera	VHR 16 M (Photonics Science)
X-ray optical system	X-ray dark field imaging
Resolution	$15 \mu\text{m} \times 15 \mu\text{m} \times 15 \mu\text{m} / \text{voxel}$
Volume size	$1600 \times 1600 \times 1240 \text{ voxels}$
X-ray energy	19.8 keV

developed by Ando et al.'s group (Fig. 4.2(a)) at the High Energy Accelerator Research Organization (KEK) (Japan) [170]. The synchrotron system used for RCT scanning was built in about 177 million USD (1 USD = 110 JPY)[171]. The specification of the RCT scanning is listed in Table 4.1. Axial and coronal slices of the RCT volume are shown in Fig. 4.3(a).

After RCT scanning, we scan the same heart specimen in the following manner. The additional staining process is introduced for  $\mu\text{CT}$  scanning. The processes are (1) Contrast enhancement: We stained the rabbit heart with a 7.5% I<sub>2</sub>KI solution for one day. (2) Rinse. The heart is briefly rinsed with an 80 % ethanol solution. (3)  $\mu\text{CT}$  scanning. 4.2 shows scanning specification. Our scanner's field of view (FOV) was limited:  $1024 \times 1024 \times 548 \text{ mm}^3$  at  $17 \mu\text{m} \times 17 \mu\text{m} \times 17 \mu\text{m} / \text{voxel}$  resolution. It has a stitch-scanning mode to cover larger FOVs. We used this feature to cover the entire heart (three consecutive scanings). However, not every volume was aligned well in the stitching mode. Furthermore, the ring artifacts on the  $\mu\text{CT}$  volume were quite obvious. We used TomoPy [177] to reduce the ring artifacts, which are commonly observed in  $\mu\text{CT}$  volumes. Examples of the axial and coronal slices of the  $\mu\text{CT}$  volume are shown in Fig. 4.3(b).

This work used a desktop-type  $\mu\text{CT}$  scanner, inspeXio SMX-90CT Plus (Shimadzu, Japan) (Fig. 4.2(b)), which is a low-end, desktop type. The catalog price is approx-

Table 4.2: Specifications of  $\mu$ CT scanning

Item	Value
Location for scanning	Nagoya University (Nagoya, Japan)
Scanner	inspeXio SMX-90CT Plus (Shimadzu)
Resolution	$17 \mu\text{m} \times 17 \mu\text{m} \times 17 \mu\text{m} / \text{voxel}$
Volume size	$1024 \times 1024 \times 1627 \text{ voxels}$
# of divided-scanning parts	4
Tube voltage	90 kVp
Tube current	$110 \mu\text{A}$
# of X-ray projection	1200
# of projections for each angle	12

imately 236,000 USD (1 USD = 110 JPY). Ethanol fixation [238] is also suitable for  $\mu$ CT scanning in combination with contrast enhancement. Other  $\mu$ CT cardiac imaging works [239, 245] use high-end, much more expensive  $\mu$ CT scanners than ours. In those works, contrast enhancement continued for several days by staining the specimens in an iodine-potassium iodide ( $\text{I}_2\text{KI}$ ) solution. For instance, one trial by Stephenson et al. [239] stained a rabbit heart in a 7.5%  $\text{I}_2\text{KI}$  solution for three days with the Metris X-Tec custom 320kV bay system with 155kV tube voltage and  $150\text{-}\mu\text{A}$  tube current. However, directly using the same protocols as these references [239, 245] for our scanner caused artifacts since our scanner has lower X-ray energy.

#### 4.4.2 Registration

To compare the fiber analysis results, we registered the RCT volume as  $\mu$ CT. The heart's  $\mu$ CT and RCT volumes were cropped and rotated manually using the MITK Workbench 2016.11 [176]. The left ventricle (LV) is entirely covered with a slight margin around it and roughly aligned between the two volumes whose size and resolution were respectively adjusted into  $900 \times 980 \times 1080$  and  $18 \mu\text{m} \times 18 \mu\text{m} \times 18 \mu\text{m} / \text{voxels}$ . The coordinate system of these volumes is defined in Fig. 4.4. Since the parts of surround-

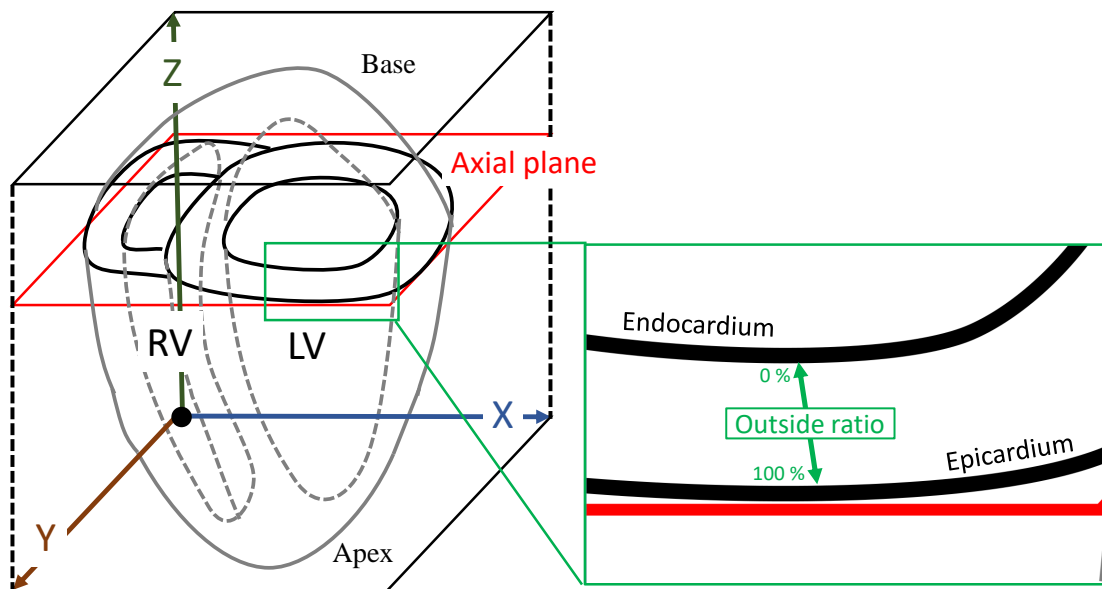


Figure 4.4: Coordinate system and position of ventricles: Axial planes (x-y plane) cut axis along base and apex into rounds. On axial planes, RV is shown on left of LV. Outside ratio is illustrated in magnified part. Outside ratio becomes 0 % at endocardium side and 100 % at epicardium side.

ing regions such as RV were also included, the processing target region was specified by masking. The mask of the LV region (LV mask) was segmented semi-automatically using the MITK Workbench 2016.11 [176] on the  $\mu$ CT volume. Then we applied non-rigid registration to the RCT volume to align it with the  $\mu$ CT volume. We used *deedsBCV*, which is open-source software published by Heinrich et al. [240].

Figures 4.5 (a) and (b) show the axial and coronal slices of the registration results. In Fig. 4.5(c), the two registered volumes' axial slices are shown as one figure after being merged to resemble a checkerboard. The RCT volume was successfully registered to the  $\mu$ CT volume. As shown in Fig. 4.5(c), the boundaries of the LV and the image patterns shown in both volumes were successfully aligned to each other.



analysis is conducted on one of those axial slices around the central part of the LV, focusing on fiber orientations. The 3D visualization of the fibers was performed by fiber tracking (Section 4.3.3).

## 4.5.2 Fiber orientation statistics

### Definition of outside ratio

Anatomical studies [234, 237] clarified that inside and outside of the LV tend to have different fiber orientations. Therefore, analyzing the fiber orientations may produce different results that correspond to their positions inside and outside the LV. We define *the outside ratio* measure as follows: it represents how each sample point is nearer outside the LV wall than inside it. The outside ratio becomes 0 % at the endocardium side and 100 % at the epicardium side, as illustrated in the magnified part of Fig. 4.4.

From the center point of the LV region on an axial slice, we performed radial searches to eight angles on an axial slice. On each search, we obtain a set of sample points whose outside ratios were 10, 20,  $\dots$ , or 90 %. On each sample point, we individually estimated the fiber orientation from the RCT and  $\mu$ CT volumes, where the axial slices cut the heart orthogonally to its longest axis (Fig. 4.4).

### Angle difference of $\mu$ CT from RCT

We define the *angle difference of  $\mu$ CT from RCT*  $\theta_1$ :

$$\theta_1 = \cos^{-1} \{ \mathbf{f}^\mu(\mathbf{x}) \cdot \mathbf{f}^R(\mathbf{x}) \} \quad (0 \leq \theta_1 \leq \pi), \quad (4.3)$$

where  $\mathbf{f}^\mu(\mathbf{x})$  and  $\mathbf{f}^R(\mathbf{x})$  represent the unit vectors of the fiber orientations estimated from the  $\mu$ CT and RCT volumes (Fig. 4.6(a)), respectively. Assuming the orientation from RCT is the ground-truth, the angle difference of  $\mu$ CT from RCT represents the

estimation error on  $\mu$ CT.

To evaluate how the fiber orientations estimated from  $\mu$ CT volumes are different from those of the RCT, we plotted the average and standard deviations of the angle difference of  $\mu$ CT from RCT at 100-slice intervals. We also visualized the angle differences of  $\mu$ CT from RCT on sample points on an axial slice around the central area.

### Inclination angle

*Inclination angle*  $\theta_2$  follows anatomical studies. Streeter et al. [237] defined fiber angle  $\alpha$  and showed that it becomes positive inside and negative outside the LV. Our definition of inclination angle resembles their definition, which can be computed in 3D volumes. As illustrated in Fig. 4.6(b), the inclination angle is defined:

$$\theta_2 = \cos^{-1} \{ \mathbf{f}(\mathbf{x}) \cdot \mathbf{p} \} \quad (-\pi < \theta_2 \leq \pi), \quad (4.4)$$

where  $\mathbf{f}(\mathbf{x})$  represents the estimated fiber orientation.  $\mathbf{p} = \frac{p(\mathbf{f}(\mathbf{x}))}{\|p(\mathbf{f}(\mathbf{x}))\|}$  represents a unit vector on the axial plane, written by the orthographic projection  $p(\mathbf{f}(\mathbf{x}))$  of  $\mathbf{f}(\mathbf{x})$  onto the axial plane.

We visualized the angle difference of  $\mu$ CT from RCT of each sample point on an axial slice around the central area. A scatter plot of the inclination angles computed from  $\mu$ CT and RCT was drawn. We also verified the statistical significance of the correspondence. We also observed the correlation between the outside ratio and the inclination angle for each volume. Their significant correlations suggest that the results follow the anatomical knowledge that the fiber orientations are different inside and outside LV.

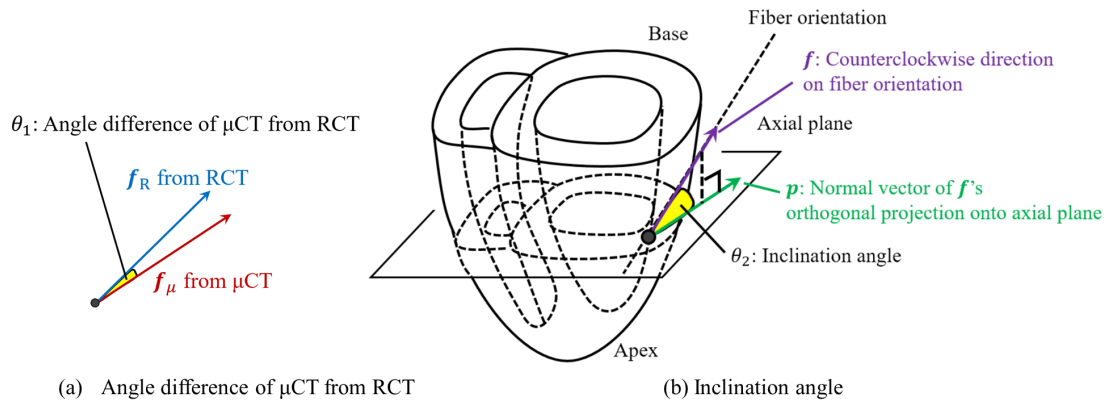


Figure 4.6: Definitions of angles: (a) Angle difference of  $\mu$ CT from RCT  $\theta_1$  and (b) Inclination angle  $\theta_2$

### 4.5.3 3D visualization of fibers

We performed 3D visualization using open-source software ParaView 5.3.0 [178] for each registered volume. This allows us to qualitatively compare the fiber trajectories from the RCT and  $\mu$ CT volumes in the entire LV. All points of the trajectories were colored to show the inclination angle. We showed all the tracking results. We trimmed the tracking results and showed whether, for the sagittal slices, the tracking was done properly in the entire LV. Since ParaView crashed when we directly opened the RCT or  $\mu$ CT volumes, we downsampled these volumes twice by cubic interpolation before opening them.

## 4.6 Results

### 4.6.1 Fiber orientation statistics

Figure 4.7 shows the mean and standard deviation of the angle differences of  $\mu$ CT from RCT on the axial slices throughout the LV. Most axial slices had a mean angle difference

of  $\mu$ CT from RCT of around 20 degrees. For instance, the mean and standard deviations of the angles were  $21.8^\circ \pm 20.5$  on an axial slice around the central part. Figure 4.8 shows the angle differences of  $\mu$ CT from RCT on a manually selected slice (depth = 8.85 mm. see Fig. 4.7). In Fig. 4.8, fiber orientations at a sample point are represented as two cylinders. A white cylinder shows fiber orientation estimated from the RCT volume. The colored cylinder shows fiber orientation estimated from the  $\mu$ CT volume and is colored according to their angle difference of  $\mu$ CT from RCT .

Figure 4.9 also shows estimated fiber orientations. Cylinders show estimated fiber orientation and are colored according to their inclination angles in this figure.

The relationship of inclination angles measured in the RCT and  $\mu$ CT volumes are shown in Fig. 4.10. Each circle in Fig. 4.10 is gray-scale coded based on the outside ratio. The inclination angles estimated from the RCT and  $\mu$ CT volumes had a correlation coefficient (CC) of 0.63. No significant difference was observed by Spearman's significant test:  $p < 2.2 \times 10^{-16}$ . This result shows that  $\mu$ CT produced fiber analysis results that resembled those of RCT. The inclination angles of RCT and the outside ratio also show a significant correlation:  $p = 2.4 \times 10^{-6}$  with a CC of -0.48. Those of the  $\mu$ CT and the outside ratio are  $p = 1.2 \times 10^{-7}$  and showed a correlation with a CC of -0.53.

#### 4.6.2 3D visualization of fibers

Figure 4.11 shows the fiber trajectories cropped along the coronal plane and a sagittal slice of the  $\mu$ CT or RCT volumes. Colors showing the inclination angles are red inside the LV and green outside it. These color tendencies visually confirm the correspondence of the outside ratio and the inclination angles. However, from the  $\mu$ CT results (Fig. 4.11(b)), some fiber tracking results were flat and densely gathered. This tendency was not observed in the RCT results (Fig. 4.11(a)). These incorrect tracking results from the  $\mu$ CT volume were caused by the joints produced by the scanning procedure,

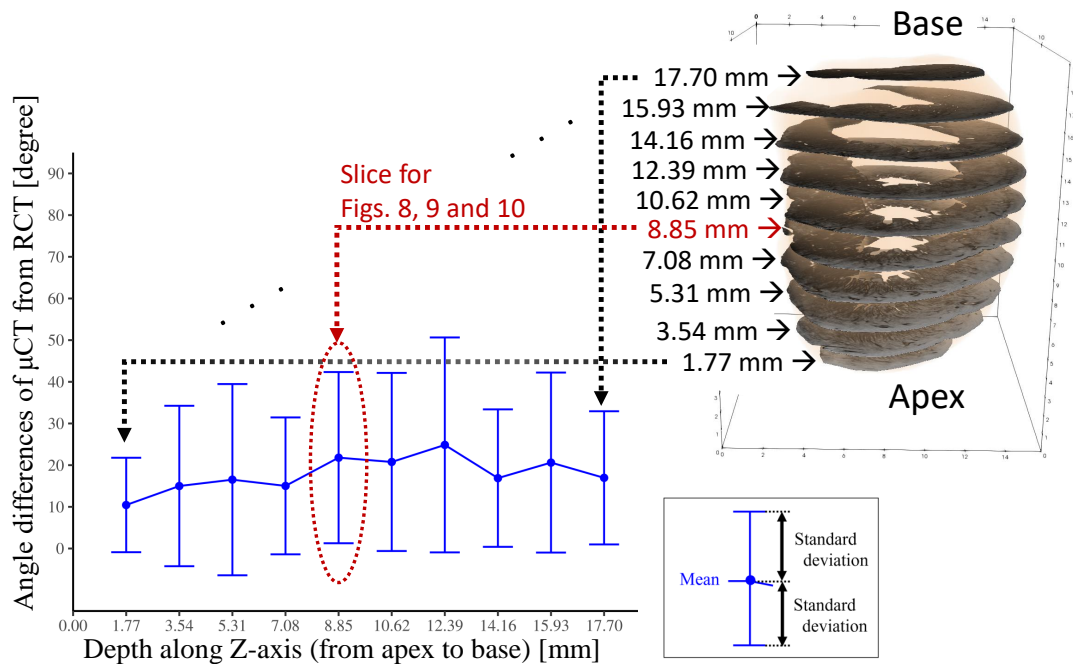


Figure 4.7: Mean and standard deviation of angle differences of  $\mu$ CT from RCT at sample points on each axial slice: Target axial slices were selected at 100-slice intervals along Z-axis (longest axis from apex to base) of RCT and  $\mu$ CT volumes. Each point on graph shows mean angle differences of  $\mu$ CT from RCT of a sample point on slice, and error bars represent standard deviation. Sample points on each slice were defined by a radial search scheme, explained in Section 4.5.2. Results do not greatly vary throughout the entire LV. Slice located at depth 8.85 mm is used for further evaluation in Figs. 4.8, 4.9 and 4.10 is pointed by arrow.

as explained in Section 4.4.1.

## 4.7 Discussions

### 4.7.1 Fiber orientation statistics

The  $\mu$ CT visually had lower contrast for the heart shown in Figs. 4.3 and 4.5. The fiber orientation estimations were not very similar to those of the RCT volume, which had an

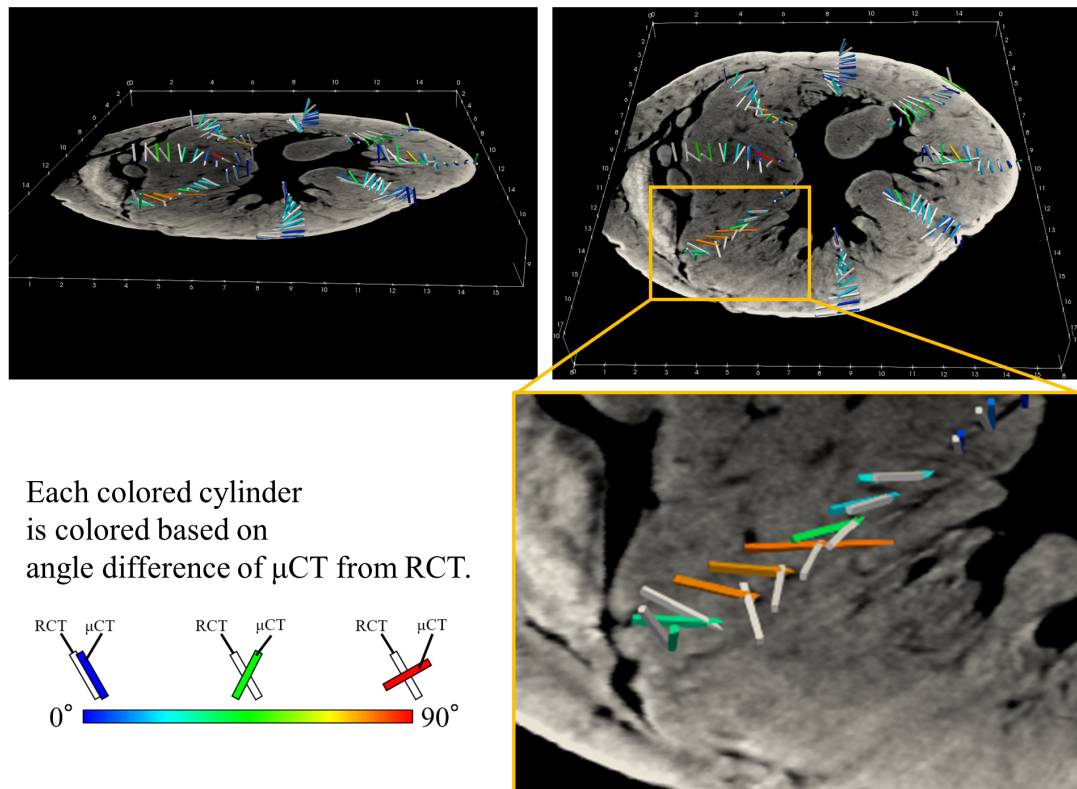


Figure 4.8: Angle differences of  $\mu$ CT from RCT on manually selected slice (depth = 8.85 mm. see Fig. 4.7): Colored cylinders show fiber orientations estimated from  $\mu$ CT volume and are colored according to angle difference of  $\mu$ CT from RCT . Fiber orientations estimated from RCT volume are also shown as white cylinders.

average error of around 20 degrees (Fig. 4.7). The average error values were increased by outliers, like the red bars in Fig. 4.8.

In part magnified in Fig. 4.8, many outliers are observed. Those errors were caused by the artifact of iodine solution (having higher absorption of X-ray), used for contrast enhancement of  $\mu$ CT imaging, as shown in Fig. 4.8. This iodine solution made a strong artifact in a slice plane. The tracking algorithm traced this artifact and produced in-plane (flat) tracking.

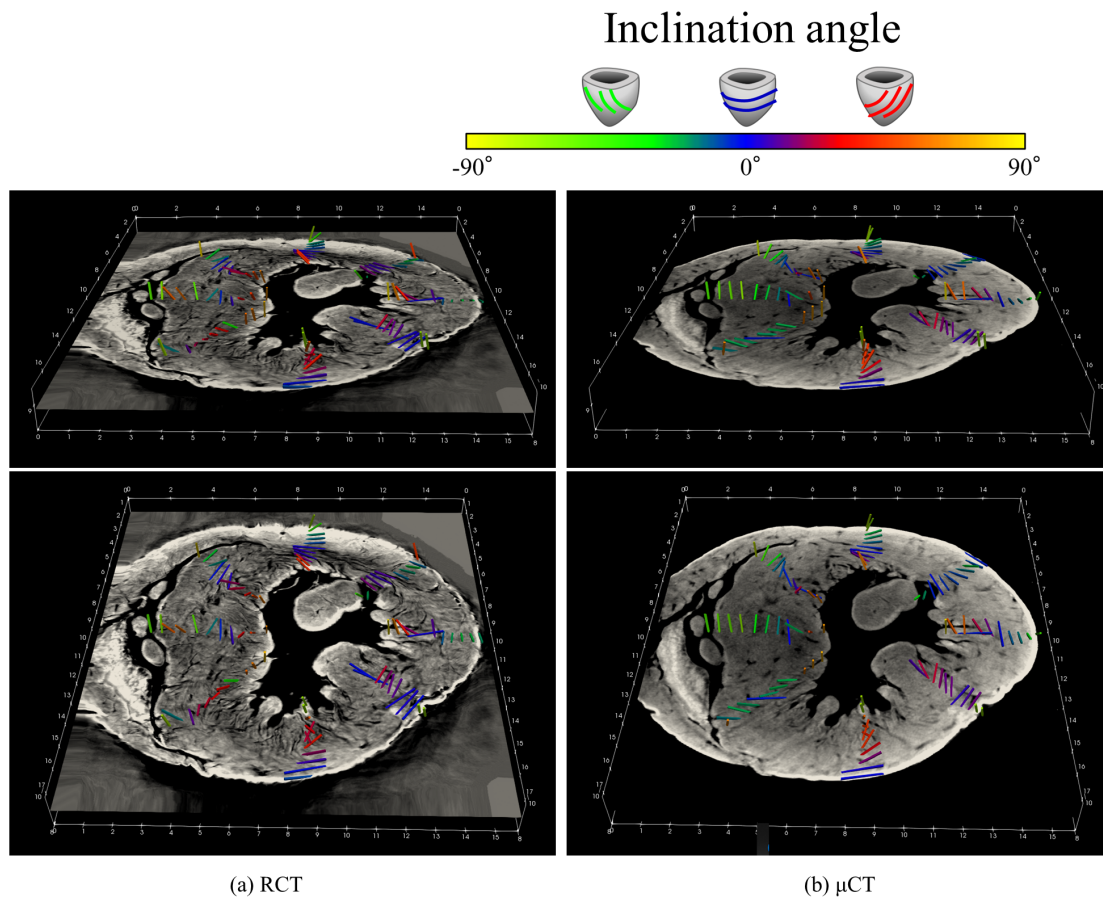


Figure 4.9: Fiber orientations on manually selected slice (depth = 8.85 mm. see Fig. 4.7) with coloring based on inclination angle: (a) RCT and (b)  $\mu$ CT. Cylinders show estimated fiber orientations, and colors represent inclination angles.

The colors of the points in Fig. 4.9 suggest that the inclination angles computed from both the RCT and  $\mu$ CT volumes were positive inside and negative outside the LV. This tendency was already proved through anatomical studies [237]. The results of both the  $\mu$ CT and RCT volumes followed it.

We used non-rigid registration to compensate for the specimen deformation at the scanning times of RCT and  $\mu$ CT. Our scanning procedures were performed in the following order: RCT scanning, iodine staining, and  $\mu$ CT scanning, as explained in 3.1. Iodine

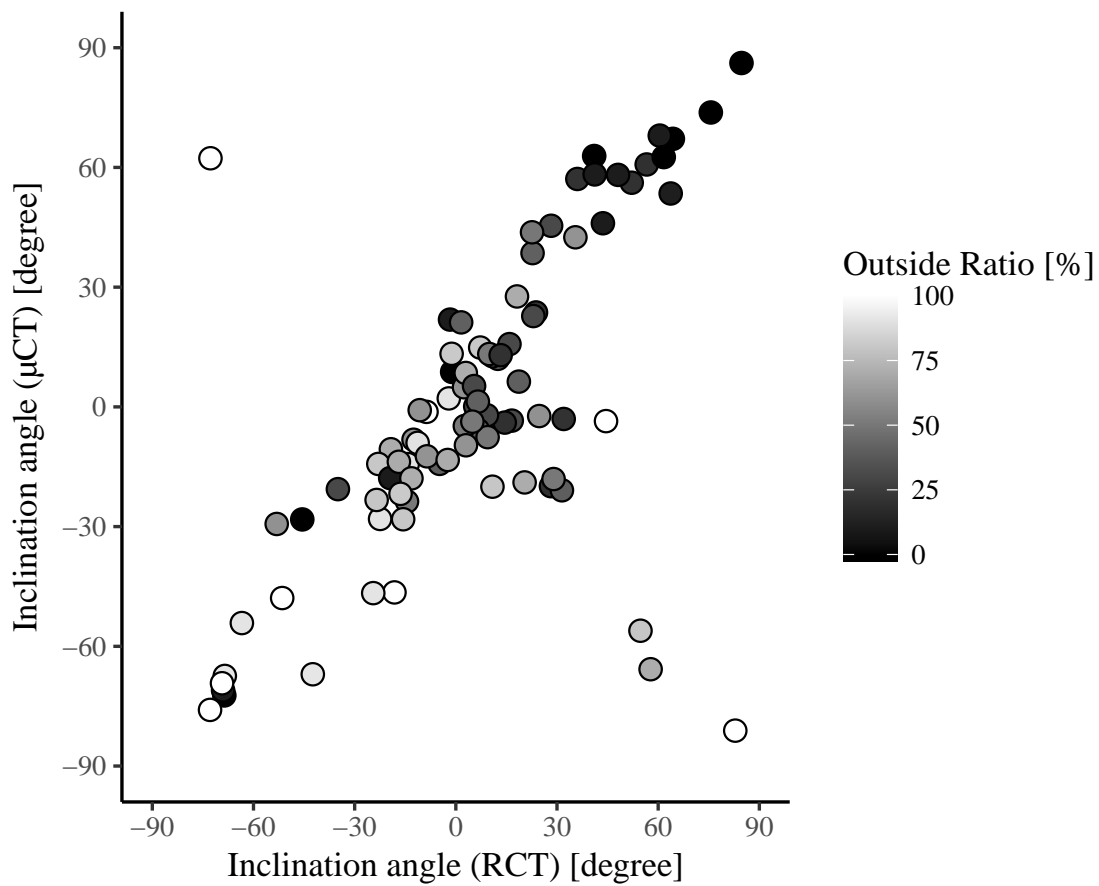


Figure 4.10: Relationship of inclination angles measured in RCT and  $\mu$ CT volumes. We manually selected slice (depth = 8.85 mm. see Fig. 4.7) and plot inclination angles measured on selected slice in this figure. Each circle is gray-scale coded based on outside ratio. From the figure, we can find positive correlation is clearly observed between inclination angles estimated from RCT and  $\mu$ CT volumes. Also, we can observe positive inclination angles in the outside area (epicardium).

staining causes a slight contraction of the heart. There are some changes in specimen sizes and small structures between two CT volumes.

### 4.7.2 3D visualization of fibers

Fiber tracking allows an intuitive understanding of fiber running orientations in 3D space. The tendency of inclination angles, correlated to the outside ratio, was also visually observed in the fiber tracking results from both the RCT and  $\mu$ CT volumes (Fig. 4.11). Most of the fiber tracking results inside the LV were red, and most of those outside were green. The trajectories were visually smooth from both volumes.

Figure 4.11 shows the fiber tracking results from the base to the apex. One large difference between the RCT and  $\mu$ CT volumes can be observed. On the results from the  $\mu$ CT volume (Fig. 4.11(b)), flat tracking results are densely gathered. Since our  $\mu$ CT scanner had a limited field of view, the rabbit heart was scanned by dividing it into three parts (Section 4.4.1). The images of the three scanning results were not precisely aligned. Their joints were followed by tracking. Correction processes for such mistracking are required in the future.

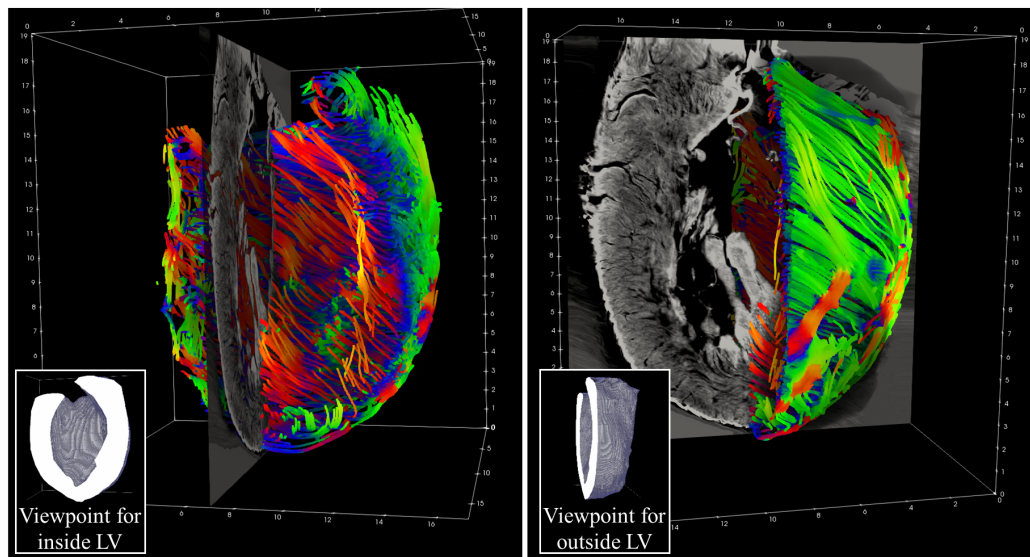
We found that it is possible to estimate fiber orientation on  $\mu$ CT volumes reasonably. Our fiber orientation estimation procedures were useful for fiber tracking in the entire LV. However, the results must be carefully observed about errors between the two scans.  $\mu$ CT, which is a promising imaging technique for cardiac imaging and useful for observing cardiac fibers, is commonly used by many companies and institutes for industrial purposes. Our work shows one of these cardiac imaging applications, which presents imaging protocols and their usefulness for observing cardiac fibers.

## 4.8 Conclusions and limitations

This chapter first describes our fiber analysis methods from the RCT or  $\mu$ CT volumes of the heart. Also, by comparing the results with RCT, we evaluated how  $\mu$ CT volumes produce reasonable analysis results. A rabbit heart was fixated by ethanol, scanned

by RCT, stained in an iodine solution, and then scanned by  $\mu$ CT. The RCT and  $\mu$ CT volumes were non-linearly registered. The fiber orientation of each point was estimated using the structure tensor analysis on each volume. We defined two measures, angle difference of  $\mu$ CT from RCT and inclination angles, to compare the fiber orientation estimation results at sample points of these volumes. Although promising results were obtained in the cardiac fiber analysis using  $\mu$ CT, we need to investigate the differences between  $\mu$ CT and RCT volumes further. Analysis results from both imaging techniques match the anatomical knowledge that fiber orientations are different inside and outside the left ventricle. Unfortunately, the  $\mu$ CT volume caused incorrect tracking around the boundaries due to stitching scanning. Smoothing around the boundaries will be a focus of our future work.

Our work suffers from the following limitations. First, we only had one specimen for the comparison experiments of two scans and their analysis. This is because we needed to use the synchrotron facility (Circumference: 187 m) shared by world-wide high-energy physics researchers for RCT scanning. Beamtime in the synchrotron facility is very expensive and very difficult to obtain. Thus, we only had one sample. We intend to increase the number of samples in our future work. Second, we must have quantitative validation of the fiber orientation results from the RCT volume used as ground-truth. Several manually-set parameters and the evaluation of different sets of parameters are also required. One idea for this work is to compare with histopathological sections. However, such a project is very challenging, as explained in Section 4.2. Therefore, future work will include more in-depth validation using many more hearts and quantitatively validating the fiber estimation of the structure tensors for RCT volumes. We would also like to find ways to observe fibers in the left ventricle and other parts and tissues in the heart.



(a) RCT

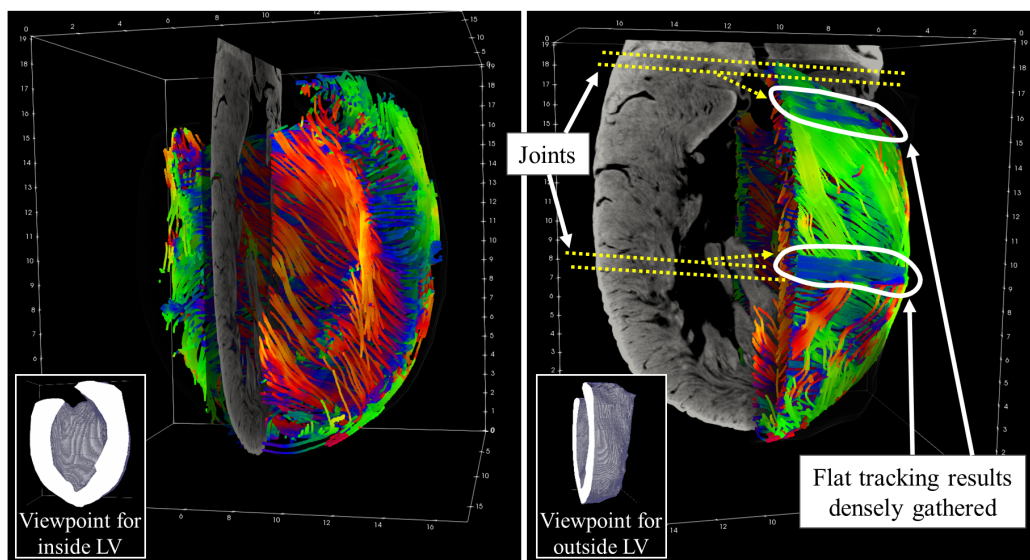
(b)  $\mu$ CT

Figure 4.11: Fiber tracking results with sagittal slice. Colors represent inclination angles. Two viewpoints were defined: one is useful for observing endocardium, and another is for epicardium. (a) RCT: Tracking was performed properly in entire LV. (b)  $\mu$ CT: Although closely resembling RCT results in (a), flat tracking results, densely gathered in joints, were produced due to scanning procedure, explained in Section 4.4.1.

# Chapter 5

## Summary and future work

### 5.1 Summary

#### 5.1.1 Overall conclusion

We focused on the anatomies in the thorax. Computational anatomy (Section 2.1.5) investigates the structures of anatomies from 3D images, which is essential for understanding human and animal bodies. Segmentation methods allow us to investigate the sizes and shapes of each anatomy. Detection methods allow us to find and locate scattered tissues. Fiber tracking methods reveal fiber structures.

The main problem that we tackled in this thesis is that these small anatomies are usually unclear and vague on images. CT and MRI are feasible candidates for 3D imaging of anatomies in the human body's thorax. Spatial resolutions of these scanning techniques are not as small as optical or electron microscopes. Smaller objects do not tend to be represented very clearly in images. We addressed two topics toward revealing the anatomical structures of these small organs and tissues that appear vague and unclear in 3D images.

Characteristics of materials and scanning techniques may cause images to be unclear.

MRI requires a long time for scanning and it is difficult to generate clear MRI volumes for moving organs, including the heart. Also, MRI detects protons in hydrogen atoms. T1- or T2-MRI images do not show tissues that do not contain much water or fat.

CT utilizes X-rays, which generate a high contrast between the air and non-air regions. However, the contrast between multiple non-air regions may be low on CT volumes. In this thesis, we addressed the two topics listed below.

### 5.1.2 Mediastinal lymph node detection

The first topic was a proposal of a filter-based detection approach. Mediastinal lymph node detection method from CT volumes was proposed in Chapter 3.

As mentioned in Section 1.4, mediastinal lymph nodes have been detected by filter-based or texture-feature-based approaches. The texture-feature-based approaches learn lymph nodes' appearances using the training dataset. Although the texture-feature-based approaches are robust for various appearances, it is difficult for us to understand target tissues' appearances.

The filter-based approaches are usually utilized with manually-defined characteristics as if "bloblike tissues brighter than surroundings." However, the mediastinal lymph nodes are tissues scattered around the main branches of the bronchus. There are various regions around each lymph node, such as air, contrast-enhanced blood vessels, and soft tissues. Lymph node boundaries tend to be unclear.

We proposed a filtering technique for mediastinal lymph nodes that can detect lymph nodes surrounded by various regions. This is a novel filtering approach, which is robust for various appearances. Since lymph nodes were in the specific intensity range, the analysis was performed only in the range.

Initial detection of mediastinal lymph nodes was performed by the filter based on the ITRST analysis. While most mediastinal lymph nodes were detected, many false

positives were also produced on regions that satisfy the filter's detection target's robustly defined characteristics. The support vector machine was introduced for removing those false positives.

Experiments were performed by 47 chest CT volumes of lung cancer patients. For lymph nodes whose short axis was at least 10 mm, the proposed method's detection rate was 84.2 %, with 9.1 false positives per volume. The proposed method outperformed the conventional filtering methods, the Hessian and RST analyses.

### 5.1.3 Cardiac fiber tracking

The second topic was an evaluation for a structure-tensor-based fiber-tracking approach. Cardiac fiber tracking on a  $\mu$ CT volume of a rabbit heart was reported in Chapter 4.

Since clinical CT or MRI volumes do not represent cardiac fibers (Fig. 1.3), the micro-focus X-ray CT ( $\mu$ CT) was utilized for imaging. Even on  $\mu$ CT volumes, which have a higher spatial resolution than clinical CT or MRI volumes, cardiac fibers were still unclear and vague. Therefore, an evaluation of  $\mu$ CT volumes' efficacy for fiber tracking was presented.

The  $\mu$ CT volume of a rabbit heart acquired by a desktop-type scanner was utilized.  $\mu$ CT volumes acquired by a desktop-type scanner do not provide clear cardiac fiber images. On  $\mu$ CT volumes, cardiac fibers can be observed as a little contrast between the fibers and their extracellular matrices consisting of collagen. Fiber tracking results were compared with those of another imaging technique, RCT volumes. Evaluating the efficacy of  $\mu$ CT volumes for fiber tracking is essential for further anatomical studies using  $\mu$ CT.

Even though cardiac fibers on  $\mu$ CT volumes were more unclearly shown than on the RCT volume, estimation results of cardiac fiber orientations were similar to those of the RCT volume, with a correlation coefficient of 0.63. Fiber tracking results of the two

imaging techniques were almost similar. However,  $\mu$ CT's problems were also revealed about the artifacts and the stitching scanning.

### 5.1.4 Further challenges

These two topics cover significant problems regarding the computational analysis of anatomies shown on low-contrast CT volumes. We discussed filter-based detection and structure tensor-based fiber tracking from a technical viewpoint. However, problems remain for anatomical investigation from 3D volumes.

- **Filtering for other structure types**

This thesis focused on the analysis of lymph nodes and cardiac fibers. Lymph nodes and cardiac fibers are regarded as bloblike and fiberlike structures, respectively.

Hessian-based filters [35, 120, 121, 126] have been widely utilized for various anatomies (Section 1.4). These filters can be customized for bloblike, linelike, or sheetlike structures. The structure tensor (RST) [130] is the basic technology of lymph node detection in Section 2. The RST can compose a filter for hollow-tube, which are bright on peripheral parts and dark around the centerlines.

Other structure types can be considered. The alveolar is a tiny structure in the lungs. The alveolar on  $\mu$ CT volumes [99] may be regarded as a hollow bloblike structure.

Furthermore, filtering for a broader viewpoint than such local structures can be considered. The bronchus on CT volumes is currently locally handled as a dark tube-like or a hollow tube-like structure. However, the bronchus consists of an airway tree from a broader viewpoint. The isolated alveolar is a hollow-blob on  $\mu$ CT volumes. However, in the lungs, many alveoli gather in a honeycomb shape. Thus, filters from broader viewpoints can be considered, including filters for a

hollow-tube treelike or honeycomb-like structure.

- **Analyses for other imaging techniques**

In this thesis, we investigated image processing for clinical CT and  $\mu$ CT volumes. However, we described many other imaging techniques in Section 2.2. Although MRI is widely utilized for the heart, cardiac MRI images of moving organs tend to be blurred. Anatomical analysis by such images remains a challenge.

- **Robust target setting for various diseases**

Prior shape information can be introduced for anatomies whose shapes or positions are almost fixed between patients, for example, cardiac chambers and blood-vessels. For instance, deformable models or probabilistic atlases are utilized (Section 1.4). For tissues or organs whose prior shape information is not suitable to apply, filtering techniques are useful (Section 2).

However, model-based or filter-based techniques have problems of robustness for manual target setting. For lymph nodes, another technique other than filtering is machine learning, e.g., texture-feature-based machine learning, deep learning. The problem with machine learning techniques is that they depend on the training dataset. A large number of training datasets should be gathered for training. Furthermore, those techniques might overlook regions having unique shapes or appearances caused by various diseases. Newly developing a scheme that is robust for abnormal appearances is desired.

- **Contrast enhancement or image converting techniques**

We focused on the problem of unclear images of anatomies. One approach which was not discussed in the thesis was contrast enhancement for preprocessing.

In Section 3, cardiac fibers were not very clearly shown on  $\mu$ CT volumes. One candidate approach that was not discussed is contrast enhancement of the  $\mu$ CT volumes. Furthermore, RCT was utilized to obtain a reference. Image conversion of  $\mu$ CT volumes to such high-contrast imaging techniques is also a candidate approach. Nowadays, many image conversion methods are available, such as CycleGAN-based methods [98]. Super-resolution techniques are also promising for analyzing small structures that are difficult to observe on available imaging techniques [97].

## 5.2 Blueprints

The goal of this research is to reveal detailed structures in the thorax. There is a variety of future work from both the anatomical and technical viewpoints.

### 5.2.1 Incorporating advantages of various imaging techniques

Each imaging technique has advantages. CT causes high contrast for organs containing air. MRI is widely used for organs that are stationary and contain water or fat. Ultrasonography allows clinicians to obtain real-time images inside the body. Incorporating the advantages of multiple imaging techniques may allow us to obtain more information. Currently, image registration methods [93, 95, 96] allow us to align images of different imaging techniques, phases, or patients.

Registration does not need to be limited to image-to-image alignment. Structure or information can be combined for further investigation. Current clinical practice is already doing a similar task. For example, breast cancer diagnosis utilizes both mammography (X-ray) and ultrasonography. Mammography is useful for evaluating calcification. Ultrasonography is helpful for finding small lumpiness, especially for patients

with well-developed mammary glands. Combining such practical techniques in a systematic approach can be the first step towards incorporation.

Furthermore, images from imaging techniques can be fused as an intermediate language. Image fusion [94] is currently utilized for observing images from different imaging techniques. This can be extended to image generation for intermediate languages, allowing clinicians or anatomists to understand information with little noise easily.

### 5.2.2 Assisting elementary or secondary education

Anatomical education is not only conducted in medical schools. Basic anatomical education is currently performed in elementary and high schools. Computational anatomical analysis can be applied for such educational purposes. Textbooks contain theoretical explanations and illustrations. Imaging and computational analysis allow students to understand the structures of visible materials in their schools and may help students understand the theories. Visualization techniques should be studied and developed much profoundly. For instance, animation of breathing simulations may be generated from the  $\mu$ CT volumes of a whole frog body.

### 5.2.3 3D imaging and analysis for microscopic anatomy

Today, microscopic anatomy (histology) is mainly studied with 2D microscopic images. Even on high-resolution microscopic images, it is challenging to understand 3D structures. As surveyed [218, 219], 3D reconstruction has been studied for both optical [191, 192] and electron [193, 220] microscopes. Another approach is the ultimate use of high-resolution 3D imaging techniques, including ( $\mu$ CT). Using these 3D imaging techniques for histological studies is not very common today because microscopes have the advantage of spatial resolution. However, X-ray imaging techniques at nanometer scale are now under improvement [194–196]. There are already some extensions to

3D imaging (nanotomography) [197], including applications to human or animal tissues [198, 199]. In the future, nanotomography may be more commonly utilized for histology [217].

As 3D imaging with nanotomography is expected in the future, computational anatomy should also be developed. Nanotomographic images might be more challenging to analyze than clinical or  $\mu$ CT because of their tiny spatial resolution. Depending on scanning systems or materials, images may be blurry. More complicated problems than we mentioned in this thesis should exist.

Removing borders between imaging techniques will also be desired. Even if nanotomography becomes commonly utilized and of high quality, microscopes still have advantages, such as color imaging. Clinical and  $\mu$ CT scanners are useful to scan wider regions than microscopes or nanotomography. Mutually sharing analysis results allows us to navigate from the entire body to inside cells.

#### **5.2.4 Deep learning techniques for various imaging techniques**

Deep learning techniques are currently widely utilized for image processing. However, deep learning techniques are not very common on images acquired by  $\mu$ CT or other imaging techniques that are not very common in the clinical field.

One reason is the lack of training datasets and the manually generated annotations required by most deep learning techniques. Even if  $\mu$ CT scanning is more common in the future, scanners and materials may still be specific for each study. The cost of collecting materials or images will remain high. Therefore, deep learning techniques should be improved so that they work without a large dataset. Promising studies including self-supervised [200, 201], unsupervised [215] and semi-supervised [213] learning are under improvement. In addition, high-resolution images, including  $\mu$ CT, are often large. Since deep learning often encounters GPU memory problems or over-fitting when large

images are input without downsampling, deep learning methods for large images are desired.

### 5.2.5 Finding unknown anatomies

There may still be anatomies of the body that have not yet been seen. In 2020, Valstar et al. [49] discovered the *tubarial salivary glands* in PET-CT images. This encourages us to search for unknown anatomies in the body. Collecting materials and images, and utilizing image processing techniques may lead to the discovery of unknown anatomies. It may be possible to extend abnormal shadow detection methods [129] to new imaging techniques or anatomies.

Non-clinical imaging techniques, including  $\mu$ CT, have enormous potential for finding unknown anatomies. Images may contain interesting tissues or lesions for experts of specific fields. Candidates of newly discovered tissues should be automatically detected and suggested to experts.



# Acknowledgments

I would like to express my sincere gratitude to every member who helped me with all of my work until now. Although I faced many difficult experiences before submitting this thesis, I was able to continue with the great help and uncountable advice offered by many people, especially at the Mori Laboratory.

I wish to first thank my supervisor, Prof. Dr. Kensaku Mori. He is a leading person in the medical imaging field and is famous all over the world. He has always guided me to the correct choices for research. I could not have finished, let alone started, my research without his invaluable instruction.

Prof. Dr. Takayuki Kitasaka (Aichi Institute of Technology) also helped me a lot, primarily through the subgroup meetings. His advice and suggestions always benefit my research progress. Dr. Masahiro Oda has always provided me with kind and warm advice, especially for papers and presentations. Dr. Yuichiro Hayashi's help was crucial to continuing my work, especially during my sick leave.

For works related to micro-focus X-ray CT, I would like to express my sincere thanks to all members of the Mori Laboratory, including Dr. Holger R. Roth (NVIDIA) and Dr. Takaaki Sugino (Tokyo Medical and Dental University). Since the micro-focus X-ray CT project was started from scratch, it was challenging for me to make decisions and continue my research. Since all members provided essential and warm discussions, I was able to meet the challenges of my research.

I would like to express my gratitude to Prof. Dr. Hiroshi Murase, Prof. Dr. Tomoki Toda, and Dr. Daisuke Deguchi, who reviewed my presentations and this thesis. Their advice and comments were essential to improving the quality of my work. Thanks to their advice, I was able to complete this thesis for submission.

Furthermore, I would like to formally express my sincere thanks to all the clinicians, medical students, and technicians that offered me datasets, materials, advice, and knowledge. Dr. Shingo Iwano is a radiologist who cooperated on the topic of mediastinal lymph nodes. Cardiovascular surgeon Prof. Dr. Toshiaki Akita and technician Ms. Noriko Usami selflessly helped with my work on cardiac imaging using micro-focus X-ray CT. Other topics were completed under the cooperation and guidance of many pediatric surgeons and medical students at Nagoya University Hospital.

Throughout my life at Mori Laboratory, any and all official procedures were supported by the secretaries Ms. Rie Ohashi, Ms. Yumiko Kobayashi, and Ms. Yumi Matsuiwa.

Finally, I acknowledge the kindness of all my family members. Their support has allowed me to happily face any challenge.

# References

- [1] 厚生労働省. 令和元年（2019）人口動態統計（確定数）の概況. 2019.
- [2] Stephen Bradley, Sarah Abraham, Adam Grice, Rocio Rodriguez Lopez, Judy Wright, Tracey Farragher, Beth Shinkins, and Richard D Neal. Sensitivity of chest X-ray for lung cancer: systematic review. *Br J Gen Pract*, Vol. 68, No. suppl 1, p. bjgp18X696905, 2018.
- [3] Phan T Huynh, Amanda M Jarolimek, and Susanne Daye. The false-negative mammogram. *Radiographics*, Vol. 18, No. 5, pp. 1137–1154, 1998.
- [4] Janice M Jenkins. Automated electrocardiography and arrhythmia monitoring. *Progress in cardiovascular diseases*, Vol. 25, No. 5, pp. 367–408, 1983.
- [5] Victor Hugo C de Albuquerque, Thiago M Nunes, Danillo R Pereira, Eduardo José da S Luz, David Menotti, João P Papa, and João Manuel RS Tavares. Robust automated cardiac arrhythmia detection in ECG beat signals. *Neural Computing and Applications*, Vol. 29, No. 3, pp. 679–693, 2018.
- [6] John Lynn Jefferies and Jeffrey A Towbin. Dilated cardiomyopathy. *The Lancet*, Vol. 375, No. 9716, pp. 752–762, 2010.
- [7] Heng-Da Cheng, XJ Shi, Rui Min, LM Hu, XP Cai, and HN Du. Approaches

- for automated detection and classification of masses in mammograms. *Pattern recognition*, Vol. 39, No. 4, pp. 646–668, 2006.
- [8] Xiangrong Zhou, Takuya Kano, Yunliang Cai, Shuo Li, Xinxin Zhou, Takeshi Hara, Ryujiro Yokoyama, and Hiroshi Fujita. Automatic quantification of mammary glands on non-contrast X-ray CT by using a novel segmentation approach. In *Medical Imaging 2016: Computer-Aided Diagnosis*, Vol. 9785, p. 97851Z. International Society for Optics and Photonics, 2016.
- [9] Albert Gubern-Mérida, Robert Martí, Jaime Melendez, Jakob L Hauth, Ritse M Mann, Nico Karssemeijer, and Bram Platel. Automated localization of breast cancer in DCE-MRI. *Medical image analysis*, Vol. 20, No. 1, pp. 265–274, 2015.
- [10] Cristina Gallego-Ortiz and Anne L Martel. A graph-based lesion characterization and deep embedding approach for improved computer-aided diagnosis of nonmass breast MRI lesions. *Medical image analysis*, Vol. 51, pp. 116–124, 2019.
- [11] P Herent, B Schmauch, P Jehanno, O Dehaene, C Saillard, C Balleyguier, J Arfi-Rouche, and S Jégou. Detection and characterization of mri breast lesions using deep learning. *Diagnostic and interventional imaging*, Vol. 100, No. 4, pp. 219–225, 2019.
- [12] Xiangrong Zhou, Mingxu Han, Takeshi Hara, Hiroshi Fujita, Keiko Sugisaki, Huayue Chen, Gobert Lee, Ryujiro Yokoyama, Masayuki Kanematsu, and Hiroaki Hoshi. Automated segmentation of mammary gland regions in non-contrast X-ray CT images. *Computerized Medical Imaging and Graphics*, Vol. 32, No. 8, pp. 699–709, 2008.
- [13] Nico Karssemeijer. Automated classification of parenchymal patterns in mammograms. *Physics in medicine & biology*, Vol. 43, No. 2, p. 365, 1998.

- [14] Luis Gonçalves, J Novo, and Aurélio Campilho. Hessian based approaches for 3D lung nodule segmentation. *Expert Systems with Applications*, Vol. 61, pp. 1–15, 2016.
- [15] Jun Wei, Yoshihiro Hagihara, Akinobu Shimizu, and Hidefumi Kobatake. Optimal image feature set for detecting lung nodules on chest X-ray images. In *CARS 2002 Computer Assisted Radiology and Surgery*, pp. 706–711. Springer, 2002.
- [16] Kenji Suzuki, Hiroyuki Abe, Heber MacMahon, and Kunio Doi. Image-processing technique for suppressing ribs in chest radiographs by means of massive training artificial neural network (MTANN). *IEEE Transactions on medical imaging*, Vol. 25, No. 4, pp. 406–416, 2006.
- [17] GN Balaji, TS Subashini, and N Chidambaram. Detection and diagnosis of dilated cardiomyopathy and hypertrophic cardiomyopathy using image processing techniques. *Engineering Science and Technology, an International Journal*, Vol. 19, No. 4, pp. 1871–1880, 2016.
- [18] Mahendra Khened, Varghese Alex, and Ganapathy Krishnamurthi. Densely connected fully convolutional network for short-axis cardiac cine MR image segmentation and heart diagnosis using random forest. In *International Workshop on Statistical Atlases and Computational Models of the Heart*, pp. 140–151. Springer, 2017.
- [19] 平岡昌和. 心電図自動診断の限界. *心電図*, Vol. 35, No. 2, pp. 149–155, 2015.
- [20] DigitalDiagnost Digital radiography solutions — Philips Healthcare. <https://www.usa.philips.com/healthcare/product/HC712220/digitaldiagnost-digital-radiography-system>.

- [21] Computed Tomography Products — Canon Medical Systems USA. <https://us.medical.canon/products/computed-tomography/>.
- [22] Ingenia Elition 3.0T X A revolutionary breakthrough in diagnostic quality and speed — Philips Healthcare. <https://www.usa.philips.com/healthcare/product/HC781358/ingenia-elition-30t-x>.
- [23] Bronchoscopes - Pulmonology - Olympus Medical Systems. <https://www.olympus-europa.com/medical/en/Products-and-Solutions/Products/Pulmonology/Bronchoscopes.html>.
- [24] Aplio i-Series — ultrasound — Canon Medical Systems. [https://global.medical.canon/products/ultrasound/aplio\\_i-series](https://global.medical.canon/products/ultrasound/aplio_i-series).
- [25] Ultra-High-Resolution Schottky Scanning Electron Microscope SU7000 : Hitachi High-Tech GLOBAL. [https://www.hitachi-hightech.com/global/product\\_detail/?pn=su7000](https://www.hitachi-hightech.com/global/product_detail/?pn=su7000).
- [26] Lung Nodule Detection from low dose CT scan using Optimization on Intel Xeon and Core processors with Intel Distribution of OpenVINO Toolkit. <https://builders.intel.com/ai/blog/lung-nodule-detection-ct-scan-xeon-core-opencvino>.
- [27] Frank Henry Netter. *Atlas of human anatomy: 2nd Edition*. Elsevier Science, 1998.
- [28] Thomas M Link, Volker Vieth, Christoph Stehling, Albrecht Lotter, Ambros Beer, David Newitt, and Sharmila Majumdar. High-resolution MRI vs multislice spiral CT: which technique depicts the trabecular bone structure best? *European radiology*, Vol. 13, No. 4, pp. 663–671, 2003.

- [29] Daniel Stucht, K Appu Danishad, Peter Schulze, Frank Godenschweger, Maxim Zaitsev, and Oliver Speck. Highest resolution in vivo human brain MRI using prospective motion correction. *PloS one*, Vol. 10, No. 7, p. e0133921, 2015.
- [30] Steffen Hahn, Till Heusner, Sherko Kümmel, Angelika Köninger, James Nagarah, Stefan Müller, Christian Boy, Michael Forsting, Andreas Bockisch, Gerald Antoch, et al. Comparison of FDG-PET/CT and bone scintigraphy for detection of bone metastases in breast cancer. *Acta radiologica*, Vol. 52, No. 9, pp. 1009–1014, 2011.
- [31] Holger R Roth, Le Lu, Ari Seff, Kevin M Cherry, Joanne Hoffman, Shijun Wang, Jiamin Liu, Evrim Turkbey, and Ronald M Summers. A new 2.5 d representation for lymph node detection using random sets of deep convolutional neural network observations. In *International conference on medical image computing and computer-assisted intervention*, pp. 520–527. Springer, 2014.
- [32] Holger R Roth, Hirohisa Oda, Xiangrong Zhou, Natsuki Shimizu, Ying Yang, Yuichiro Hayashi, Masahiro Oda, Michitaka Fujiwara, Kazunari Misawa, and Kensaku Mori. An application of cascaded 3D fully convolutional networks for medical image segmentation. *Computerized Medical Imaging and Graphics*, Vol. 66, pp. 90–99, 2018.
- [33] Jonathan Long, Evan Shelhamer, and Trevor Darrell. Fully convolutional networks for semantic segmentation. In *Proceedings of the IEEE conference on computer vision and pattern recognition*, pp. 3431–3440, 2015.
- [34] Philippe Despres and Xun Jia. A review of GPU-based medical image reconstruction. *Physica Medica*, Vol. 42, pp. 76–92, 2017.
- [35] Alejandro F Frangi, Wiro J Niessen, Koen L Vincken, and Max A Viergever. Mul-

- tiscale vessel enhancement filtering. In *International conference on medical image computing and computer-assisted intervention*, pp. 130–137. Springer, 1998.
- [36] Martin J Willeminck and Peter B Noël. The evolution of image reconstruction for CT—from filtered back projection to artificial intelligence. *European radiology*, Vol. 29, No. 5, pp. 2185–2195, 2019.
- [37] Nadia Kourra, Jason M Warnett, Alex Attridge, Aishah Dahnel, Helen Ascroft, Stuart Barnes, and Mark A Williams. A metrological inspection method using micro-CT for the analysis of drilled holes in CFRP and titanium stacks. *The International Journal of Advanced Manufacturing Technology*, Vol. 88, No. 5, pp. 1417–1427, 2017.
- [38] Jixuan Ya, Zhenguo Liu, and Yuanhang Wang. Micro-CT characterization on the meso-structure of three-dimensional full five-directional braided composite. *Applied Composite Materials*, Vol. 24, No. 3, pp. 593–610, 2017.
- [39] Esther Wehrle, Duncan C Tourolle né Betts, Gisela A Kuhn, Ariane C Scheuren, Sandra Hofmann, and Ralph Müller. Evaluation of longitudinal time-lapsed in vivo micro-CT for monitoring fracture healing in mouse femur defect models. *Scientific reports*, Vol. 9, No. 1, pp. 1–12, 2019.
- [40] Gabriela de Souza Balbinot, Vicente Castelo Branco Leitune, Deise Ponzoni, and Fabricio Mezzomo Collares. Bone healing with niobium-containing bioactive glass composition in rat femur model: A micro-CT study. *Dental Materials*, Vol. 35, No. 10, pp. 1490–1497, 2019.
- [41] Dylan B Smith, Galina Bernhardt, Nigel E Raine, Richard L Abel, Dan Sykes, Farah Ahmed, Inti Pedroso, and Richard J Gill. Exploring miniature insect brains using micro-CT scanning techniques. *Scientific reports*, Vol. 6, p. 21768, 2016.

- [42] Danny Poinapen, Joanna K Konopka, Joseph U Umoh, Chris JD Norley, Jeremy N McNeil, and David W Holdsworth. Micro-CT imaging of live insects using carbon dioxide gas-induced hypoxia as anesthetic with minimal impact on certain subsequent life history traits. *BMC Zoology*, Vol. 2, No. 1, pp. 1–13, 2017.
- [43] Zi Wang, Pieter Verboven, and Bart Nicolai. Contrast-enhanced 3d micro-CT of plant tissues using different impregnation techniques. *Plant methods*, Vol. 13, No. 1, p. 105, 2017.
- [44] Takashi Ijiri, Hideki Todo, Akira Hirabayashi, Kenji Kohiyama, and Yoshinori Dobashi. Digitization of natural objects with micro CT and photographs. *PloS one*, Vol. 13, No. 4, p. e0195852, 2018.
- [45] Karen M Steel, Robin E Dawson, David R Jenkins, Robin Pearce, and Merrick R Mahoney. Use of rheometry and micro-CT analysis to understand pore structure development in coke. *Fuel Processing Technology*, Vol. 155, pp. 106–113, 2017.
- [46] Sriharsha Gummadi, John Eisenbrey, Jingzhi Li, Zhaojun Li, Flemming Forsberg, Andrej Lyshchik, and Ji-Bin Liu. Advances in modern clinical ultrasound. *Advanced Ultrasound in Diagnosis and Therapy*, Vol. 2, No. 2, pp. 51–63, 2018.
- [47] Anton du Plessis, Ina Yadroitsava, and Igor Yadroitsev. Nondestructive micro-CT inspection of additive parts: how to beat the bottlenecks. In *29th Annual International Solid Freeform Fabrication Symposium—An Additive Manufacturing Conference*, 2018.
- [48] Deniz Aykac, Eric A Hoffman, Geoffrey McLennan, and Joseph M Reinhardt. Segmentation and analysis of the human airway tree from three-dimensional X-ray CT images. *IEEE transactions on medical imaging*, Vol. 22, No. 8, pp. 940–950, 2003.

- [49] Matthijs H Valstar, Bernadette S de Bakker, Roel JHM Steenbakkens, Kees H de Jong, Laura A Smit, Thomas JW Klein Nulent, Robert JJ van Es, Ingrid Hofland, Bart de Keizer, Bas Jasperse, et al. The tubarial salivary glands: A potential new organ at risk for radiotherapy. *Radiotherapy and Oncology*, 2020.
- [50] Visible Body. Human Anatomy Atlas, 2012.
- [51] Tianyi Zhao, Zhaozheng Yin, Jiao Wang, Dashan Gao, Yunqiang Chen, and Yunxiang Mao. Bronchus segmentation and classification by neural networks and linear programming. In *International Conference on Medical Image Computing and Computer-Assisted Intervention*, pp. 230–239. Springer, 2019.
- [52] Qier Meng, Takayuki Kitasaka, Yukitaka Nimura, Masahiro Oda, Junji Ueno, and Kensaku Mori. Automatic segmentation of airway tree based on local intensity filter and machine learning technique in 3d chest CT volume. *International journal of computer assisted radiology and surgery*, Vol. 12, No. 2, pp. 245–261, 2017.
- [53] Debora Gil, Carles Sanchez, Agnes Borrás, Marta Diez-Ferrer, and Antoni Rosell. Segmentation of distal airways using structural analysis. *Plos one*, Vol. 14, No. 12, p. e0226006, 2019.
- [54] Takafumi Nemoto, Natsumi Futakami, Masamichi Yagi, Atsuhiko Kumabe, Atsuya Takeda, Etsuo Kunieda, and Naoyuki Shigematsu. Efficacy evaluation of 2D, 3D U-net semantic segmentation and atlas-based segmentation of normal lungs excluding the trachea and main bronchi. *Journal of radiation research*, Vol. 61, No. 2, pp. 257–264, 2020.
- [55] Spyros G Marketos and Panagiotis Skiadas. Hippocrates: The father of spine surgery. *Spine*, Vol. 24, No. 13, p. 1381, 1999.

- [56] Todd Gustavson. *Camera: a history of photography from daguerreotype to digital*. Sterling Innovation, 2009.
- [57] LF Haas. Wilhelm conrad von röntgen (1845–1923). *Journal of Neurology, Neurosurgery & Psychiatry*, Vol. 70, No. 1, pp. 126–126, 2001.
- [58] Mark Nicholls. *Wilhelm C. Röntgen discoverer of X-rays*. 2019.
- [59] Rodrigo E Elizondo-Omaña, Santos Guzmán-López, and María De Los Angeles García-Rodríguez. Dissection as a teaching tool: past, present, and future. *The Anatomical Record Part B: The New Anatomist: An Official Publication of the American Association of Anatomists*, Vol. 285, No. 1, pp. 11–15, 2005.
- [60] RR Reverón. Herophilus and erasistratus, pioneers of human anatomical dissection. *Vesalius: acta internationales historiae medicinae*, Vol. 20, No. 1, pp. 55–58, 2014.
- [61] Marios Loukas, Michael Hanna, Nada Alsaiegh, Mohammadali M Shoja, and R Shane Tubbs. Clinical anatomy as practiced by ancient Egyptians. *Clinical Anatomy*, Vol. 24, No. 4, pp. 409–415, 2011.
- [62] Gianfranco Natale, Guido Bocci, and Domenico Ribatti. Scholars and scientists in the history of the lymphatic system. *Journal of anatomy*, Vol. 231, No. 3, pp. 417–429, 2017.
- [63] Saliha Seda Adanır and İlhan Bahşi. The giant anatomist, whose value is later understood: Bartolomeo eustachi. *Child's Nervous System*, pp. 1–4, 2019.
- [64] Sanjib K Ghosh and Ashutosh Kumar. Marcello malpighi (1628-1694): Pioneer of microscopic anatomy and exponent of the scientific revolution of the 17 th century. *Eur. J. Anat*, Vol. 22, No. 5, pp. 433–439, 2018.

- [65] Giovanni B Fogazzi. The description of the renal glomeruli by marcello malpighi. *Nephrology, dialysis, transplantation: official publication of the European Dialysis and Transplant Association-European Renal Association*, Vol. 12, No. 10, pp. 2191–2192, 1997.
- [66] Andres Kaech. An introduction to electron microscopy instrumentation, imaging and preparation. *Center for Microscopy and Image Analysis, University of Zurich*, 2013.
- [67] Stephanie McCann and Eric Wise. *Anatomy Coloring Book*. Simon and Schuster, 2017.
- [68] Johannes W Rohen, Chihiro Yokochi, and Elke Lutjen-Drecoll. *Anatomy: A Photographic Atlas*. Wolters Kluwer;, 2018.
- [69] Anne M Gilroy, Brian R MacPherson, Lawrence M Ross, Jonas Broman, and Anna Josephson. *Atlas of anatomy*. Thieme Stuttgart, 2008.
- [70] Jack Joseph. *Textbook of regional anatomy*. Macmillan International Higher Education, 1982.
- [71] Nancy L. Halliday and Harold M. Chung. *BRS Gross Anatomy*. Lippincott Williams & Wilkins, 2018.
- [72] Johan Hyllner, Chris Mason, and Ian Wilmut. *Cells: from robert hooke to cell therapy — a 350 year journey*, 2015.
- [73] Indra K Vasil. A history of plant biotechnology: from the cell theory of schleiden and schwann to biotech crops. *Plant cell reports*, Vol. 27, No. 9, p. 1423, 2008.
- [74] Hidefumi Kobatake and Yoshitaka Masutani. *Computational anatomy based on whole body imaging*. Springer, 2017.

- [75] Mats GL Gustafsson, DA Agard, JW Sedat, et al. I5M: 3D widefield light microscopy with better than 100nm axial resolution. *Journal of microscopy*, Vol. 195, No. 1, pp. 10–16, 1999.
- [76] Daisuke Shindo and Kenji Hiraga. Resolution limit of electron microscopes. *Bulletin of the Japan Institute of Metals*, Vol. 35, No. 11, pp. 1230–1234, 1996.
- [77] Michael Benjamin. *Surface Anatomy. The Anatomical Basis of Clinical Examination*, Vol. 177. Wiley-Blackwell, 1991.
- [78] Veronica Papa, Francesco Maria Galassi, Eugenio Polito, Giovanni Capelli, Angelo Rodio, Mauro Vaccarezza, Domenico Tafuri, and Elena Varotto. The muscles of the athletes to learn surface anatomy-the influence of classical statues on anatomy teaching. *Italian Journal of Anatomy and Embryology*, Vol. 124, No. 2, pp. 164–175, 2019.
- [79] Marcello Malpighi and Fundador de la Microanatomía. Marcello malpighi (1628-1694), founder of microanatomy. *Int. J. Morphol*, Vol. 29, No. 2, pp. 399–402, 2011.
- [80] John B West. Marcello malpighi and the discovery of the pulmonary capillaries and alveoli. *American Journal of Physiology-Lung Cellular and Molecular Physiology*, Vol. 304, No. 6, pp. L383–L390, 2013.
- [81] Regis Olry and Kaoru Motomiya. Paolo mascagni, ernest alexandra lauth and marie philibert constant sappey on the dissection and injection of the lymphatics. *J Int Soc Plastination*, Vol. 12, No. 2, pp. 6–7, 1997.
- [82] Ali M Elhadi, Samuel Kalb, Luis Perez-Orribo, Andrew S Little, Robert F Spetzler, and Mark C Preul. The journey of discovering skull base anatomy in ancient

- Egypt and the special influence of Alexandria. *Neurosurgical focus*, Vol. 33, No. 2, p. E2, 2012.
- [83] Anne MR Agur and Arthur F Dalley. *Grant's atlas of anatomy*. Lippincott Williams & Wilkins, 2009.
- [84] JOHN T HANSEN. Anatomy coloring book. *Hip*, Vol. 2, No. 16, pp. 2–17, 2010.
- [85] Susan Standring. *Gray's Anatomy: The Anatomical Basis of Clinical Practice*. Elsevier Health Sciences, 2015.
- [86] T Hampton, S Armstrong, and WJ Russell. Estimating the diameter of the left main bronchus. *Anaesthesia and intensive care*, Vol. 28, No. 5, pp. 540–542, 2000.
- [87] Lindsey A Torre, Rebecca L Siegel, and Ahmedin Jemal. Lung cancer statistics. *Lung Cancer and Personalized Medicine*, pp. 1–19, 2016.
- [88] Hirohisa Oda, Holger R Roth, Takaaki Sugino, Naoki Sunaguchi, Noriko Usami, Masahiro Oda, Daisuke Shimao, Shu Ichihara, Tetsuya Yuasa, Masami Ando, et al. Cardiac fiber tracking on super high-resolution CT images: a comparative study. *Journal of Medical Imaging*, Vol. 7, No. 2, p. 026001, 2020.
- [89] Robert Keys. Cubic convolution interpolation for digital image processing. *IEEE Transactions on Acoustics, Speech, and Signal Processing*, Vol. 29, No. 6, pp. 1153–1160, 1981.
- [90] Rebecca L Siegel, Kimberly D Miller, and Ahmedin Jemal. Cancer statistics, 2016. *CA: A Cancer Journal for Clinicians*, Vol. 66, No. 1, pp. 7–30, 2016.
- [91] Wanqing Chen, Rongshou Zheng, Peter D Baade, Siwei Zhang, Hongmei Zeng, Freddie Bray, Ahmedin Jemal, Xue Qin Yu, and Jie He. Cancer statistics in China, 2015. *CA: A Cancer Journal for Clinicians*, Vol. 66, No. 2, pp. 115–132, 2016.

- [92] Saeed Mirsadraee, Dilip Oswal, Yalda Alizadeh, Andrea Caulo, and Edwin JR van Beek. The 7th lung cancer TNM classification and staging system: Review of the changes and implications. *World Journal of Radiology*, Vol. 4, No. 4, pp. 128–134, 2012.
- [93] Timo Makela, Patrick Clarysse, Outi Sipila, Nicoleta Pauna, Quoc Cuong Pham, Toivo Katila, and Isabelle E Magnin. A review of cardiac image registration methods. *IEEE Transactions on medical imaging*, Vol. 21, No. 9, pp. 1011–1021, 2002.
- [94] Min Woo Lee. Fusion imaging of real-time ultrasonography with CT or MRI for hepatic intervention. *Ultrasonography*, Vol. 33, No. 4, p. 227, 2014.
- [95] Yujun Guo, Jasjit Suri, and Radhika Sivaramakrishna. Image registration for breast imaging: a review. In *2005 IEEE Engineering in Medicine and Biology 27th Annual Conference*, pp. 3379–3382. IEEE, 2006.
- [96] Yabo Fu, Yang Lei, Tonghe Wang, Walter J Curran, Tian Liu, and Xiaofeng Yang. Deep learning in medical image registration: a review. *Physics in Medicine & Biology*, 2020.
- [97] Tong Zheng, Hirohisa Oda, Takayasu Moriya, Takaaki Sugino, Shota Nakamura, Masahiro Oda, Masaki Mori, Hirotsugu Takabatake, Hiroshi Natori, and Kensaku Mori. Multi-modality super-resolution loss for GAN-based super-resolution of clinical CT images using micro CT image database. In *Medical Imaging 2020: Image Processing*, Vol. 11313, p. 1131305. International Society for Optics and Photonics, 2020.
- [98] Yuta Hiasa, Yoshito Otake, Masaki Takao, Takumi Matsuoka, Kazuma Takashima, Aaron Carass, Jerry L Prince, Nobuhiko Sugano, and Yoshinobu Sato. Cross-modality image synthesis from unpaired data using CycleGAN. In *International*

*workshop on simulation and synthesis in medical imaging*, pp. 31–41. Springer, 2018.

- [99] Henrik Watz, Andreas Breithecker, Wigbert Stephan Rau, and Andres Kriete. Micro-CT of the human lung: imaging of alveoli and virtual endoscopy of an alveolar duct in a normal lung and in a lung with centrilobular emphysema—initial observations. *Radiology*, Vol. 236, No. 3, pp. 1053–1058, 2005.
- [100] Jiamin Liu, Joanne Hoffman, Jocelyn Zhao, Jianhua Yao, Le Lu, Lauren Kim, Evrim B Turkbey, and Ronald M Summers. Mediastinal lymph node detection and station mapping on chest CT using spatial priors and random forest. *Medical Physics*, Vol. 43, No. 7, pp. 4362–4374, 2016.
- [101] Marco Feuerstein, Ben Glocker, Takayuki Kitasaka, Yoshihiko Nakamura, Shingo Iwano, and Kensaku Mori. Mediastinal atlas creation from 3-D chest computed tomography images: application to automated detection and station mapping of lymph nodes. *Medical Image Analysis*, Vol. 16, No. 1, pp. 63–74, 2012.
- [102] Takayuki Kitasaka, Yukihiro Tsujimura, Yoshihiko Nakamura, Kensaku Mori, Yasuhito Suenaga, Masaaki Ito, and Shigeru Nawano. Automated extraction of lymph nodes from 3-D abdominal CT images using 3-D minimum directional difference filter. In *International Conference on Medical Image Computing and Computer-Assisted Intervention*, pp. 336–343. Springer, 2007.
- [103] Jana Dornheim, Heiko Seim, Bernhard Preim, Ilka Hertel, and Gero Strauss. Segmentation of neck lymph nodes in CT datasets with stable 3d mass-spring models. In *International Conference on Medical Image Computing and Computer-Assisted Intervention*, pp. 904–911. Springer, 2006.
- [104] Jiayong Yan, Tian-ge Zhuang, Binsheng Zhao, and Lawrence H Schwartz. Lymph

- node segmentation from CT images using fast marching method. *Computerized Medical Imaging and Graphics*, Vol. 28, No. 1-2, pp. 33–38, 2004.
- [105] Yao Wang and Reinhard Beichel. Graph-based segmentation of lymph nodes in CT data. In *International Symposium on Visual Computing*, pp. 312–321. Springer, 2010.
- [106] Zijian Bian, Wenjun Tan, Jiren Liu, and Dazhe Zhao. Automated airway segmentation from chest CT images combined uniform and local intensities and airway topology structure. In *Tenth International Conference on Digital Image Processing (ICDIP 2018)*, Vol. 10806, p. 108065B. International Society for Optics and Photonics, 2018.
- [107] Wolfgang Sorgel and Vincent Vaerman. Automatic heart localization from a 4D MRI data set. In *Medical Imaging 1997: Image Processing*, Vol. 3034, pp. 333–344. International Society for Optics and Photonics, 1997.
- [108] James D Dormer, Ling Ma, Martin Halicek, Carolyn M Reilly, Eduard Schreibmann, and Baowei Fei. Heart chamber segmentation from CT using convolutional neural networks. In *Medical Imaging 2018: Biomedical Applications in Molecular, Structural, and Functional Imaging*, Vol. 10578, p. 105782S. International Society for Optics and Photonics, 2018.
- [109] Olivier Ecabert, Jochen Peters, Hauke Schramm, Cristian Lorenz, Jens von Berg, Matthew J Walker, Mani Vembar, Mark E Olszewski, Krishna Subramanyan, Guy Lavi, et al. Automatic model-based segmentation of the heart in CT images. *IEEE transactions on medical imaging*, Vol. 27, No. 9, pp. 1189–1201, 2008.
- [110] Ivana Isgum, Marius Staring, Annemarieke Rutten, Mathias Prokop, Max A Viergever, and Bram Van Ginneken. Multi-atlas-based segmentation with local

- decision fusion—application to cardiac and aortic segmentation in CT scans. *IEEE transactions on medical imaging*, Vol. 28, No. 7, pp. 1000–1010, 2009.
- [111] Hortense A Kirisli, Michiel Schaap, Stefan Klein, Lisan A Neefjes, Annick C Weustink, Theo Van Walsum, and Wiro J Niessen. Fully automatic cardiac segmentation from 3D CTA data: a multi-atlas based approach. In *Medical Imaging 2010: Image Processing*, Vol. 7623, p. 762305. International Society for Optics and Photonics, 2010.
- [112] Jochen Peters, Olivier Ecabert, Cristian Lorenz, Jens von Berg, Matthew J Walker, TB Ivanc, Mani Vembar, ME Olszewski, and Jürgen Weese. Segmentation of the heart and major vascular structures in cardiovascular CT images. In *Medical Imaging 2008: Image Processing*, Vol. 6914, p. 691417. International Society for Optics and Photonics, 2008.
- [113] H Abrishami Moghaddam and JF Lerallut. Volume visualization of the heart using MRI 4D cardiac images. *Journal of computing and information technology*, Vol. 6, No. 2, pp. 215–228, 1998.
- [114] Ardeshir Goshtasby and David A Turner. Segmentation of cardiac cine MR images for extraction of right and left ventricular chambers. *IEEE transactions on medical imaging*, Vol. 14, No. 1, pp. 56–64, 1995.
- [115] M-P Jolly, Nicolae Duta, and Gareth Funka-Lea. Segmentation of the left ventricle in cardiac MR images. In *Proceedings Eighth IEEE International Conference on Computer Vision. ICCV 2001*, Vol. 1, pp. 501–508. IEEE, 2001.
- [116] Majd Zreik, Tim Leiner, Bob D De Vos, Robbert W van Hamersvelt, Max A Viergever, and Ivana Išgum. Automatic segmentation of the left ventricle in car-

- diac CT angiography using convolutional neural networks. In *2016 IEEE 13th International Symposium on Biomedical Imaging (ISBI)*, pp. 40–43. IEEE, 2016.
- [117] Yu Lu, Xianghua Fu, Xiaoqing Li, and Yingjian Qi. Cardiac chamber segmentation using deep learning on magnetic resonance images from patients before and after atrial septal occlusion surgery. In *2020 42nd Annual International Conference of the IEEE Engineering in Medicine & Biology Society (EMBC)*, pp. 1211–1216. IEEE, 2020.
- [118] MR Avendi, Arash Kheradvar, and Hamid Jafarkhani. Fully automatic segmentation of heart chambers in cardiac MRI using deep learning. *Journal of Cardiovascular Magnetic Resonance*, Vol. 18, No. 1, pp. 1–3, 2016.
- [119] Minhoo Lee, June Goo Lee, Namkug Kim, Joon Beom Seo, and Sang Min Lee. Hybrid airway segmentation using multi-scale tubular structure filters and texture analysis on 3d chest CT scans. *Journal of Digital Imaging*, Vol. 32, No. 5, pp. 779–792, 2019.
- [120] Qiang Li, Shusuke Sone, and Kunio Doi. Selective enhancement filters for nodules, vessels, and airway walls in two-and three-dimensional CT scans. *Medical Physics*, Vol. 30, No. 8, pp. 2040–2051, 2003.
- [121] Yoshinobu Sato, Carl-Fredrik Westin, Abhir Bhalerao, Shin Nakajima, Nobuyuki Shiraga, Shinichi Tamura, and Ron Kikinis. Tissue classification based on 3D local intensity structures for volume rendering. *IEEE Transactions on Visualization and Computer Graphics*, Vol. 6, No. 2, pp. 160–180, 2000.
- [122] Yukitaka Nimura, Yuichiro Hayashi, Takayuki Kitasaka, Kazuhiro Furukawa, Kazunari Misawa, and Kensaku Mori. Automated abdominal lymph node seg-

- mentation based on RST analysis and SVM. In *SPIE Medical Imaging*, pp. 90352U–90352U. International Society for Optics and Photonics, 2014.
- [123] Adrian Barbu, Michael Suehling, Xun Xu, David Liu, S Kevin Zhou, and Dorin Comaniciu. Automatic detection and segmentation of lymph nodes from CT data. *IEEE Transactions on Medical Imaging*, Vol. 31, No. 2, pp. 240–250, 2012.
- [124] Kevin M Cherry, Shijun Wang, Evrim B Turkbey, and Ronald M Summers. Abdominal lymphadenopathy detection using random forest. In *SPIE Medical Imaging*, pp. 90351G–90351G. International Society for Optics and Photonics, 2014.
- [125] Leo Breiman. Random forests. *Machine Learning*, Vol. 45, No. 1, pp. 5–32, 2001.
- [126] Alejandro F Frangi, Wiro J Niessen, Romhild M Hoogeveen, Theo Van Walsum, and Max A Viergever. Model-based quantitation of 3-D magnetic resonance angiographic images. *IEEE Transactions on Medical Imaging*, Vol. 18, No. 10, pp. 946–956, 1999.
- [127] 日本医用画像工学ハンドブック編集委員会. 医用画像工学ハンドブック. 日本医用画像工学会, 2012.
- [128] Alex Krizhevsky, Ilya Sutskever, and Geoffrey E Hinton. ImageNet classification with deep convolutional neural networks. In *Advances in Neural Information Processing Systems*, pp. 1097–1105, 2012.
- [129] Shouhei Hanaoka, Yoshitaka Masutani, Mitsutaka Nemoto, Yukihiro Nomura, Soichiro Miki, Takeharu Yoshikawa, Naoto Hayashi, and Kuni Ohtomo. A multiple anatomical landmark detection system for body CT images. In *2013 First international symposium on computing and networking*, pp. 308–311. IEEE, 2013.

- [130] Rafael Wiemker, Tobias Klinder, Martin Bergtholdt, Kirsten Meetz, Ingwer C Carlsen, and Thomas Bülow. A radial structure tensor and its use for shape-encoding medical visualization of tubular and nodular structures. *IEEE Transactions on Visualization and Computer Graphics*, Vol. 19, No. 3, pp. 353–366, 2013.
- [131] Jiamin Liu, Jocelyn Zhao, Joanne Hoffman, Jianhua Yao, Weidong Zhang, Evrim B Turkbey, Shijun Wang, Christine Kim, and Ronald M Summers. Mediastinal lymph node detection on thoracic CT scans using spatial prior from multi-atlas label fusion. In *SPIE Medical Imaging*, pp. 90350M–90350M. International Society for Optics and Photonics, 2014.
- [132] Johannes Feulner, S Kevin Zhou, Matthias Hammon, Joachim Hornegger, and Dorin Comaniciu. Lymph node detection and segmentation in chest CT data using discriminative learning and a spatial prior. *Medical Image Analysis*, Vol. 17, No. 2, pp. 254–270, 2013.
- [133] Johannes Feulner, S Kevin Zhou, Alexander Cavallaro, Sascha Seifert, Joachim Hornegger, and Dorin Comaniciu. Fast automatic segmentation of the esophagus from 3D CT data using a probabilistic model. In *International Conference on Medical Image Computing and Computer-Assisted Intervention*, pp. 255–262. Springer, 2009.
- [134] João Otávio Bandeira Diniz, Jonnison Lima Ferreira, Pedro Henrique Bandeira Diniz, Aristófanés Corrêa Silva, and Anselmo Cardoso de Paiva. Esophagus segmentation from planning CT images using an atlas-based deep learning approach. *Computer Methods and Programs in Biomedicine*, Vol. 197, p. 105685, 2020.
- [135] Holger R Roth, Le Lu, Ari Seff, Kevin M Cherry, Joanne Hoffman, Shijun Wang, Jiamin Liu, Evrim Turkbey, and Ronald M Summers. A new 2.5D representa-

- tion for lymph node detection using random sets of deep convolutional neural network observations. In *International Conference on Medical Image Computing and Computer-Assisted Intervention (MICCAI) 2017, LNCS 8673*, pp. 520–527. Springer, 2014.
- [136] Shiying Hu, Eric A Hoffman, and Joseph M Reinhardt. Automatic lung segmentation for accurate quantitation of volumetric X-ray CT images. *IEEE Transactions on Medical Imaging*, Vol. 20, No. 6, pp. 490–498, 2001.
- [137] Mohammadali M Shoja, Paul S Agutter, Marios Loukas, Brion Benninger, Ghaffar Shokouhi, Husain Namdar, Kamyar Ghabili, Majid Khalili, and R Shane Tubbs. Leonardo da Vinci’s studies of the heart. *International journal of cardiology*, Vol. 167, No. 4, pp. 1126–1133, 2013.
- [138] Kapil Sugand, Peter Abrahams, and Ashish Khurana. The anatomy of anatomy: a review for its modernization. *Anatomical sciences education*, Vol. 3, No. 2, pp. 83–93, 2010.
- [139] Charles Leslie, Charles M Leslie, and Allan Young. *Paths to Asian medical knowledge*. No. 32. Univ of California Press, 1992.
- [140] Li Zhang, Eric A Hoffman, and Joseph M Reinhardt. Atlas-driven lung lobe segmentation in volumetric X-ray CT images. *IEEE transactions on medical imaging*, Vol. 25, No. 1, pp. 1–16, 2005.
- [141] Soumik Ukil and Joseph M Reinhardt. Anatomy-guided lung lobe segmentation in X-ray CT images. *IEEE transactions on medical imaging*, Vol. 28, No. 2, pp. 202–214, 2008.
- [142] Tsui-Ying Law and PhengAnn Heng. Automated extraction of bronchus from 3D CT images of lung based on genetic algorithm and 3D region growing. In *Medical*

- Imaging 2000: Image Processing*, Vol. 3979, pp. 906–916. International Society for Optics and Photonics, 2000.
- [143] Kensaku Mori, Jun-ichi Hasegawa, Jun-ichiro Toriwaki, Hirofumi Anno, and Kazuhiro Katada. Recognition of bronchus in three-dimensional X-ray CT images with applications to virtualized bronchoscopy system. In *Proceedings of 13th International Conference on Pattern Recognition*, Vol. 3, pp. 528–532. IEEE, 1996.
- [144] Rômulo Pinho, Sten Luyckx, and Jan Sijbers. Robust region growing based intrathoracic airway tree segmentation. In *Proc. of Second International Workshop on Pulmonary Image Analysis*, pp. 261–271, 2009.
- [145] Jan-Martin Kuhnigk, Horst Hahn, Milo Hindennach, Volker Dicken, Stefan Krass, and Heinz-Otto Peitgen. Lung lobe segmentation by anatomy-guided 3D watershed transform. In *Medical imaging 2003: image processing*, Vol. 5032, pp. 1482–1490. International Society for Optics and Photonics, 2003.
- [146] Ewa Pietka. Lung segmentation in digital radiographs. *Journal of digital imaging*, Vol. 7, No. 2, pp. 79–84, 1994.
- [147] Françoise J Preteux, Philippe Grenier, and Pierre Vanier. Advances in automated lung segmentation in CT studies. In *Medical Imaging 1993: Image Processing*, Vol. 1898, pp. 330–341. International Society for Optics and Photonics, 1993.
- [148] Kensaku Mori, Daisuke Deguchi, Jun Sugiyama, Yasuhito Suenaga, Jun-ichiro Toriwaki, Calvin R Maurer Jr, Hirotsugu Takabatake, and Hiroshi Natori. Tracking of a bronchoscope using epipolar geometry analysis and intensity-based image registration of real and virtual endoscopic images. *Medical Image Analysis*, Vol. 6, No. 3, pp. 321–336, 2002.

- [149] Daisuke Deguchi, Kensaku Mori, Yasuhito Suenaga, Jun-ichi Hasegawa, Jun-ichiro Toriwaki, Hirotsugu Takabatake, and Hiroshi Natori. New image similarity measure for bronchoscope tracking based on image registration. In *International Conference on Medical Image Computing and Computer-Assisted Intervention*, pp. 399–406. Springer, 2003.
- [150] GP Genereux and JL Howie. Normal mediastinal lymph node size and number: CT and anatomic study. *American journal of roentgenology*, Vol. 142, No. 6, pp. 1095–1100, 1984.
- [151] Herman I Libshitz and RJ McKenna Jr. Mediastinal lymph node size in lung cancer. *American journal of roentgenology*, Vol. 143, No. 4, pp. 715–718, 1984.
- [152] JG Murray, M O’Driscoll, and JJ Curtin. Mediastinal lymph node size in an Asian population. *The British journal of radiology*, Vol. 68, No. 808, pp. 348–350, 1995.
- [153] Timothy N Udoji, Gary S Phillips, Eugene A Berkowitz, David Berkowitz, Cicely Ross, and Rabih I Bechara. Mediastinal and hilar lymph node measurements. comparison of multidetector-row computed tomography and endobronchial ultrasound. *Annals of the American Thoracic Society*, Vol. 12, No. 6, pp. 914–920, 2015.
- [154] Alfred Schneider, H Hautmann, Helmut Barfuss, T Pinkau, F Peltz, Hubertus Feussner, and A Wichert. Real-time image tracking of a flexible bronchoscope. In *International Congress Series*, Vol. 1268, pp. 753–757. Elsevier, 2004.
- [155] Kensaku Mori, Daisuke Deguchi, Kazuyoshi Ishitani, Takayuki Kitasaka, Yasuhito Suenaga, Yosihori Hasegawa, Kazuyoshi Imaizumi, and Hirotsugu Takabatake. Bronchoscope tracking without fiducial markers using ultra-tiny electromagnetic tracking system and its evaluation in different environments. In *International*

- Conference on Medical Image Computing and Computer-Assisted Intervention*, pp. 644–651. Springer, 2007.
- [156] Kensaku Mori, Daisuke Deguchi, Kenta Akiyama, Takayuki Kitasaka, Calvin R Maurer, Yasuhito Suenaga, Hirotsugu Takabatake, Masaki Mori, and Hiroshi Natori. Hybrid bronchoscope tracking using a magnetic tracking sensor and image registration. In *International Conference on Medical Image Computing and Computer-Assisted Intervention*, pp. 543–550. Springer, 2005.
- [157] David J Vining, Kun Liu, Robert H Choplin, and Edward F Haponik. Virtual bronchoscopy: relationships of virtual reality endobronchial simulations to actual bronchoscopic findings. *Chest*, Vol. 109, No. 2, pp. 549–553, 1996.
- [158] Chih-Chung Chang and Chih-Jen Lin. LIBSVM: a library for support vector machines. *ACM Transactions on Intelligent Systems and Technology (TIST)*, Vol. 2, No. 3, p. 27, 2011.
- [159] Corinna Cortes and Vladimir Vapnik. Support-vector networks. *Machine Learning*, Vol. 20, No. 3, pp. 273–297, 1995.
- [160] Ivana Isgum, Bram van Ginneken, and Marco Olree. Automatic detection of calcifications in the aorta from CT scans of the abdomen. *Academic Radiology*, Vol. 11, No. 3, pp. 247–257, 2004.
- [161] Yoshitaka Masutani, Heber MacMahon, and Kunio Doi. Computerized detection of pulmonary embolism in spiral CT angiography based on volumetric image analysis. *IEEE Transactions on Medical Imaging*, Vol. 21, No. 12, pp. 1517–1523, 2002.
- [162] Se Hyung Kim, Jeong Min Lee, Joon-Goo Lee, Jong Hyo Kim, Philippe A Lefere, Joon Koo Han, and Byung Ihn Choi. Computer-aided detection of colonic polyps

- at CT colonography using a hessian matrix-based algorithm: preliminary study. *American Journal of Roentgenology*, Vol. 189, No. 1, pp. 41–51, 2007.
- [163] Amir H Foruzan, Reza A Zoroofi, Yoshinobu Sato, and Masatoshi Hori. A Hessian-based filter for vascular segmentation of noisy hepatic CT scans. *International Journal of Computer Assisted Radiology and Surgery*, Vol. 7, No. 2, pp. 199–205, 2012.
- [164] Suguru Kawajiri, Xiangrong Zhou, Xuejun Zhang, Takeshi Hara, Hiroshi Fujita, Ryujiro Yokoyama, Hiroshi Kondo, Masayuki Kanematsu, and Hiroaki Hoshi. Automated segmentation of hepatic vessels in non-contrast X-ray CT images. *Radiological Physics and Technology*, Vol. 1, No. 2, pp. 214–222, 2008.
- [165] Zhenghao Shi, Minghua Zhao, Lifeng He, Yinghui Wang, Ming Zhang, and Kenji Suzuki. A computer aided pulmonary nodule detection system using multiple massive training svms. *Applied Mathematics*, Vol. 7, No. 3, pp. 1165–1172, 2013.
- [166] Hidenori Shikata, Eric A Hoffman, and Milan Sonka. Automated segmentation of pulmonary vascular tree from 3D CT images. In *Medical Imaging 2004*, pp. 107–116. International Society for Optics and Photonics, 2004.
- [167] Compound microscope — fun science. <https://funscience.in/compound-microscope/>.
- [168] Anatomy and physiology ii: The lungs. <https://courses.lumenlearning.com/suny-ap2/chapter/the-lungs/>.
- [169] 生物・病原菌などの解析事例 | 花市電子顕微鏡技術研究所. <https://www.kenbikyo.com/creature/>.
- [170] <https://www.kek.jp/en/Facility/IMSS/PF/PFRing/Imaging/>.

- [171] [http://www.mext.go.jp/b\\_menu/shingi/chousa/shinkou/010/houkoku/05081201/s001.htm](http://www.mext.go.jp/b_menu/shingi/chousa/shinkou/010/houkoku/05081201/s001.htm).
- [172] OER Services. Anatomy and physiology ii: The lungs. <https://courses.lumenlearning.com/suny-ap2/chapter/the-lungs/>.
- [173] RA Greenbaum, S Yen Ho, DG Gibson, AE Becker, and RH Anderson. Left ventricular fibre architecture in man. *Heart*, Vol. 45, No. 3, pp. 248–263, 1981.
- [174] Theo Arts, Robert S Reneman, and Peter C Veenstra. A model of the mechanics of the left ventricle. *Annals of biomedical engineering*, Vol. 7, No. 3-4, pp. 299–318, 1979.
- [175] Ramón Casero, Urszula Siedlecka, Elizabeth S Jones, Lena Gruscheski, Matthew Gibb, Jürgen E Schneider, Peter Kohl, and Vicente Grau. Transformation diffusion reconstruction of three-dimensional histology volumes from two-dimensional image stacks. *Medical Image Analysis*, Vol. 38, pp. 184–204, 2017.
- [176] Marco Nolden, Sascha Zelzer, Alexander Seitel, Diana Wald, Michael Müller, Alfred M Franz, Daniel Maleike, Markus Fangerau, Matthias Baumhauer, Lena Maier-Hein, et al. The Medical Imaging Interaction Toolkit: challenges and advances. *International Journal of Computer Assisted Radiology and Surgery*, Vol. 8, No. 4, pp. 607–620, 2013.
- [177] Doga Gürsoy, Francesco De Carlo, Xianghui Xiao, and Chris Jacobsen. TomoPy: a framework for the analysis of synchrotron tomographic data. *Journal of synchrotron radiation*, Vol. 21, No. 5, pp. 1188–1193, 2014.
- [178] Utkarsh Ayachit. *The ParaView Guide: A Parallel Visualization Application*. Kitware, Inc., 2015.

- [179] Patrick Helm, Mirza Faisal Beg, Michael I Miller, and Raimond L Winslow. Measuring and mapping cardiac fiber and laminar architecture using diffusion tensor MR imaging. *Annals of the New York Academy of Sciences*, Vol. 1047, No. 1, pp. 296–307, 2005.
- [180] Peter J Basser, Sinisa Pajevic, Carlo Pierpaoli, Jeffrey Duda, and Akram Aldroubi. In vivo fiber tractography using DT-MRI data. *Magnetic resonance in medicine*, Vol. 44, No. 4, pp. 625–632, 2000.
- [181] Vincent Chan and Anahi Perlas. Basics of ultrasound imaging. In *Atlas of ultrasound-guided procedures in interventional pain management*, pp. 13–19. Springer, 2011.
- [182] Susan A Elmore. Histopathology of the lymph nodes. *Toxicologic pathology*, Vol. 34, No. 5, pp. 425–454, 2006.
- [183] Hiroshi Kura, Norihiro Sato, Akihiko Uchiyama, Yuji Nakafusa, Ryuichi Mibu, Kouichirou Yoshida, Kentaro Kuroiwa, and Masao Tanaka. Mediastinal lymph node metastasis of colon cancer: report of a case. *Surgery today*, Vol. 29, No. 4, pp. 375–377, 1999.
- [184] Hiroaki Nomori, Shizuka Kaseda, Kouichi Kobayashi, Tsuneo Ishihara, Noboru Yanai, and Chikao Torikata. Adenoid cystic carcinoma of the trachea and mainstem bronchus: a clinical, histopathologic, and immunohistochemical study. *The Journal of Thoracic and Cardiovascular Surgery*, Vol. 96, No. 2, pp. 271–277, 1988.
- [185] 小川邦康. イメージング mri (磁気共鳴画像法). *ぶんせき*, Vol. 2019, No. 1, pp. 2–10, 2019.

- [186] Koji Hashimoto, Shoji Kawashima, Masao Araki, Kazuo Iwai, Kunihiro Sawada, and Yutaka Akiyama. Comparison of image performance between cone-beam computed tomography for dental use and four-row multidetector helical CT. *Journal of oral science*, Vol. 48, No. 1, pp. 27–34, 2006.
- [187] AK Suomalainen, A Salo, Soraya Robinson, and JS Peltola. The 3DX multi image micro-CT device in clinical dental practice. *Dentomaxillofacial Radiology*, Vol. 36, No. 2, pp. 80–85, 2007.
- [188] Michael J Paulus, Shaun S Gleason, Stephen J Kennel, Patricia R Hunsicker, and Dabney K Johnson. High resolution X-ray computed tomography: an emerging tool for small animal cancer research. *Neoplasia*, Vol. 2, No. 1-2, pp. 62–70, 2000.
- [189] RI Radu, Adriana Bold, OT Pop, D Gh Mălăescu, IRINA Gheorghisor, and L Mogoantă. Histological and immunohistochemical changes of the myocardium in dilated cardiomyopathy. *Rom. J. Morphol. Embryol*, Vol. 53, No. 2, pp. 269–275, 2012.
- [190] 山口功, 市川勝弘, 辻岡勝美, 宮下宗治. 放射線技術学シリーズ CT 撮影技術学 (改訂 2 版). 日本放射線技術学会, 2011.
- [191] Firdaus Janoos, Kishore Mosaliganti, Xiaoyin Xu, Raghu Machiraju, Kun Huang, and Stephen TC Wong. Robust 3D reconstruction and identification of dendritic spines from optical microscopy imaging. *Medical image analysis*, Vol. 13, No. 1, pp. 167–179, 2009.
- [192] Ignacio Arganda-Carreras, Rodrigo Fernández-González, Arrate Muñoz-Barrutia, and Carlos Ortiz-De-Solorzano. 3D reconstruction of histological sections: Ap-

- plication to mammary gland tissue. *Microscopy research and technique*, Vol. 73, No. 11, pp. 1019–1029, 2010.
- [193] Fei Guo and Wen Jiang. Single particle cryo-electron microscopy and 3-D reconstruction of viruses. In *Electron Microscopy*, pp. 401–443. Springer, 2014.
- [194] Anne Sakdinawat and David Attwood. Nanoscale X-ray imaging. *Nature photonics*, Vol. 4, No. 12, p. 840, 2010.
- [195] Donald H Bilderback, Stephen A Hoffman, and Daniel J Thiel. Nanometer spatial resolution achieved in hard X-ray imaging and Laue diffraction experiments. *Science*, Vol. 263, No. 5144, pp. 201–203, 1994.
- [196] Maoyu Wang, LÍney Árnadóttir, Zhichuan J Xu, and Zhenxing Feng. In situ X-ray absorption spectroscopy studies of nanoscale electrocatalysts. *Nano-Micro Letters*, Vol. 11, No. 1, p. 47, 2019.
- [197] Martin Dierolf, Andreas Menzel, Pierre Thibault, Philipp Schneider, Cameron M Kewish, Roger Wepf, Oliver Bunk, and Franz Pfeiffer. Ptychographic X-ray computed tomography at the nanoscale. *Nature*, Vol. 467, No. 7314, pp. 436–439, 2010.
- [198] Joy C Andrews, Eduardo Almeida, Marjolein CH van der Meulen, Joshua S Alwood, Chialing Lee, Yijin Liu, Jie Chen, Florian Meirer, Michael Feser, Jeff Gelb, et al. Nanoscale X-ray microscopic imaging of mammalian mineralized tissue. *Microscopy and Microanalysis: The Official Journal of Microscopy Society of America, Microbeam Analysis Society, Microscopical Society of Canada*, Vol. 16, No. 3, p. 327, 2010.
- [199] Max Langer, Alexandra Pacureanu, Heikki Suhonen, Quentin Grimal, Peter

- Cloetens, and Françoise Peyrin. X-ray phase nanotomography resolves the 3D human bone ultrastructure. *PloS one*, Vol. 7, No. 8, p. e35691, 2012.
- [200] Xiaojin Jerry Zhu. Semi-supervised learning literature survey. Technical report, University of Wisconsin-Madison Department of Computer Sciences, 2005.
- [201] Longlong Jing and Yingli Tian. Self-supervised visual feature learning with deep neural networks: A survey. *IEEE Transactions on Pattern Analysis and Machine Intelligence*, 2020.
- [202] Christopher L Vaughan. *Imagining the elephant: A biography of Allan MacLeod Cormack*. Juta and Company Ltd, 2008.
- [203] Elizabeth C Beckmann. Ct scanning the early days. *The British journal of radiology*, Vol. 79, No. 937, pp. 5–8, 2006.
- [204] Romy J Brinkman and J Joris Hage. Andreas Vesalius ’ 500th anniversary: First description of the mammary suspensory ligaments. *World journal of surgery*, Vol. 40, No. 9, pp. 2144–2148, 2016.
- [205] John F Dobson. Herophilus of Alexandria. *Proceedings of the Royal Society of Medicine*, Vol. 18, No. Sect\_Hist\_Med, pp. 19–32, 1925.
- [206] Mauricio Kugler, Yushi Goto, Yuki Tamura, Naoki Kawamura, Hirokazu Kobayashi, Tatsuya Yokota, Chika Iwamoto, Kenoki Ohuchida, Makoto Hashizume, Akinobu Shimizu, et al. Robust 3D image reconstruction of pancreatic cancer tumors from histopathological images with different stains and its quantitative performance evaluation. *International journal of computer assisted radiology and surgery*, Vol. 14, No. 12, pp. 2047–2055, 2019.
- [207] Berardo Di Matteo, Vittorio Tarabella, Giuseppe Filardo, Massimiliano Mosca, Mirco Lo Presti, Anna Viganò, Patrizia Tomba, and Maurilio Marcacci. Art in

- science: Mondino de ' Liuzzi: the restorer of anatomy. *Clinical Orthopaedics and Related Research*, Vol. 475, No. 7, pp. 1791–1795, 2017.
- [208] D Todman. Galen (129-199). *Journal of neurology*, Vol. 254, No. 7, p. 975, 2007.
- [209] James W Fletcher, Benjamin Djulbegovic, Heloisa P Soares, Barry A Siegel, Val J Lowe, Gary H Lyman, R Edward Coleman, Richard Wahl, John Christopher Paschold, Norbert Avril, et al. Recommendations on the use of 18F-FDG PET in oncology. *Journal of Nuclear Medicine*, Vol. 49, No. 3, pp. 480–508, 2008.
- [210] Yoshio Machida and Kazuo Mori. Basic principle of MR imaging. *Medical imaging technology*, Vol. 28, No. 1, pp. 63–67, jan 2010.
- [211] Willi A Kalender. X-ray computed tomography. *Physics in Medicine & Biology*, Vol. 51, No. 13, p. R29, 2006.
- [212] Kalyan B Bhattacharyya. Godfrey Newbold Hounsfield (1919–2004): The man who revolutionized neuroimaging. *Annals of Indian Academy of Neurology*, Vol. 19, No. 4, p. 448, 2016.
- [213] Veronika Cheplygina, Marleen de Bruijne, and Josien PW Pluim. Not-so-supervised: a survey of semi-supervised, multi-instance, and transfer learning in medical image analysis. *Medical image analysis*, Vol. 54, pp. 280–296, 2019.
- [214] Kenji Yoshida. Principle of ultrasonic diagnostic imaging. *Journal of the Society of Instrument and Control Engineers*, Vol. 58, No. 7, pp. 489–493, jul 2019.
- [215] Asako Kanezaki. Unsupervised image segmentation by backpropagation. In *2018 IEEE international conference on acoustics, speech and signal processing (ICASSP)*, pp. 1543–1547. IEEE, 2018.

- [216] Michael Lynch, Ovidiu Ghita, and Paul F Whelan. Automatic segmentation of the left ventricle cavity and myocardium in MRI data. *Computers in biology and medicine*, Vol. 36, No. 4, pp. 389–407, 2006.
- [217] David Attwood. Nanotomography comes of age. *Nature*, Vol. 442, No. 7103, pp. 642–643, 2006.
- [218] Yi Song, Darren Treanor, Andrew J Bulpitt, and Derek R Magee. 3D reconstruction of multiple stained histology images. *Journal of pathology informatics*, Vol. 4, No. Suppl, 2013.
- [219] Jonas Pichat, Juan Eugenio Iglesias, Tarek Yousry, Sébastien Ourselin, and Marc Modat. A survey of methods for 3D histology reconstruction. *Medical image analysis*, Vol. 46, pp. 73–105, 2018.
- [220] Roberto Marabini, Gabor T Herman, and José M Carazo. 3D reconstruction in electron microscopy using art with smooth spherically symmetric volume elements (blobs). *Ultramicroscopy*, Vol. 72, No. 1-2, pp. 53–65, 1998.
- [221] Atsushi Sanbe, Jason G Fewell, James Gulick, Hanna Osinska, John Lorenz, D Greg Hall, Lisa A Murray, Thomas R Kimball, Sandra A Witt, and Jeffrey Robbins. Abnormal cardiac structure and function in mice expressing nonphosphorylatable cardiac regulatory myosin light chain 2. *Journal of Biological Chemistry*, Vol. 274, No. 30, pp. 21085–21094, 1999.
- [222] Joachim R Sommer and Edward A Johnson. Cardiac muscle: a comparative study of purkinje fibers and ventricular fibers. *The Journal of Cell Biology*, Vol. 36, No. 3, pp. 497–526, 1968.
- [223] T Ohtani, K Oho, R Amemiya, O Taira, K Hayakawa, I Ogawa, and Y Hayata. Experiments on tumor resection by laser surgery via the fiberoptic broncho-

- scope. In *Bronchology: Research, Diagnostic, and Therapeutic Aspects*, pp. 537–539. Springer, 1981.
- [224] DM Mitchell, DN Mitchell, JV Collins, and CJ Emerson. Transbronchial lung biopsy through fiberoptic bronchoscope in diagnosis of sarcoidosis. *Br Med J*, Vol. 280, No. 6215, pp. 679–681, 1980.
- [225] Atsushi Teramoto and Hiroshi Fujita. Fast lung nodule detection in chest CT images using cylindrical nodule-enhancement filter. *International journal of computer assisted radiology and surgery*, Vol. 8, No. 2, pp. 193–205, 2013.
- [226] Jochen Peters, Olivier Ecabert, Carsten Meyer, Hauke Schramm, Reinhard Kneser, Alexandra Groth, and Jürgen Weese. Automatic whole heart segmentation in static magnetic resonance image volumes. In *International Conference on Medical Image Computing and Computer-Assisted Intervention*, pp. 402–410. Springer, 2007.
- [227] Maria Lorenzo-Valdés, Gerardo I Sanchez-Ortiz, Andrew G Elkington, Raad H Mohiaddin, and Daniel Rueckert. Segmentation of 4D cardiac MR images using a probabilistic atlas and the EM algorithm. *Medical Image Analysis*, Vol. 8, No. 3, pp. 255–265, 2004.
- [228] MR Avendi, Arash Kheradvar, and Hamid Jafarkhani. A combined deep-learning and deformable-model approach to fully automatic segmentation of the left ventricle in cardiac mri. *Medical image analysis*, Vol. 30, pp. 108–119, 2016.
- [229] Mariana Bustamante, Vikas Gupta, Daniel Forsberg, Carl-Johan Carlhäll, Jan Engvall, and Tino Ebbers. Automated multi-atlas segmentation of cardiac 4D flow MRI. *Medical image analysis*, Vol. 49, pp. 128–140, 2018.

- [230] Jason L Causey, Junyu Zhang, Shiqian Ma, Bo Jiang, Jake A Qualls, David G Politte, Fred Prior, Shuzhong Zhang, and Xiuzhen Huang. Highly accurate model for prediction of lung nodule malignancy with ct scans. *Scientific reports*, Vol. 8, No. 1, pp. 1–12, 2018.
- [231] Maxine Tan, Rudi Deklerck, Bart Jansen, Michel Bister, and Jan Cornelis. A novel computer-aided lung nodule detection system for CT images. *Medical physics*, Vol. 38, No. 10, pp. 5630–5645, 2011.
- [232] Oleg V Aslanidi, Theodora Nikolaidou, Jichao Zhao, Bruce H Smaill, Stephen H Gilbert, Arun V Holden, Tristan Lowe, Philip J Withers, Robert S Stephenson, Jonathan C Jarvis, et al. Application of micro-computed tomography with iodine staining to cardiac imaging, segmentation, and computational model development. *IEEE transactions on medical imaging*, Vol. 32, No. 1, pp. 8–17, 2012.
- [233] David F Scollan, Alex Holmes, Raimond Winslow, and John Forder. Histological validation of myocardial microstructure obtained from diffusion tensor magnetic resonance imaging. *American Journal of Physiology-Heart and Circulatory Physiology*, Vol. 275, No. 6, pp. H2308–H2318, 1998.
- [234] Herve Lombaert, Jean-Marc Peyrat, Pierre Croisille, Stanislas Rapacchi, Laurent Fanton, Patrick Clarysse, Herve Delingette, and Nicholas Ayache. Statistical analysis of the human cardiac fiber architecture from DT-MRI. In *International Conference on Functional Imaging and Modeling of the Heart*, pp. 171–179. Springer, 2011.
- [235] Damien Rohmer, Arkadiusz Sitek, and Grant T Gullberg. Reconstruction and visualization of fiber and laminar structure in the normal human heart from ex vivo diffusion tensor magnetic resonance imaging (DTMRI) data. *Investigative radiology*, Vol. 42, No. 11, pp. 777–789, 2007.

- [236] Emelia J. Benjamin, Salim S. Virani, Clifton W. Callaway, et al. Heart disease and stroke statistics-2018 update: a report from the American Heart Association. *Circulation*, Vol. 137, p. e67e492, 2018.
- [237] Daniel D Streeter Jr, Henry M Spotnitz, Dali P Patel, Edmund H Sonnenblick, et al. Fiber orientation in the canine left ventricle during diastole and systole. *Circulation Research*, Vol. 24, No. 3, pp. 339–347, 1969.
- [238] Takuya Kunii, Ryota Shirai, Akio Yoneyama, Hiroko Maruyama, Thet Thet Lwin, and Tohoru Takeda. Visualization of rat myocardial layers in phase-contrast X-ray imaging with ethanol fixation. *Medical Imaging Technology*, Vol. 31, No. 2, pp. 132–135, 2013.
- [239] Robert S Stephenson, Mark R Boyett, George Hart, Theodora Nikolaidou, Xue Cai, Antonio F Corno, Nelson Alphonso, Nathan Jeffery, and Jonathan C Jarvis. Contrast enhanced micro-computed tomography resolves the 3-dimensional morphology of the cardiac conduction system in mammalian hearts. *PloS one*, Vol. 7, No. 4, p. e35299, 2012.
- [240] Mattias P Heinrich, Mark Jenkinson, Michael Brady, and Julia A Schnabel. MRF-based deformable registration and ventilation estimation of lung CT. *IEEE Transactions on Medical Imaging*, Vol. 32, No. 7, pp. 1239–1248, 2013.
- [241] Yasushi Hirano, Rui Xu, Rie Tachibana, and Shoji Kido. A method for extracting airway tree by using a cavity enhancement filter. In *Fourth International Workshop on Pulmonary Image Analysis*, pp. 91–99, 2011.
- [242] Arumugham Sukanya, Rajendran Rajeswari, and Kamatchigounder Subramaniam Murugan. Region based coronary artery segmentation using modified

- Frangi's vesselness measure. *International Journal of Imaging Systems and Technology*, Vol. 30, No. 3, pp. 716–730, 2020.
- [243] Jurgen AW Heymann, Mike Hayles, Ingo Gestmann, Lucille A Giannuzzi, Ben Lich, and Sriram Subramaniam. Site-specific 3D imaging of cells and tissues with a dual beam microscope. *Journal of structural biology*, Vol. 155, No. 1, pp. 63–73, 2006.
- [244] Seunghwan Yoo, Pablo Ruiz, Xiang Huang, Kuan He, Nicola J Ferrier, Mark Hereld, Alan Selewa, Matthew Daddysman, Norbert Scherer, Oliver Cossairt, et al. 3D image reconstruction from multi-focus microscope: axial super-resolution and multiple-frame processing. In *2018 IEEE International Conference on Acoustics, Speech and Signal Processing (ICASSP)*, pp. 1453–1457. IEEE, 2018.
- [245] Oleg V Aslanidi, Theodora Nikolaidou, Jichao Zhao, Bruce H Smaill, Stephen H Gilbert, Arun V Holden, Tristan Lowe, Philip J Withers, Robert S Stephenson, Jonathan C Jarvis, et al. Application of micro-computed tomography with iodine staining to cardiac imaging, segmentation, and computational model development. *IEEE Transactions on Medical Imaging*, Vol. 32, No. 1, pp. 8–17, 2013.
- [246] Marta Varela, Jichao Zhao, and Oleg V Aslanidi. Determination of atrial myofibre orientation using structure tensor analysis for biophysical modelling. In *International Conference on Functional Imaging and Modeling of the Heart*, pp. 425–432. Springer, 2013.
- [247] Naoki Sunaguchi, Tetsuya Yuasa, Qingkai Huo, Shu Ichihara, and Masami Ando. refraction-contrast computed tomography images using dark-field imaging optics. *Applied Physics Letters*, Vol. 97, No. 15, p. 153701, 2010.
- [248] Naoki Sunaguchi, Tetsuya Yuasa, Shin-ichi Hirano, Rajiv Gupta, and Masami

Ando. In vitro validation of an artefact suppression algorithm in X-ray phase-contrast computed tomography. *PloS one*, Vol. 10, No. 8, p. e0135654, 2015.

- [249] Olaf Ronneberger, Philipp Fischer, and Thomas Brox. U-net: Convolutional networks for biomedical image segmentation. In *International Conference on Medical image computing and computer-assisted intervention*, pp. 234–241. Springer, 2015.

# Publications

- Hirohisa Oda, Kohei Nishio, Takayuki Kitasaka, Hizuru Amano, Aitaro Takimoto, Hiroo Uchida, Kojiro Suzuki, Hayato Itoh, Masahiro Oda, and Kensaku Mori. Intestinal region reconstruction of ileus cases from 3D CT images based on graphical representation and its visualization. In *Medical Imaging 2021: Computer-Aided Diagnosis*. International Society for Optics and Photonics, 2021 (Accepted).
- Hirohisa Oda, Holger R Roth, Takaaki Sugino, Naoki Sunaguchi, Noriko Usami, Masahiro Oda, Daisuke Shima, Shu Ichihara, Tetsuya Yuasa, Masami Ando, Toshiaki Akita, Yuji Narita, and Kensaku Mori. Cardiac fiber tracking on super high-resolution CT images: a comparative study. *Journal of Medical Imaging*, Vol. 7, No. 2, p. 026001, 2020.
- Hirohisa Oda, Tamada Yudai, Kohei Nishio, Takayuki Kitasaka, Hizuru Amano, Kosuke Chiba, Akinari Hinoki, Hiroo Uchida, Masahiro Oda, and Kensaku Mori. Detecting ganglion cells on virtual slide images: Macroscopic masking by superpixel. *International Journal of Computer Assisted Radiology and Surgery*, Vol. 15, Sup. 1, pp. S169–S170, 2020.
- Hirohisa Oda, Kohei Nishio, Takayuki Kitasaka, Hizuru Amano, Aitaro Takimoto, Hiroo Uchida, Kojiro Suzuki, Hayato Itoh, Masahiro Oda, and Kensaku Mori. Visualizing intestines for diagnostic assistance of ileus based on intestinal region segmentation

- from 3D CT images. In *Medical Imaging 2020: Computer-Aided Diagnosis*, Vol. 11314, p. 1131434. International Society for Optics and Photonics, 2020.
- Hirohisa Oda, Holger R Roth, Naoki Sunaguchi, Masahiro Oda, Daisuke Shima, Shu Ichihara, Tetsuya Yuasa, and Masami Ando. Scanning, registration, and fiber estimation of rabbit hearts using micro-focus and refraction-contrast X-ray CT. In *Medical Imaging 2019: Biomedical Applications in Molecular, Structural, and Functional Imaging*, Vol. 10953, p. 109531I. International Society for Optics and Photonics, 2019.
  - Hirohisa Oda, Kohei Nishio, Takayuki Kitasaka, Benjamin Villard, Hizuru Amano, Kosuke Chiba, Akinari Hinoki, Hiroo Uchida, Kojiro Suzuki, Hayato Itoh, Oda Masahiro, and Kensaku Mori. Spaciousness filters for non-contrast CT volume segmentation of the intestine region for emergency ileus diagnosis. In *Uncertainty for Safe Utilization of Machine Learning in Medical Imaging and Clinical Image-Based Procedures*, pp. 104–114. Springer, 2019.
  - 小田紘久, 西尾光平, 北坂孝幸, 天野日出, 千馬耕亮, 内田広夫, 鈴木耕次, 伊東隼人, 小田昌宏, 森健策. 少量のラベルデータを用いた学習によるイレウス症例 CT 像における拡張腸管の自動抽出. 第 38 回日本医用画像工学会大会予稿集 (JAMIT2019), pp. OP1–15, 2019.
  - 小田紘久, 西尾光平, 北坂孝幸, 玉田雄大, 天野日出, 千馬耕亮, 檜頭成, 内田広夫, 小田昌宏, 森健策. 神経節細胞検出のための腸管組織のバーチャルスライド画像における筋層抽出. 日本コンピュータ外科学会誌 第 28 回日本コンピュータ外科学会大会特集号, Vol. 21, No. 4, 19(VII)4, pp. 276–277, 2019.
  - Hirohisa Oda, Holger R Roth, Kosuke Chiba, Jure Sokolić, Takayuki Kitasaka, Masahiro Oda, Akinari Hinoki, Hiroo Uchida, Julia A Schnabel, and Kensaku Mori. BESNet: boundary-enhanced segmentation of cells in histopathological images. In

*International Conference on Medical Image Computing and Computer-Assisted Intervention, Lecture Notes in Computer Science 11071*, pp. 228–236. Springer, 2018.

- Hirohisa Oda, Holger R Roth, Kanwal K Bhatia, Masahiro Oda, Takayuki Kitasaka, Shingo Iwano, Hirotoishi Homma, Hirotsugu Takabatake, Masaki Mori, Hiroshi Natori, Julia A Schnabel, and Kensaku Mori. Dense volumetric detection and segmentation of mediastinal lymph nodes in chest CT images. In *Medical Imaging 2018: Computer-Aided Diagnosis*, Vol. 10575, p. 1057502. International Society for Optics and Photonics, 2018.
- Hirohisa Oda, Holger R Roth, Naoki Sunaguchi, Tetsuya Yuasa, Toshiaki Akita, Kensaku Mori, Daisuke Shima, Shu Ichihara, Masami Ando, Noriko Usami, Masahiro Oda, and Yuji Narita. Micro-focus X-ray CT of the heart: A comparison with X-ray refraction-contrast CT. *International Journal of Computer Assisted Radiology and Surgery*, Vol. 13, Sup. 1, pp. S140–S142, 2018.
- 小田紘久, Holger R. Roth, 砂口尚輝, 宇佐美紀子, 小田昌宏, 島雄大介, 市原周, 湯浅哲也, 安藤正海, 秋田利明, 成田裕司, 森健策. ウサギ心臓の屈折 CT 像における線維配向の可視化ならびに評価. 第 37 回日本医用画像工学会大会予稿集 (JAMIT2018), pp. OP1–8, 2018.
- 小田紘久, 砂口尚輝, 中村彰太, 秋田利明, 森健策. マイクロ CT 画像を用いた胸部微細解剖構造解析. *Medical Imaging Technology*, Vol. 36, No. 4, pp. 174–180, 2018.
- 小田紘久, Kanwal K. Bhatia, Holger R. Roth, 小田昌宏, 北坂孝幸, 岩野信吾, 本間裕敏, 高島博嗣, 森雅樹, 名取博, Julia A. Schnabel, 森健策. 3D U-Net による 3 次元胸部 CT 像からのリンパ節検出. 第 36 回日本医用画像工学会大会 (JAMIT2017), pp. OP1–6, 2017.

- Hirohisa Oda, Kanwal K Bhatia, Masahiro Oda, Takayuki Kitasaka, Shingo Iwano, Hirotooshi Homma, Hirotsugu Takabatake, Masaki Mori, Hiroshi Natori, Julia A Schnabel, and Kensaku Mori. Automated mediastinal lymph node detection from CT volumes based on intensity targeted radial structure tensor analysis. *Journal of Medical Imaging*, Vol. 4, No. 4, p. 044502, 2017.
- Hirohisa Oda, Masahiro Oda, Takayuki Kitasaka, Toshiaki Akita, and Kensaku Mori. Extracellular matrix directions estimation of the heart on micro-focus X-ray CT volumes. In *Medical Imaging 2017: Biomedical Applications in Molecular, Structural, and Functional Imaging*, Vol. 10137, p. 101370M. International Society for Optics and Photonics, 2017.
- Hirohisa Oda, Kanwal K Bhatia, Masahiro Oda, Takayuki Kitasaka, Shingo Iwano, Julia A Schnabel, and Kensaku Mori. GPU implementation of SLIC supervoxel oversegmentation. In *Medical Imaging 2017: Biomedical Applications in Molecular, Structural, and Functional Imaging*, Vol. 10137, p. 101370M. International Society for Optics and Photonics, 2017.
- Hirohisa Oda, Kanwal K Bhatia, Masahiro Oda, Takayuki Kitasaka, Shingo Iwano, Hirotooshi Homma, Hirotsugu Takabatake, Masaki Mori, Hiroshi Natori, Julia A Schnabel, and Kensaku Mori. Hessian-assisted supervoxel: structure-oriented voxel clustering and application to mediastinal lymph node detection from CT volumes. In *Medical Imaging 2017: Computer-Aided Diagnosis*, Vol. 10134, p. 101341D. International Society for Optics and Photonics, 2017.
- 小田紘久, 小田昌宏, 北坂孝幸, 森健策. MIST ライブラリのための GPU プログラミング. 電子情報通信学会技術研究報告 (医用画像 MI), Vol. 116, No. 393, pp. 133–136, 2017.
- Hirohisa Oda, Holger R Roth, Kanwal K Bhatia, Masahiro Oda, Takayuki Kitasaka, Toshiaki Akita, Julia A Schnabel, and Kensaku Mori. TBS: Tensor-based supervoxels

- for unfolding the heart. In *International Conference on Medical Image Computing and Computer-Assisted Intervention, Lecture Notes in Computer Science 10433*, pp. 681–689. Springer, 2017.
- Hirohisa Oda, Masahiro Oda, Takayuki Kitasaka, Toshiaki Akita, and Kensaku Mori. Comparison of Hessian-matrix- and structure-tensor-based methods for myofiber structure extraction from micro-CT volumes. *International Journal of Computer Assisted Radiology and Surgery*, Vol. 11, Sup. 11, pp. S38–S39, 2016.
  - Hirohisa Oda, Masahiro Oda, Takayuki Kitasaka, Shingo Iwano, Hirotochi Homma, Hirotsugu Takabatake, Masaki Mori, Hiroshi Natori, and Kensaku Mori. Evaluation of efficiency of feature values for false positive reduction of automated mediastinal lymph node detection. *International Journal of Computer Assisted Radiology and Surgery*, Vol. 11, Sup. 1, pp. S130–S131, 2016.
  - 小田紘久, 二村幸孝, 小田昌宏, 北坂孝幸, 岩野信吾, 本間裕敏, 高島博嗣, 森雅樹, 名取博, 森健策. Radial Structure Tensor に基づく塊状構造強調フィルタの縦隔リンパ節検出への利用に関する検討. 第18回画像の認識・理解シンポジウム (MIRU2015), pp. SS4–10, 2015.
  - 小田紘久, 小田昌宏, 北坂孝幸, 秋田利明, 森健策. マイクロ CT 画像からの線維方向追跡に関する検討. 電子情報通信学会技術研究報告 (医用画像 MI), Vol. 115, No. 301, pp. 9–14, 2015.
  - 小田紘久, 二村幸孝, 小田昌宏, 北坂孝幸, 岩野信吾, 本間裕敏, 高島博嗣, 森雅樹, 名取博, 森健策. 縦隔リンパ節検出のための Radial Structure Tensor 解析の改良に関する基礎的検討. 日本コンピュータ外科学会誌 第24回日本コンピュータ外科学会大会特集号, Vol. 17, No. 3, pp. 256–257, 2015.